Nanoscale Horizons

ROYAL SOCIETY OF CHEMISTRY

REVIEW

View Article Online
View Journal | View Issue

Cite this: *Nanoscale Horiz.*, 2022, 7, 1299

Self-assembly, alignment, and patterning of metal nanowires

Ying Chen,†[a] Tianwei Liang,†[a] Lei Chen,[abc] Yaofei Chen,[abc] Bo-Ru Yang,[d] Yunhan Luo*[abc] and Gui-Shi Liu*[abc]

Received 2nd July 2022,
Accepted 29th August 2022

DOI: 10.1039/d2nh00313a

rsc.li/nanoscale-horizons

Armed with the merits of one-dimensional nanostructures (flexibility, high aspect ratio, and anisotropy) and metals (high conductivity, plasmonic properties, and catalytic activity), metal nanowires (MNWs) have stood out as a new class of nanomaterials in the last two decades. They are envisaged to expedite significantly and even revolutionize a broad spectrum of applications related to display, sensing, energy, plasmonics, photonics, and catalysis. Compared with disordered MNWs, well-organized MNWs would not only enhance the intrinsic physical and chemical properties, but also create new functions and sophisticated architectures of optoelectronic devices. This paper presents a comprehensive review of assembly strategies of MNWs, including self-assembly for specific structures, alignment for anisotropic constructions, and patterning for precise configurations. The technical processes, underlying mechanisms, performance indicators, and representative applications of these strategies are described and discussed to inspire further innovation in assembly techniques and guide the fabrication of optoelectrical devices. Finally, a perspective on the critical challenges and future opportunities of MNW assembly is provided.

1. Introduction

One-dimensional (1D) nanomaterials with unique physical and chemical properties have received great attention from the industrial and academic communities.[1,2] In particular, metal nanowires (MNWs) are regarded as promising alternatives to rigid, bulk materials (such as indium tin oxide (ITO)) due to their merits of high electrical conductivity, distinct optical capabilities, large aspect ratio, solution-processible fabrication, *etc.*[3] With these merits, assembled MNWs can circumvent the issues of fragility, low flexibility, and high cost while maintaining or surpassing the electronic, optical,

[a] *Guangdong Provincial Key Laboratory of Optical Fiber Sensing and Communications, Department of Optoelectronic Engineering, Jinan University, Guangzhou 510632, China. E-mail: yunhanluo@163.com, guishiliu@163.com*
[b] *Key Laboratory of Visible Light Communications of Guangzhou, Jinan University, Guangzhou 510632, China*
[c] *Key Laboratory of Optoelectronic Information and Sensing Technologies of Guangdong Higher Education Institutes, Guangzhou 510632, China*
[d] *State Key Laboratory of Optoelectronic Materials and Technologies, School of Electronics and Information Technology, Sun Yat-Sen University, Guangzhou 510006, China*
† These authors contributed equally.

Ying Chen

Ying Chen received her bachelor's degree from the Department of Optoelectronic Engineering, Jinan University, Guangzhou, China, in 2022. She is currently pursuing her MS degree in optical engineering at Jinan University, Guangzhou, China. Her research interests include patterning of metal nanowires and wearable strain sensors.

Tianwei Liang

Tianwei Liang received his bachelor's degree from the Department of Optoelectronic Engineering, Jinan University, Guangzhou, China, in 2022. He is currently pursuing his MS degree at South China Normal University, Foshan, China. His research interests include assembly of low-dimensional materials and flexible electronics.

mechanical, thermal, magnetic, and plasmonic properties of metals at a low quantity. For this reason, 1D MNWs as building blocks have been widely utilized for constructing various transparent, flexible, and stretchable devices,[4,5] including electronic skins,[6,7] touch screens,[8] smart windows,[9–11] voice recognition systems,[12–14] solar cells,[15] nanogenerators,[16,17] photodetectors,[18] wearable thermal management systems,[19–21] electromagnetic interference shielding,[22,23] *etc.*

In the first decade of the 21st century, most researchers dedicated their efforts to the chemical synthesis of MNWs and performance improvements of MNW networks with random distribution,[24–26] which leads to the loss of the anisotropic properties of a single MNW.[27] Numerous studies have demonstrated that assembling MNWs into micro/nanostructured, aligned, or micropatterned morphologies as functional components in devices can achieve outstanding performances, novel properties, and sophisticated integration architectures. For instance, NW alignment can improve percolation conductivity,[28,29] trigger surface plasmons for polarized surface-enhanced Raman spectroscopy,[30,31] and enhance mechanical strength;[32] self-assembly of MNWs can lead to abundant open areas, highly conductive paths, and/or specific structures, which can improve the mechanical stretchability,[33] optical transmittance,[34] and electrical properties of MNW-based devices;[35] and patterning of MNW networks can improve optoelectronic performance at precise locations,[36] reduce feature size to enhance integration and sensitivity,[37] and form large through-hole contacts on ultra-fine interconnect pitches to realize specific performance.[38] These demonstrations provide a vision for utilizing the unique and outstanding properties of MNW components for various types of applications.[4] Although the precision and repeatability of top-down manufacturing techniques like photolithography and nanoimprinting can be used to manufacture well-defined, ordered MNW structures, it is evident that the shortcomings in terms of a complex process, high cost, and impracticality will limit the further application of MNWs.

To inspire innovation and expedite the utilization of assembly approaches, many reviews on the orientation of 1D-nanomaterials, MNW-based flexible transparent electrodes (TEs), and stretchable electronics have been recently published.[4,39–44] However, there is still a lack of an overview dedicated to the various assembly strategies of MNWs, especially the self-assembly and patterning of MNW networks. Therefore, we present and discuss the recent advancements in assembling techniques of MNWs. The self-assembly strategies of MNWs, such as the coffee-ring effect and ice template methods, are first described to show their advantages of low cost, easy operation, and flexible controllability.[32,34,35,45–51] Subsequently, we discuss the methods to realize the alignment of MNWs, including the classical Langmuir–Blodgett (LB) technique,[30,52–59] assembly in an electric and magnetic field,[60–72] bubble blowing technique,[73,74] electrospinning,[75–81] electrohydrodynamic (EHD) jet printing,[12,82–85] and recently developed assembly at air/solid–liquid interfaces like the Marangoni flow-assisted float assembly.[28,29,86–97] The following section focuses on a variety of patterning approaches to construct high-performance transparent, flexible, and/or stretchable electrodes (SEs), which can be divided into top-down technical routes, including traditional photolithography, adhesion difference-based selective removal,[37] novel Plateau–Rayleigh instability-induced patterning,[98] *etc.*, and the bottom-up strategies such as inkjet printing (IJP) and wetting–dewetting.[99] Lastly, the effects of MNW assembling morphologies on the optoelectrical and electromechanical performances are discussed, and the applications of the assembled MNWs are briefly summarized, aiming to provide basic guidance for device applications. Fig. 1 shows a brief timeline of recent diverse approaches for self-assembly, alignment, and patterning of MNWs and summarizes the involved fluid flows and key processes. This paper presents an all-inclusive review of assembling strategies of MNWs, discusses the underlying mechanisms, assesses the developed strategies, and summarizes representative applications in flexible and stretchable electronics, with the intention of inspiring efforts toward the invention of novel assembly approaches for MNWs, as well as provide guidance for fabricating large-scale, high-performance, new-function MNW-based optoelectronics.[100,101]

Yunhan Luo

Yunhan Luo received his PhD degree in Measurement Techniques and Measuring Instruments from Tianjin University, China, in 2006. From 2011 to 2012, he was a visiting scholar at the University of Michigan for research on microstructured biosensors. He worked as a professor in the Department of Optoelectronic Engineering, Jinan University, China, until 2015. His research interests include micro-nano photonics, optoelectrical electronics, and microfluidic and biomedical photonics.

Gui-Shi Liu

Gui-Shi Liu received his PhD degree in microelectronics and solid-state electronics from Sun Yat-Sen University, Guangzhou, China, in 2018. From 2017 to 2018, he was a visiting scholar at Harvard Medical School for research on biosensors. He joined Jinan University, Guangzhou, China, as an assistant professor in the Department of Optoelectronic Engineering in 2019. His research focuses on assembly of low-dimensional materials for biosensors and wearable electronics.

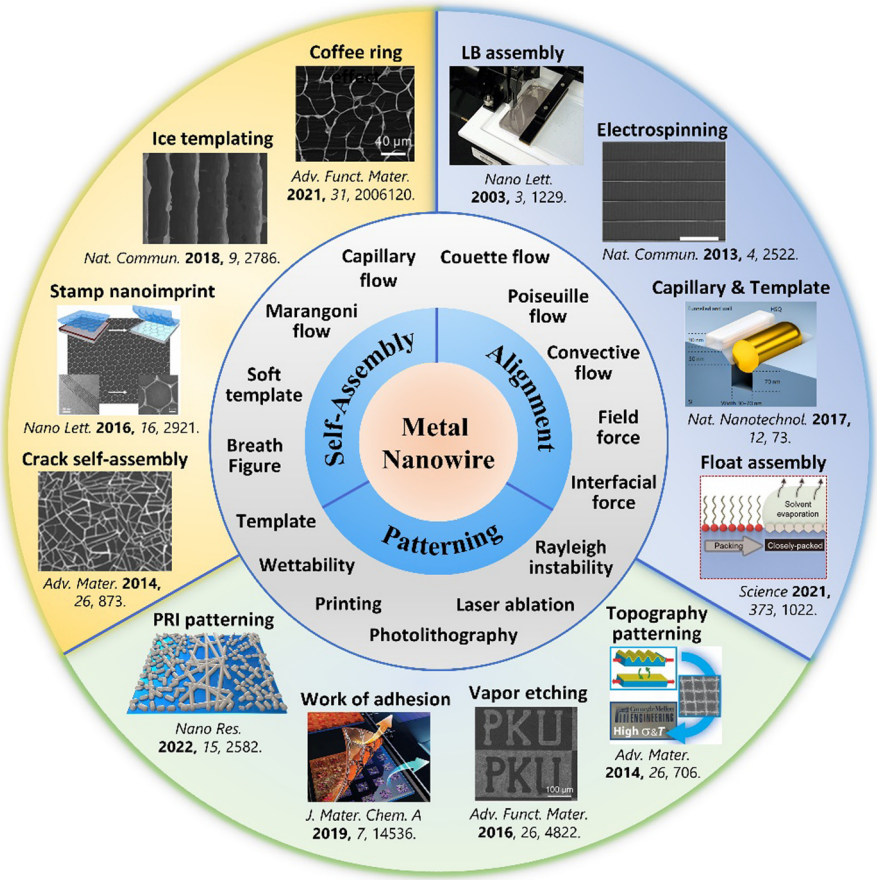

Fig. 1 Summary of self-assembly, alignment, and patterning techniques of MNWs, along with involved fluid processes and parameters. Reproduced with permission.[45,86,87,102–110] Copyright 2013, Springer Nature; Copyright 2015, American Chemical Society; Copyright 2017, Springer Nature; Copyright 2021, American Association for the Advancement of Science; Copyright 2014, Wiley-VCH; Copyright 2016, Wiley-VCH; Copyright 2019, The Royal Society of Chemistry; Copyright 2019, Springer Nature; Copyright 2014, Wiley-VCH; Copyright 2016, American Chemical Society; Copyright 2018, Springer Nature; Copyright 2022, Wiley-VCH.

2. Self-assembly

Self-assembly of liquid-dispersed nanomaterials refers to the process in which nanomaterials spontaneously organize into an ordered, macroscopic structure through a specific liquid thermodynamic process. The structure is guided by a reduction in the system's interfacial/surface energy and/or external actions, mainly including the coffee-ring effect, liquid interfacial force (*e.g.*, bubbles),[47] direct interactions between the nanomaterials, external field (*e.g.*, electric field),[70] and templates (*e.g.*, modified anisotropic substrates).[111,112] The first four strategies are the "extra" template-free assembly methods. In the methods based on the coffee-ring effect and liquid interfacial force, the droplets or liquid–substrate interfaces are generally used as "soft" templates, at the edges of which the MNWs self-assemble after the liquid evaporation.[34,45,47–51,113] The direct interaction method enables the assembly of MNWs into an ordered fiber or pattern but suffers from poor controllability.[32,35,46] The above strategies can yield both specific patterns (nanorings, porous structures, microcircuits, *etc.*) and aligned structures of MNWs. For example, the self-assembly methods based on the coffee-ring effect,[114] templates,[36,114] and external fields[87] are also applicable to the alignment and patterning of MNWs. Due to the numerous studies on the two topics, the self-assembly of MNWs into aligned and orderly patterned structures is described under the Alignment and Patterning sections, respectively.

2.1. Coffee-ring effect-based assembly

The coffee-ring effect refers to the phenomenon in which ring-like patterns are left on a solid substrate after the evaporation of sessile droplets containing non-volatile solutes.[115] The mechanism involved is that the evaporation rate at the inner edge of the droplet is greater than the evaporation rate at the center, which induces an outward capillary flow to carry suspended solutes to the edge of the droplet and form a ring-like deposition.[116] This effect has been widely exploited for deposition of nanoparticles, polymers, and biomolecules,[117] and recently extended to the assembly of MNWs into micromesh-like structures on macroscopic substrates, which mainly serve as high-performance conductors with large optical aperture ratio, high conductivity, and/or large stretchability.[34,45,49]

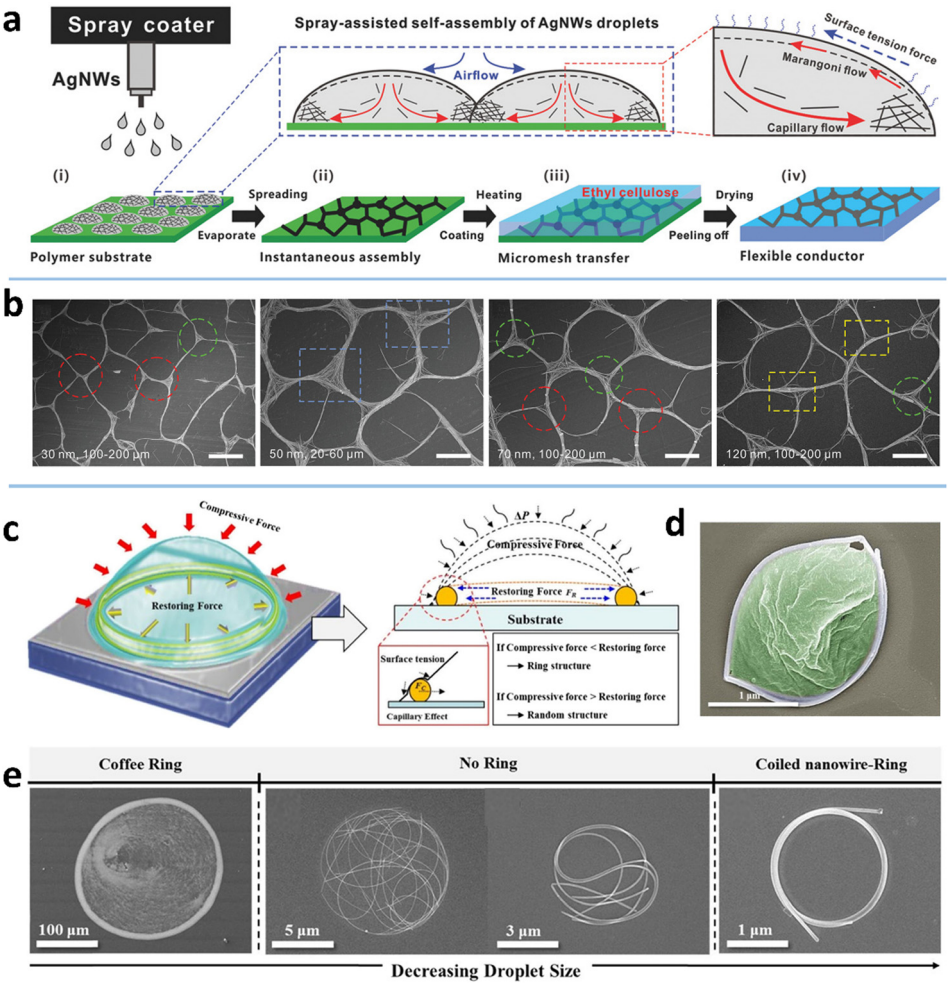

Fig. 2 (a) Fabrication procedure and assembly mechanism of the AgNW micromesh. Reproduced with permission.[34] Copyright 2018, WILEY-VCH. (b) Scanning electron microscope (SEM) image of the obtained AgNW microgrid. Reproduced with permission.[45] Copyright 2021, WILEY-VCH. (c) Formation mechanism of the AgNW ring. (d) SEM image of the AgNW ring filled with polyvinylpyrrolidone (PVP). (e) SEM image of kinked AgNWs with different wetted droplet sizes. Reproduced with permission.[50] Copyright 2017, American Chemical Society.

The deposition pattern of MNWs is closely associated with the capillary flow and Marangoni flow, and their relative strength (Fig. 2a). The two flow processes can be effectively modulated by droplet size and the properties of ink and substrate.[45] Using an atomization method to control the droplet size, Seong *et al.* achieved three kinds of ring-shaped AgNW structures (Fig. 2e).[50] For large droplets with low evaporation rates, the AgNWs tend to be deposited along the circumference of the droplets *via* the capillary effect, yielding an AgNW ring with a thick rim and sparse deposition within the ring (the far left of Fig. 2e). With the decrease in droplet size and thus increased evaporation rate, the NW deposition is no longer dominated by the capillary flow and forms the coiling of AgNWs inside the small droplets. When the droplet diameter drops below a specific size, the deformed AgNWs form a nearly perfect ring. If a polymer material is dissolved in the solvent, a polymer-filled AgNW ring can also be achieved (Fig. 2d). As indicated in Fig. 2c, the final morphologies generated by the small droplets are guided by the relative values of the restoring force (F_R) of the NW, arising from the NW length larger than the droplet size, and the compressive force (F_C), a net force from liquid surface tension exerted on the NW surface.[118,119] A stronger compressive force ($F_C > F_R$) can strongly bend the NWs to form a ring shape; the converse leads to randomly kinked NWs inside the droplet.

High wettability of the NW ink on the substrate can induce a quick-spreading flow and rapid evaporation to produce uniform deposition within the droplet.[114] Xiong *et al.* demonstrated that a hydrophobic substrate (perfluoroalkoxylalkane, PFA, with a water contact angle of 108.2°) facilitates the pinned droplets to expedite the capillary flow and suppress the Marangoni flow, giving rise to a microgrid structure through a spray-assisted process (Fig. 2a and b).[34,45] Comparative experiments suggest that the substrates with surface tension higher than 25 mN m^{-1} are not suitable to form AgNW-bundle meshes for the IPA ink with AgNWs of diameter >20 nm due to the limited driving force within the spreading droplets on the substrates. As for the ink, a higher surface tension (by adding water into the IPA ink) has a larger contact angle and thus a

smaller contact area, making the droplets slip freely during the slow evaporation of water. The coffee-ring effect is therefore weakened to form a uniform deposition of AgNWs.

MNW dimension also has a marked impact on the self-assembled morphology. It is easier to drive nanoparticles than the heavier MNWs under the capillary flow.[120] The drop-casting of ethanol-dispersed AgNWs (diameter 200 nm and length 30 μm) on silicon yields relatively uniform deposition with a slightly thick rim.[114] With a smaller size (*e.g.*, diameter 40 nm and length 25 μm), most AgNWs can be transported to the rim by the capillary flow, yielding a ring-like deposition and micro-meshed structure.[50] The shorter AgNWs form a mesh with larger bundles and knots (Fig. 2b), because the same weight ratio per unit area has a higher amount of the shorter NWs than the longer NWs.[45] The resultant micromesh has a lower performance in terms of both conductivity and transparency. At a given length, the AgNWs with small diameters self-organize into a mesh with smoother knots, better connection, and thinner bundles due to the lower amount and better ductility of the thinner NWs, which results in higher conductivity and transmittance. It is also demonstrated that the AgNWs with higher aspect ratios form a mesh with larger cells and thicker bundles at high concentrations ($\geq$2 wt%), while the results are mixed at low concentrations.[49] One of the resultant TEs has a sheet resistance ($R_S = RW/L$, where R, W, and L are resistance, width, and length, respectively) of 25 Ohm sq^{-1}, an ultrahigh transmittance (T) of 97%, and a low haze (deviation degree of transmitted light) of 2.6%.[34]

To sum up, the assembly texture *via* the coffee-ring effect can be easily tuned and optimized by adjusting the properties of the solvent (including surface tension, volatilization rate, viscosity, *etc.*), MNW dimension, concentration and composition of the ink, surface energy of substrates, and the deposition method (spray coating, rod-coating followed by heating, *etc.*). Modulation of the coffee-ring effect can be achieved by controlling (i) the pinning of the contact line, (ii) the outward capillary flow, (iii) the Marangoni reflux, and (iv) the interaction between the liquid interface and NWs. The most prominent feature of this effect is the template-free assembly into specific patterns. Using a multi-nozzle spraying system, one could easily scale up the ring formation through the coffee-ring effect for mass manufacture of MNW-based TEs.

2.2. Ice template assembly

Interfaces are the most important assembly platform for the MNWs dispersed in solvents. With the use of different types of interfaces, such as the liquid–liquid interface and the solid–liquid interface, various strategies including freeze casting,[36,121,122] breath figure (BF) method,[51,123] bubble templates,[47,48] LB assembly,[56] crack-direct assembly,[111,112] *etc.* have been developed for self-assembly of NWs into 1D, 2D, and 3D structures. These strategies can realize either aligned NWs or NWs organized into microporous structures. The alignment of NWs will be discussed in a separate section, considering the numerous publications on this topic.

Ice templating is a versatile solid–liquid interface-based technique for assembling various materials into porous structures.[121] It is not until the 2010s that the ice templating gained much attention in MNW assembly.[109,124–130] Typically, ice templating involves the controlled freezing of a liquid or liquid hybrid, freeze drying of the solvent (mostly water), and subsequent posttreatment (*e.g.*, thermal annealing) if necessary.[121] During the freezing process, the solvent solidifies into patterns that serve as a template, where the solidification front repulses solid nanomaterials to follow the template. Afterward, the ice template is removed by sublimation, leaving the nanomaterial-formed framework.

The most common type of structure assembled by the ice template technique is the 3D cellular-like hierarchical architecture (Fig. 3a), *i.e.*, AgNW-based aerogel.[109,124,125] The 3D cells are induced by the parallel ice fingers which are formed during ice crystals sweeping along with the solidification front. The AgNWs are rejected and condensed into the spaces between the ice fingers. In this way, the 2D AgNW networks with interconnected 3D cells are assembled into a macroscopic monolith. This MNW-based porous structure offers a new way to achieve ultrahigh ratios of conductivity to weight, *e.g.*, a conductivity of 1.3 S cm^{-1} at a density of 1.3 mg cm^{-3},[125] with tunable electromechanical stability. By combining the 3D MNW framework with hydrogels or elastomers one can construct high-performance stretchable and piezoresistive conductors. Yu *et al.* presented a first example of the combination of the sulfhydryl compound-modified 3D AgNW aerogel and a hydrogel (poly(*N*-isopropylacrylamide)) as the stretchable conductor,[109] which has a cellular architecture with a ternary structure: NW network, cellular microstructure, and macroscopic assembly with hydrogel cross-linking. Unlike the elastomer-filled NW framework, the hydrogel-conjugated cellular-like AgNW structure effectively dissipates the crack energy to withstand a tensile strain of 800% with a minor change in resistance.

The ice template technique has also been extended to the 2D assembly of MNWs into a porous and ordered network. One strategy is the direct transformation of the 3D cellular structure into a 2D porous network during the ice thawing by the use of the high flexibility of ultrathin MNWs and the NW capillary coalescence.[127] The other is the utilization of the salt-controlled recrystallized ice crystals as the 2D template for MNW assembly (Fig. 3b).[131] The ice crystals at −80 °C were subjected to annealing at a higher temperature to trigger the recrystallization, leading to the growth of the crystals. The crystal size can be easily tuned by adding different ions and changing the annealing temperature. In this way, the mesh size and bundle width of the assembled 2D AgNW mesh can be regulated to achieve desirable optoelectrical performance and stretchability. Besides the porous network, an orderly patterned 2D network has been reported by directionally freezing a liquid film at a controlled velocity (Fig. 3c).[36] By simultaneously freezing from two directional cold sources, '>' shaped and orthogonally crossed patterns can be fabricated (Fig. 3d). The TE prepared from low-dose AgNWs exhibits an R_S of 20 Ω sq^{-1} and a T of 91%.

2.3. Other types of interface assembly methods

The BF is another natural phenomenon which provides guidance for micro/nano fabrication. One example is the fog

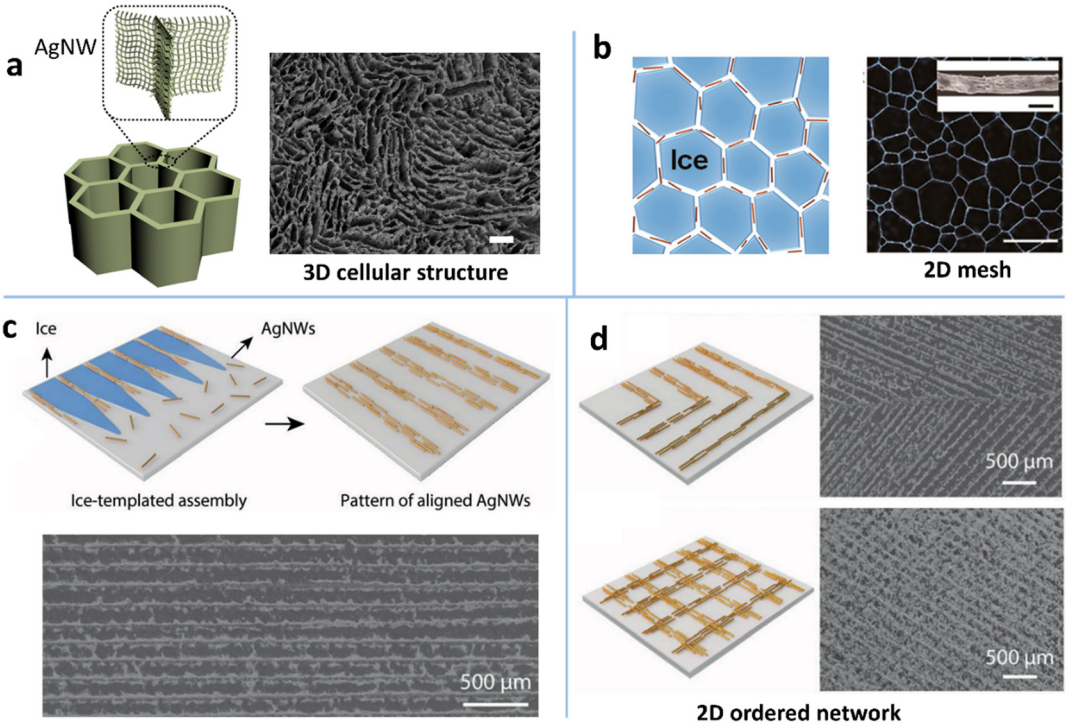

Fig. 3 (a) Illustration of the structure of 3D ice-templating AgNWs and the corresponding SEM image. Reproduced with permission.[109] Copyright 2018, Springer Nature. (b) Schematic of the 2D recrystallized ice template method and the optical microscope (OM) image of the assembled 2D AgNW mesh. Reproduced with permission.[131] Copyright 2017, American Chemical Society. (c) Schematic of the 2D ice-templating method for ordering and patterning AgNWs and the corresponding SEM image. (d) Schematic and SEM images of '>' shaped and orthogonally aligned AgNW patterns fabricated by the 2D ice-templating approach. Reproduced with permission.[36] Copyright 2021, WILEY-VCH.

formed on a cold glass when we breathe upon it. The BF method can induce the formation of the honeycomb macroporous pattern (HMP) of MWNs with high transparency and conductivity.[132] The typical BF method involves cast coating of a nonpolar, low-boiling point solvent, and harvest of water droplets on a substrate.[123] The two-phase system serves as a soft template to induce a porous pattern of nanomaterials (Fig. 4a).[133] He *et al.* used chloroform to disperse AuNWs and cast the dispersion on the Si substrate which was then placed in a closed humid container.[51] As the solvent evaporates, small water droplets condense to form a droplet-array on the substrate.[4] The AuNWs can self-assemble at the edge of the droplets to form the HMP when the water droplet-array evaporates completely (Fig. 4b). The concentration and length of AuNWs and the surrounding humidity are the critical parameters for the static BF method. For example, humidity affects the condensation of water, which in turn affects the size of water droplets and the shape of the hole-array. With a similar idea, Shin *et al.* achieved an AgNW microgrid on polyethylene terephthalate (PET) by rod-coating a formulation that consisted of AgNWs and three solvents (DI water, methanol, and α-terpineol).[49] The three solvents constitute a multi-phase system to yield a soft template during evaporation. Since the vapor pressure of α-terpineol is 10^7 times higher than that of methanol, evaporation leaves two immiscible fluids: α-terpineol and water. The α-terpineol droplet separates the water containing AgNWs to form a cell-like separation texture with concentrated NW bundles after complete evaporation. The cell-shaped pattern not only improves the conductivity but also creates a high aperture ratio to have high transparency, showing an R_S of 25.44 Ohm sq^{-1} at 88.42% transmittance and 3.71% haze.

Likewise, other multi-phase induced interfaces have been developed to manufacture various metal grids with abundant open areas. Gong *et al.* reported a simple air–water interfacial self-assembly technique to fabricate a meshed TE using ultrathin AuNWs (diameter ≈ 2 nm).[134] The aged AuNW hexane solution was drop-cast on the air–water interface. The immiscible hexane floated on the air–water interface and evaporated to assemble the AuNWs into a mesh-like network. Due to its ultrahigh aspect ratio (>10 000) and small diameter, the network was comprised of serpentine bundles with an average thickness of 193.7 nm and pore sizes of 8–52 μm. The bundle formation may arise from the partial removal of oleylamine ligands from the AuNW surface. The AuNW network exhibits an R_S of 130.1 Ohm sq^{-1} at 92% transmittance. Khatri *et al.* created the bubble-based air–liquid interfaces to guide the mesh formation of AgNWs.[47] The AgNW water dispersion was bubbled using the surfactant sodium dodecyl sulfate and the thickening agent lauryl dimethylamine oxide. The bubbled solution was then cast and sandwiched between two substrates to form the meshed AgNW network after drying.

Using vertically aligned carbon nanotubes (ACNTs) on glass as a solid interface, Bian *et al.* assembled AgNWs into multi-dimensional ordered textures *via* fibrous elastocapillary coalescence

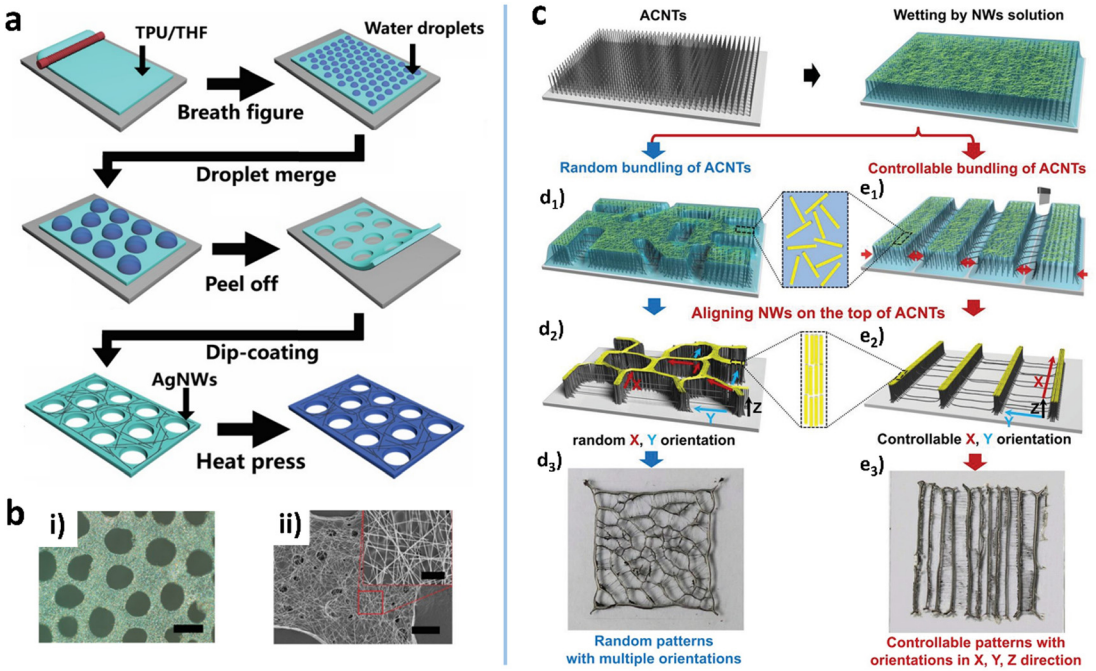

Fig. 4 (a) Schematic illustration of the fabrication process for the porous HP-AgNW/TPU film. (b) Optical (i) and SEM (ii) images of the porous AgNW/TPU film. Reproduced with permission.[133] Copyright 2020, American Chemical Society. (c) Schematic of ACNT-assisted self-assembled multidimensional structures of NWs. (d_3–e_3) Digital images of the assembled NW micro-structures. Reproduced with permission.[35] Copyright 2019, WILEY-VCH.

(Fig. 4c).[35] Due to its surface texture and inherent hydrophilicity, the ACNT can be gradually wetted by the AgNW water solution.[135,136] Under the action of strong capillary force and van der Waals interaction, the ACNT fibers coalesce into a micropattern, on the top of which the AgNWs are densely arranged into the same pattern.[137] Meanwhile, CNT filaments are drawn out and crossed over the mesh of the micropattern (Fig. 4c(d_3–e_3)). As a result, the multidimensional ordered AgNW/CNT hybrid micropatterns are formed, exhibiting a good piezoresistive effect with a sensitivity of 0.32 kPa^{-1}.

3. Alignment

MNWs have distinct anisotropic physical properties which cannot be manifested and exploited in disordered structures. This section summarizes the methods to achieve macroscopic ordered in-plane MNW networks in which the long axes of individual MNWs are more or less parallel to each other (*i.e.*, in alignment). The alignment strategies can be categorized into shear force-based approaches, LB technique and its variants, and electromagnetic field methods.

3.1. Shear force-based alignment

3.1.1. Shear flow phenomenon. A viscous fluid flowing over a solid substrate will experience shear force from the substrate surface. A 1D NW suspended in a liquid is subjected to asymmetric torque under a shear force,[138] leading to rotation of the NW to be aligned lengthwise along the flow direction. Since Huang *et al.* proposed a microfluidic flow method to achieve alignment of MNWs in 2004, a variety of shear force-based methods have been exploited for NW alignment, including inkjet printing,[31,83–86,139–146] spin/dip/rod/blade/slot-die coating,[12,90,93,147–150] wetting–dewetting,[151] microfluidic channel flow,[152] forced convection,[29] bubble blowing,[73,74,153,154] nanocombing,[97] *etc.*

In most cases, the system can be simplified as either the parallel-plate Couette flow or pipe Poiseuille flow. For the most frequently used IJP and rod/blade/slot-die coating, a meniscus connecting the substrate to the printing/coating head is also involved during the NW deposition. Therefore, the alignment of NWs is the synergistic action of shearing speed, solvent viscosity, height of the wetting film, solvent evaporation, NW aspect ratio, NW concentration, capillary action, and/or substrate properties. Fig. 5a illustrates the various flows and interactions affecting the NW alignments near the boundary. Without involving or before entering the meniscus, the alignment degree is mainly determined by the velocity field which has a linear profile for the Couette flow and a parabolic profile for the Poiseuille flow. In both cases, a higher shearing rate yields a higher degree of alignment for NWs.[29,155] However, the orientation of a few NWs in the obtained samples deviates from the shear force direction because there is thermal relaxation before NWs adhere to the substrate. The relaxation can be evaluated by the Peclet number (Pe) and Reynolds number (Re). The Peclet number can describe the relative strength between hydrodynamic and diffusion forces of the NW in the liquid flow, given by[156]

$$\mathrm{Pe} = 3\dot{\gamma}\mu l^3/k_B T \ln(R) \quad (1)$$

where $\dot{\gamma}$, μ, l, k_B, T, and R are the shear rate, shear viscosity of the solution, length, Boltzmann constant, temperature, and

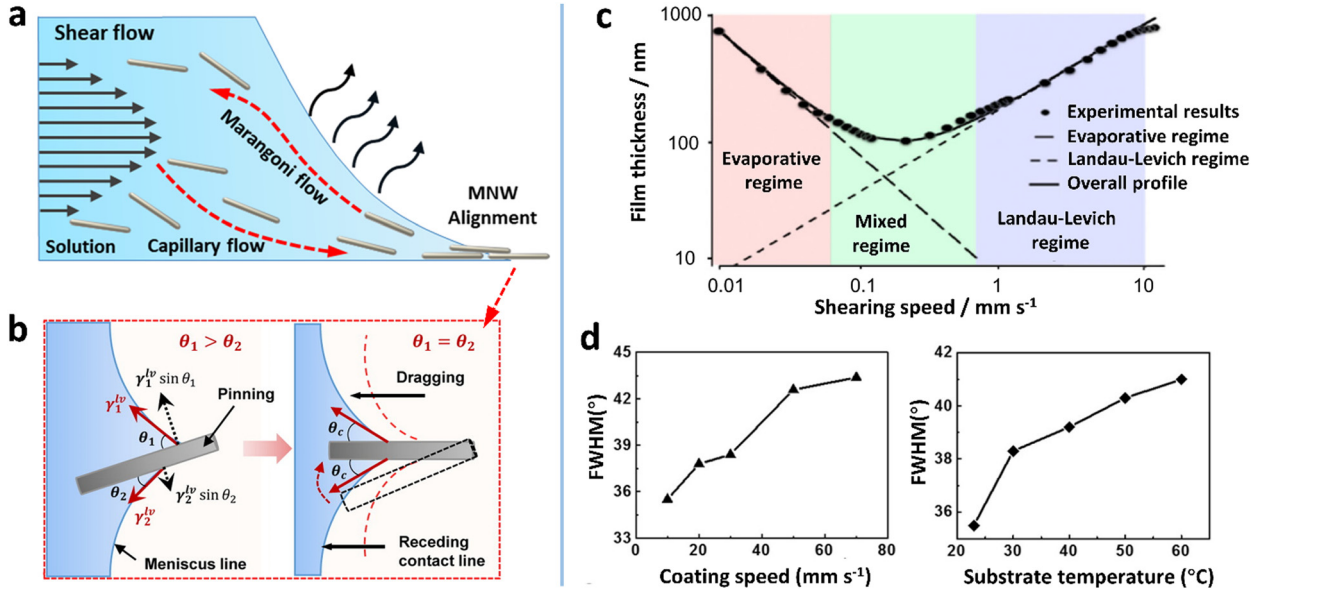

Fig. 5 (a) Schematic of flows underlying the shear flow-guided coating that can influence the orientation of MNWs. (b) MNWs aligned by a nano-patterned PDMS stamp and the capillary action at the air–liquid–solid contact line. (c) Two deposition regimes as a function of coating speed. Reproduced with permission.[157] Copyright 2018, Springer Nature. (d) FWHM values as a function of coating speed and substrate temperature. Reproduced with permission.[91] Copyright 2017, American Chemical Society.

aspect ratio of the NW, respectively. The NW motion is dominated by the flow field for Pe $\geq$ 1 but by the Brownian fluctuations for Pe $<$ 1.[156] The Reynolds number quantifies the influence of inertial forces compared to viscous forces, described by[157]

$$\mathrm{Re} = \rho v L/\mu \quad (2)$$

where ρ, v, and L are the fluid density, mean fluid velocity, and gap distance/pipe diameter, respectively. To maintain the aligned state of the NW in fluid over long periods before deposition on the substrate surface, high Pe and low Re numbers are desirable. According to eqn (1) and (2), the Brownian motion of NWs can be depressed by adjusting fluid viscosity, shear rate, aspect ratio of NWs, and coating gap/microchannel diameter. It is experimentally demonstrated that adjusting the solution viscosity with PVP polymer to 20–30 cP yields very large Pe (10^5–10^7) and very small Re (10^{-6}–10^{-3}), making AgNW alignment unchanged for more than 6000 s,[138] and increasing the substrate temperature reduces the alignment degree of the bar-coated AgNWs (Fig. 5d).[91]

The fluidic system is more complicated if a meniscus near the substrate is involved. Due to enhanced evaporation in the front of the meniscus, a capillary flow carrying NWs toward the contact line can be induced. In the meantime, a surface tension gradient along the meniscus may be generated depending on the solvent, which triggers a Marangoni flow to recirculate NWs back toward the deposition head (Fig. 5a). At the contact line, the pre-alignment NWs are subjected to unbalanced capillary forces to further improve the alignment degree (Fig. 5b). According to the flow speed, there are two deposition regimes: "evaporative regime" in which film thickness decreases with coating/printing speed and "Landau–Levich (LL) regime" in which film thickness increases (Fig. 5c).[157] In the evaporative regime, low shear rates lead to the disordering of the MNWs through their rotation along Jeffery orbits under a small Reynolds number.[158] A minimum coating speed of $\approx$1 mm s^{-1} is required for a shear force-based alignment of the AgNWs.[91] Therefore, for highly aligning MNWs, the coating speed values reported in the literature are in the range of 0.5–100 mm s^{-1},[86,91,94,96] which are located within the LL regime. With a LL meniscus, the thickness (h) of the liquid film can be given by the capillary number (Ca = $\mu v/\sigma$) as follows:[157]

$$h = k\mathrm{Ca}^{3/2}R_\mathrm{d} \quad (3)$$

where k, σ, and R_d are the constant of proportionality, surface tension, and meniscus radius, respectively. It is evident that the film thickness continuously increases with the coating speed. Accordingly, a lowered alignment degree of AgNW with an increased coating speed has been experimentally observed in rod or blade-like coating.[86,91,94] This can be ascribed to the thicker liquid film hindering the formation of a uniform receding meniscus during the evaporation and allowing more free rotation of the NWs far away from the boundary constraints.[91,158] It has been shown that modifying the substrate with positively charged functional groups, which may suppress the rotation process *via* electrostatic interaction, facilitates improving the alignment degree of AgNWs.[91]

3.1.2. Shear force-based techniques

Bubble blowing. Bubble blowing is one of the classic shear force-based methods for NW alignment.[73,74,153,154] This method generally involves three steps: (1) preparation of polymer solution containing NWs; (2) expansion of the NW dispersion with a ring centered over the gas outlet, which was moved upward while introducing gas, and (3) transfer of the bubble film onto the target substrate. In this method, the NWs are

oriented in the thin polymer film and at the interface between the film and the substrate, not in a fluid as in most shear-force based approaches. The MNW alignment is driven by the shear forces generated at the gas outlet and the interface upon attaching the receiving substrate, as well as by the tension force arising out of bubble blowing. Cao *et al.* used this method to align TeNW networks and *in situ* transformed the straight TeNWs into buckled nanosprings during the blowing process (Fig. 6g).[73] This group also constructed sausage-like nanoblocks containing graphene nanotubes and CuNWs in the bubble film, which can enhance the antioxidation of Cu and reduce the linear resistance of graphene.[159] Large-area crossed-aligned NW networks have been realized by the bubble-blowing method for application in gas sensors and FETs.[160] This low-cost technique can print NWs on various substrates, whether their surfaces are flat, rigid, or not. However, two drawbacks remaining for this method are the control of density and distribution of MNWs on the substrate and the polymer matrix residing in the NW film which may decrease optoelectrical performance such as conductivity.

Fluid convection. Fluid convection-induced shear force is a simple strategy for NW alignment. Heating and mechanical agitation have been used to induce the convection of MNW dispersion.[28,29,162] A prestrained poly(ethyleneimine) (PEI)-coated polydimethylsiloxane (PDMS) film was placed on the wall of a beaker, in which the AgNW dispersion was magnetically agitated.[29] The cationic polymer PEI was used to anchor aligned AgNWs in the agitated flow *via* electrostatic interaction. The alignment degree was improved by increasing solvent viscosity and agitation speed, but there existed an optimized viscosity for the highest orientation degree (Fig. 6b). The agitation at 800 rpm achieved around 50% of the NWs aligned within $\pm 10^{\circ}$. By assembling AgNWs twice with orthogonal direction, a mesh-like AgNW network was achieved. The prestrain-induced tangled AgNW network shows a high stretchability of 40%, with a special positive relationship between the strain and conductivity. Heating the solvent in a beaker is another strategy to induce convection-based alignment.[28,162] As shown in Fig. 6a, inhomogeneous heating causes an uprising stream and a down-flowing stream of water at the center and rim of the beaker, respectively.[28] When a small droplet of NW solution (*e.g.*, ethanol[162] or IPA[28] as the solvent) is drop-cast on hot water, the NW solution can quickly spread out on the water surface without NW precipitating or mutual dissolution, which may be caused by the interface heat convection arising from the temperature gradient between the mild droplet and hot water. The shear force induced by the Marangoni effect

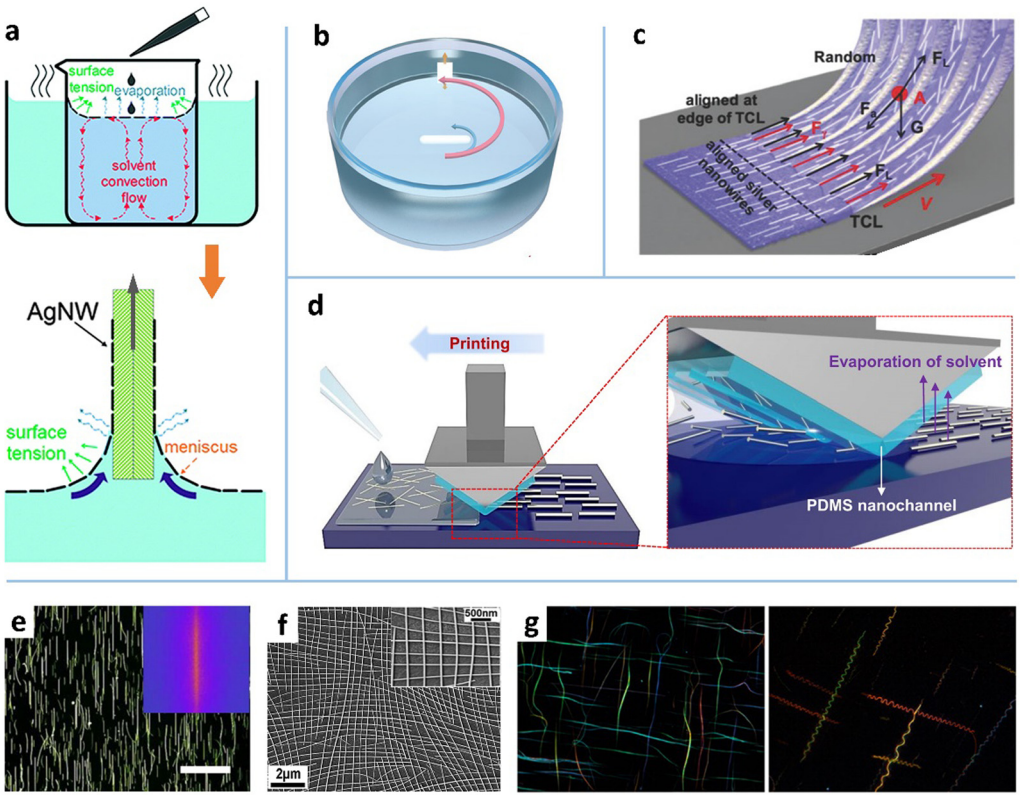

Fig. 6 Schematic illustrations of the (a) water-bath assisted convective assembly, (b) agitation-assisted alignment, (c) conical fiber array-guided alignment, and (d) capillary printing. (a–d) Reproduced with permission: ref. 28, Copyright 2015, The Royal Society of Chemistry; ref. 29, Copyright 2019, WILEY-VCH; ref. 161, Copyright 2018, WILEY-VCH; ref. 86, Copyright 2015, American Chemical Society. (e) OM images of the capillary-printed unidirectional AgNWs. Reproduced with permission.[86] Copyright 2015, American Chemical Society. (f) SEM image of the convective flow-assembled bi-aligned AgNWs. Reproduced with permission.[28] Copyright 2015, The Royal Society of Chemistry. (g) OM images of the crossed spring-shaped TeNWs. Reproduced with permission.[73] Copyright 2014, American Chemical Society.

at the interface actuates the orientation of the AgNWs to form a shiny mirror-like layer when the solvent evaporates. The aligned AgNWs can be easily transferred to the target substrate by dip coating. Likewise, a crisscross NW mesh can be obtained by two-times dip coating (Fig. 6f). The major drawback of the bubble blowing and fluid convection-based methods is their impracticality in large-area fabrication.

Bar coating. Bar coating is a simple yet effective method to generate large-area aligned MNW networks.[90–93,96] The bar here refers broadly to various sweeping heads including rod,[94] Meyer rod,[91,92,96] blade/plate,[149] slot-die,[163] structured bar,[86] and even hairbrush.[161,164] The NW alignment is not only induced by the shearing action underneath the bar, but is also affected by the downstream meniscus which involves capillary flow, Marangoni flow, and the capillary force at the contact line (Fig. 5a). In the LL coating regime, a higher coating speed (0.5–100 mm S^{-1}) leads to a thicker meniscus and a lower alignment degree,[94] indicating that the meniscus action dominates the NW alignment. It is reported that more than 85% of MNWs align within $\pm 30^\circ$ at a coating speed of 10 cm s^{-1}.[96]

To further improve the alignment degree, efforts have been devoted to spatial heterogeneity of the bar and substrate. Takemoto *et al.* modified a substrate into a hydrophobic/hydrophilic patterned surface to provide additional boundary constraints for the glass-rod coating of AgNWs, reducing the R_S by 6.8 times.[90] Likewise, a structured coating head can provide physical guidance for MNW deposition. Our group first used the Meyer rod to achieve the aligned and bi-aligned AgNWs, which reduces the R_S of the network by more than 50%, compared with the random AgNW network.[92] Ko *et al.* modified the Meyer rod coating technique by preconjugating the PET substrate with poly-L-lysine to increase the AgNW adhesion to the PET *via* an electrostatic force.[91] Similarly, mounting the coating bar with nano-patterned PDMS has been developed to more accurately guide the deposition of AgNWs. As shown in Fig. 6d, the PDMS with a line pattern spacing of 400 nm was attached to a trigonal prismatic frame, the sharp peak of which was in contact with the substrate, to sweep the AgNW solution on the substrate, producing a highly aligned or bi-aligned AgNW network (Fig. 6e). More recently, Liu *et al.* utilized the Chinese brush, composed of a conical fiber array (CFA), to achieve a highly oriented AgNW&PEDOT:PSS composite film (Fig. 6c). The conductivity of the CFA-aligned AgNW network along the brushing direction is over 270 times that of the spin-coated AgNW network. The advantages of the structured bar coating are that it provides additional geometric constraints which improve the alignment degree and evades the additional process requirements, such as transferring, substrate pre-patterning, and pre-grown vertical NW arrays, which are essential for other alignment approaches.[4]

Printing. Printing is another primary class of alignment technologies for MNWs, in which the gravure printing, IJP, and EHD jet printing have been reported to have alignment effects on AgNWs.[165] The gravure printing shares a similar alignment mechanism with the blade coating for MNWs. The former differs from the latter in that the ink is coated onto engraved structures of a substrate and then transferred onto the target substrate. The gravure printing method has shown a full width at half-maximum (FWHM) value of 64.5° (smaller value indicating higher alignment degree), higher than the values of the capillary and Meyer-rod coating methods (Table 1). For the IJP and EHD jet printing (Fig. 7a), the shear force can be generated both on the surface of the jet stream and in the printed solution film. The two methods can precisely control the MNW deposition in terms of alignment, position, direction, and NW density. Different from the pressure-induced

Table 1 Alignment degree of MNWs assembled by different methods

Nanowire	Method	Alignment degree[a]	Application	Ref.
AuNWs	Langmuir–Schaefer technique	±10°	Chiral ultrathin films	56
AgNWs	Wetting–dewetting	39.8°	Electrodes	151
AgNWs	Dip coating	15°–75°	—	88
AgNWs	Dip coating	17.3°–23°	Strain sensors	167
AgNWs	Bar coating	35°	Flexible TEs	90
AgNWs	Bar coating	21.4°	Flexible TPs	91
AgNWs	Bar coating	±30°	Solar cells	96
AgNWs	Bar coating	82°	TEs	12
AgNWs	Shear force	57°	—	168
AgNWs	Shear force	±30°	SEs	29
AgNWs	Gravure printing	64.5°	—	140
AgNWs	EHD printing	±10°	Heaters and ECG[b] sensing	139
AgNWs	Capillary printing	40°–65°	LEDs and solar cells	86
AgNWs	Inkjet printing	±30°	SEs	82
AgNWs	Grazing incidence spraying	±15°	—	169
AgNWs	Substrate stretching	±10°	—	93
TeNWs	Bubble blowing	<7°	Photodetectors and gas sensors	73
AuNWs	Printing and electric field	22°	Muscle-tissue regeneration	84
CuNWs	Assembly by magnetic field	8 ± 4°	—	61
FeNiCo NWs	Magnetic field and microgroove	15 ± 1°	—	62
AuNWs	Assembly by electric field	5°	—	69

[a] Alignment degree is characterized by FWHM. [b] ECG: electrocardiogram.

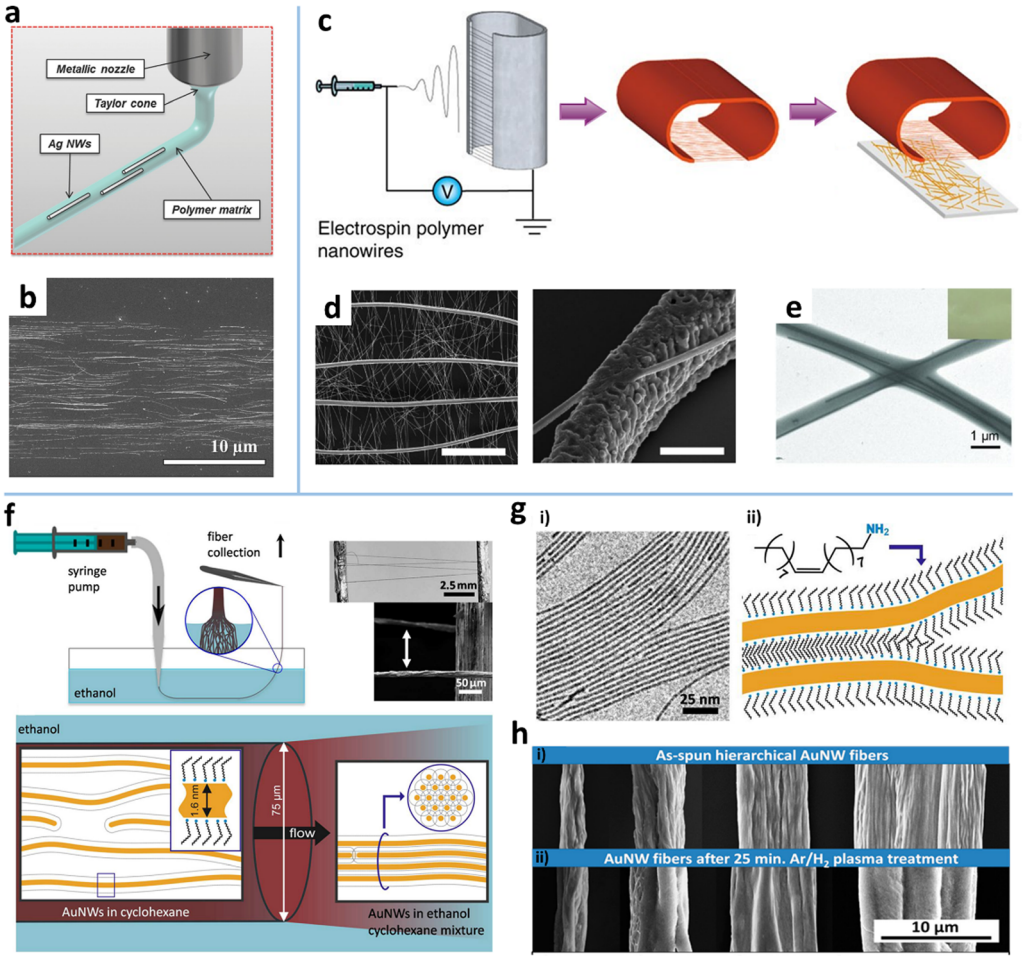

Fig. 7 (a) Schematic of the EHD jet printing and (b) a corresponding SEM image of the aligned AgNWs. Reproduced with permission.[85] Copyright 2014, WILEY-VCH. (c) Schematic of an electrospinning method for fabricating the aligned CuNWs–AgNW composite and (d) a corresponding SEM image of the aligned CuNWs integrated with random AgNWs. Reproduced with permission.[102] Copyright 2013, Springer Nature. (e) TEM image of the electrospun fabricated PVP nanofibers containing aligned AgNWs. Reproduced with permission.[75] Copyright 2012, WILEY-VCH. (f) Schematic of injection of AuNWs into ethanol and beam formation at the single NW level. (g) (i) TEM image of washed AuNWs and (ii) schematic illustration of two AuNWs with interacting ligand layers. (h) SEM images of AuNW fibers spun with different AuNW volume fractions before and after plasma treatment. Reproduced with permission.[32] Copyright 2017, American Chemical Society.

ink extrusion in IJP, the EHD jet printing utilizes an electric field to induce a conical ink meniscus at the nozzle tip so that the ink is ejected from the meniscus to form high-resolution patterns with printed features down to submicron size.[166] The resultant MNWs are highly aligned without perceptible deviation, as shown in Fig. 7b.[85] An additional benefit of the printing techniques is that the printed aligned MNWs can be easily constructed into a specific array or pattern with high resolution and performance,[31,165] which will be described in Section 4.

Pipe ejecting. Printing-like pipe ejecting techniques, electrospinning and solution spinning, have also been exploited to align AgNWs and AuNWs.[75,76,80,81,170] The electrospinning technique was first developed to fabricate polymer fibers with diameters ranging from tens of nanometers to a few micrometers.[102] As the electrostatic force generated by a high voltage overcomes the surface tension of the polymer droplet, a thin charged jet is formed and accelerated toward the grounded collector to produce ultrathin fibers (Fig. 7c). High alignment of the electrospun nanofibers can be easily realized by various auxiliary setups or external fields.[171] The electrospun polymer nanofibers are used as either the matrix for containing MNWs or the template for further metallization to form MNWs. For the matrix strategy, MNWs can be aligned and incorporated into the nanofiber matrix by adding MNWs into the electrospinning solution.[75] Fig. 7e shows the aligned AgNW incorporated into PVP nanofibers. The AgNWs with a high aspect ratio show a higher alignment degree than the Au nanorods with a small aspect ratio.[172]

In the nanofiber-templated scheme, the key is to metalize the nanofibers to form MNWs. There are four main ways of metalizing nanofibers: calcination and reduction,[77] thermal evaporation,[102,173,174] electroplating,[175,176] and electroless deposition.[177,178] In the first method, the mixture of a metal precursor and a carrier polymer is electrospun to form raw nanofibers which are then subjected to calcination to obtain metal oxide nanofibers by removing the polymer, followed by

reduction to turn the metal oxide into metal. The thermal evaporation is a more straightforward method, where the metal is thermally evaporated onto the electrospun polymer fibers to form metalized NWs after selectively dissolving the supporting polymer. Using this method, the Cui group fabricated a free-standing nanowire-like (nanotrough) network and a hybrid of aligned Cu mesowire (CuMW) and AgNWs *via* an additional transferring (Fig. 7c and d).[102,173] It is shown that the aligned CuMW can decrease the R_S of the NW TE by an order of magnitude without degrading T, showing R_S = 0.36 Ω sq^{-1} at T = 92%. To avoid the high-temperature annealing or high-vacuum process, An *et al.* combined electrospinning and electroplating to produce a self-welded CuNW network.[179] This method involves five steps: (i) noble-metal seeding on polymer fibers *via* vacuum sputtering or electroless non-vacuum chemical bath deposition to achieve sufficient electrical conductivity; (ii) electrospinning a supporting polymer fiber layer; (iii) electroplating in a copper electroplating solution for a few seconds; and (v) transferring the CuNWs onto target substrates and removing the supporting layer. To further simplify the process, Yang *et al.* proposed an electroless deposition of Cu on electrospun poly(4-vinylpyridine) (P4VP) NWs.[179] The P4VP NWs as templates can be seeded with catalyst Pd nanoparticles in $PdCl_2$/HCl solution due to the strong affinity of pyridyl groups to metal ions. The Pd NPs as catalysts induce reduction of Cu precursors onto the PVP NWs. The advantages of the electrospinning method are that high alignment of MNWs can be achieved at a macroscopic scale and more complex hierarchical alignment structures can be readily realized by controlling the arrangement of the electrospun fibers. It should be noted that the MNWs made by calcination, electroplating, and electroless deposition have rough surfaces, leading to lower conductivity. The performances of the resultant TEs are lower than those of MNWs fabricated by vacuum thermal deposition.

Solution spinning. Alignment of MNWs can also be achieved by solution spinning that utilizes intermolecular non-covalent interactions between MNWs to induce their self-assembly into freestanding fibers.[32] In a study reported by Beate *et al.*, the AuNWs in the cyclohexane dispersion are injected into the antisolvent ethanol to form fiber-like precipitates (Fig. 7f). When pulled across the ethanol–air interface, the fibers composed of loose AuNWs will be compressed by capillary forces. The ethanol induces fully interdigitated ligand layers (oleylamine) between adjacent AuNWs to yield tight bundling (Fig. 7g and h (i)). The bundles can be fully annealed by plasma treatment, forming porous NWs with continuous gold shells (Fig. 7h (ii)). The breaking stress of the well-aligned bundle is 25% higher than that of the poorly aligned bundle. The bundle fibers can be used to construct small electronic circuits or to form nanoscale interconnections.[108]

3.2. Langmuir–Blodgett technique and its variants

The LB assembly technique is one of the most classic methods for aligning nanomaterials, including NWs,[53,87,100,180] NPs,[181,182] nanotubes,[55,183] and nano-films.[30,52,54,184] A macroscopic LB assembly-like phenomenon is the ''logs-on-a-river'', where the narrow river width causes the woods to be aligned along the flow direction. This alignment mechanism also applies to 1D nanomaterials. Typically, the 1D NWs diffusing on the surface of organic solvents generate a randomly distributed and loosely stacked NW network (Fig. 8a).[185] Using a baffle with controllable surface pressure and barrier velocity to compress the layer on the liquid surface, a high-density aligned Langmuir monolayer film can be obtained (Fig. 8b). The aligned single-layer films can be repeatedly deposited by vertical immersion or horizontal lifting techniques, which can prepare nano-films with specific thickness or multi-alignments. For example, Wang *et al.* reported a transparent electrochromic film based on an ordered NW network with tunable conductivity (7–40 Ω sq^{-1}) and transmittance (58–86% at 550 nm), which was obtained by depositing two layers of aligned NWs with crossing angles.[186] The film-forming process was carried out under normal temperature and pressure, and it did not change the properties of the material itself. So far, ordered NW films, such as AgNWs,[54] vanadium dioxide NWs,[187] and germanium NWs,[188] have been prepared by LB technology. Although the LB technique has demonstrated its versatility for NW assembly, it also has several drawbacks: NWs have to be surface functionalized, the LB process is slow, and the condition control is rigid, otherwise, NW array films are not uniform.

A few attempts have been made to overcome the above issues of the LB method. To avoid inhomogeneities that appear commonly in film transfer in the LB technology, Ana *et al.* reported a modified LB technique for AuNWs, which incorporates a meniscus-assisted float assembly on a liquid (Fig. 8c).[53] A concave meniscus of hexane containing AuNWs is established on diethyleneglycol. The solvent evaporation rate is faster in the middle of the meniscus to induce NW compression at the liquid–air interface,[189] which causes the AuNWs to be densely arranged with good alignment on a Teflon recipient (Fig. 8d).[190] This process produces an almost defect-free dense NW monolayer with 2 nm thickness, showing a high T of 96.5% at a low R_S (400–500 Ohm sq^{-1}). Yang *et al.* developed a shear-assisted-Langmuir technique to align NWs.[52] The NWs are first dispersed at the air–water interface in a funnel container and compressed by draining the water out of the funnel, accompanied by rotating the water by a polyrod to induce shear force that aligns the MNWs. Compared with the traditional LB technique, this method can produce aligned MNWs faster.

Recently, D. H. Kim *et al.* proposed an LB-like float assembly method to fabricate a dense aligned AgNW nanomembrane.[87] Unlike the conventional LB technique, the NW compression in this method is induced by Marangoni flow at the water–oil interface, where the ''oil'' made of AgNWs, ethanol, and water-immiscible solvent elastomer floats on the water (Fig. 8e). The Marangoni flow is induced when the ethanol in the ''oil'' dissolves into the water to form a surface tension gradient. In the meantime, the water-immiscible elastomer solution floats on the water to create the oil–water interface, at which the AgNWs tend to settle due to the amphiphilic ligand (polyvinyl pyrrolidone). To further pack the AgNWs on the water, a few

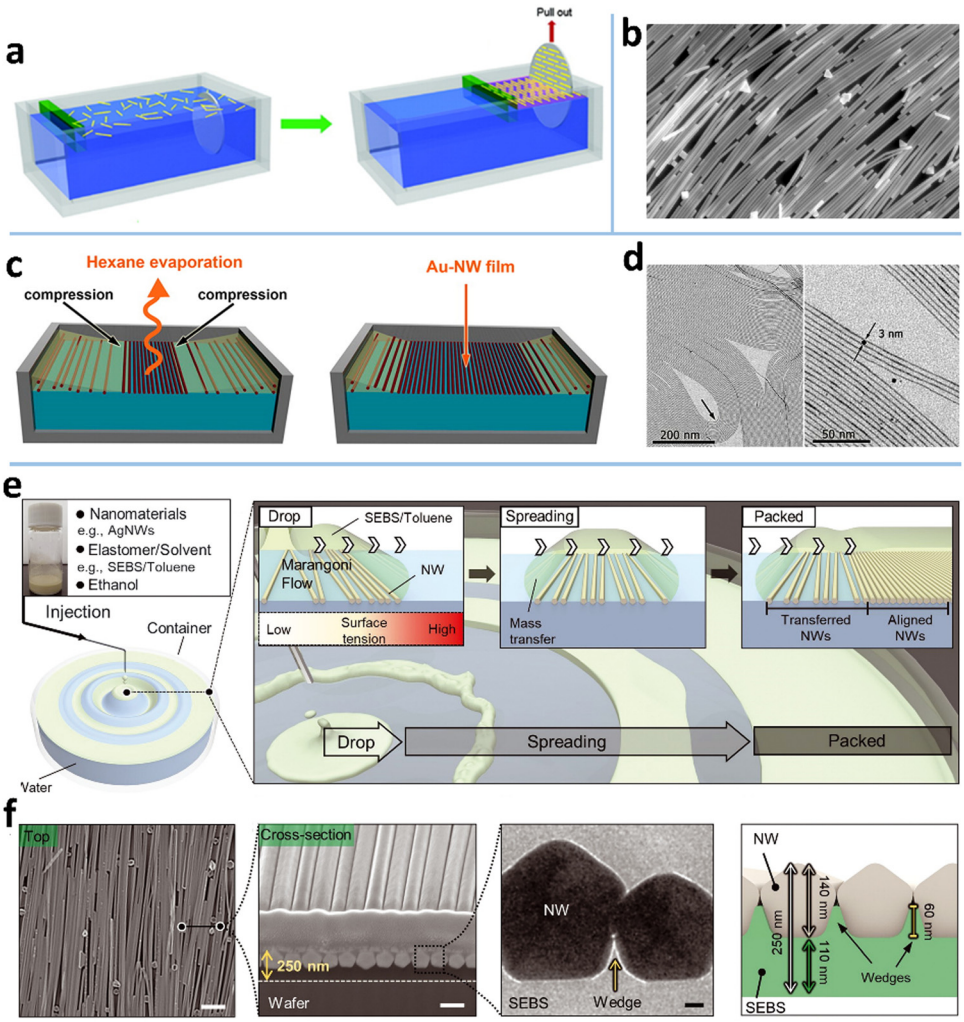

Fig. 8 (a) Schematic of the LB assembly process. Reproduced with permission.[100] Copyright 2012, American Chemical Society. (b) Aligned AgNWs achieved by the LB assembly method. Reproduced with permission.[180] Copyright 2012, American Chemical Society. (c) Schematic of the convection-assisted technique for fabrication of AuNW monolayer films and (d) the TEM images of the assembled AuNWs. Reproduced with permission.[53] Copyright 2012, American Chemical Society. (e) Schematic of a float assembly method for fabricating a compact, aligned AgNW nanomembrane. (f) SEM and TEM images, and structure diagram of the aligned AgNW nanomembrane. Reproduced with permission.[87] Copyright 2021, American Association for the Advancement of Science.

surfactant drops are dripped into the film center to induce Marangoni flow again. One advantage of this method over the LB assembly is that the aligned NW monolayer is partially embedded in an ultrathin elastomer film after the solvent in the "oil" evaporates (Fig. 8f). This film can be used as a skin electrode or transferred to target substrates for other uses.

3.3. Electromagnetic field methods

3.3.1. Alignment in a magnetic field. The magnetic field can be used to align MNWs along the lines of magnetic force.[60–63] This method is only applicable to NWs either made of or modified with magnetic materials, such as nickel NWs (NiNWs) and Fe_3O_4-modified AgNWs (Fe_3O_4–AgNWs).[191,192] In a magnetic field, thousands of magnetic NWs can be aligned in one step and form a head-to-tail chain. Oleksandr *et al.* utilized non-uniform magnetic fields to fabricate aligned Fe_3O_4–AgNW networks (Fig. 9a–c).[63] By changing the direction of the magnetic field and depositing layer by layer, the AgNWs can be assembled into a network structure with biaxial orientation. Besides, the frequency of an applied rotating magnetic field can facilely control and induce tumbling, precession, or rolling of CoPt NWs with semihard magnetic properties, which are synthesized by template-assisted galvanostatic electrodeposition.[193] Nevertheless, the alignment degree of long NWs is still not satisfactory. The defeat in alignment is partly caused by the NW bending during the deposition due to its high aspect ratio,[63] and may also arise from the magnetic force not being strong enough to overcome the hydrodynamic resistance and friction force.

Two processes govern the ordered deposition of NWs in the magnetic field: NW rotation in suspension along the direction of the magnetic field line and NW approaching the substrate *via* NW–interface interaction. The rotation is closely related to the applied magnetic field strength, NW length, and solvent properties. Increasing the magnetic field strength has been

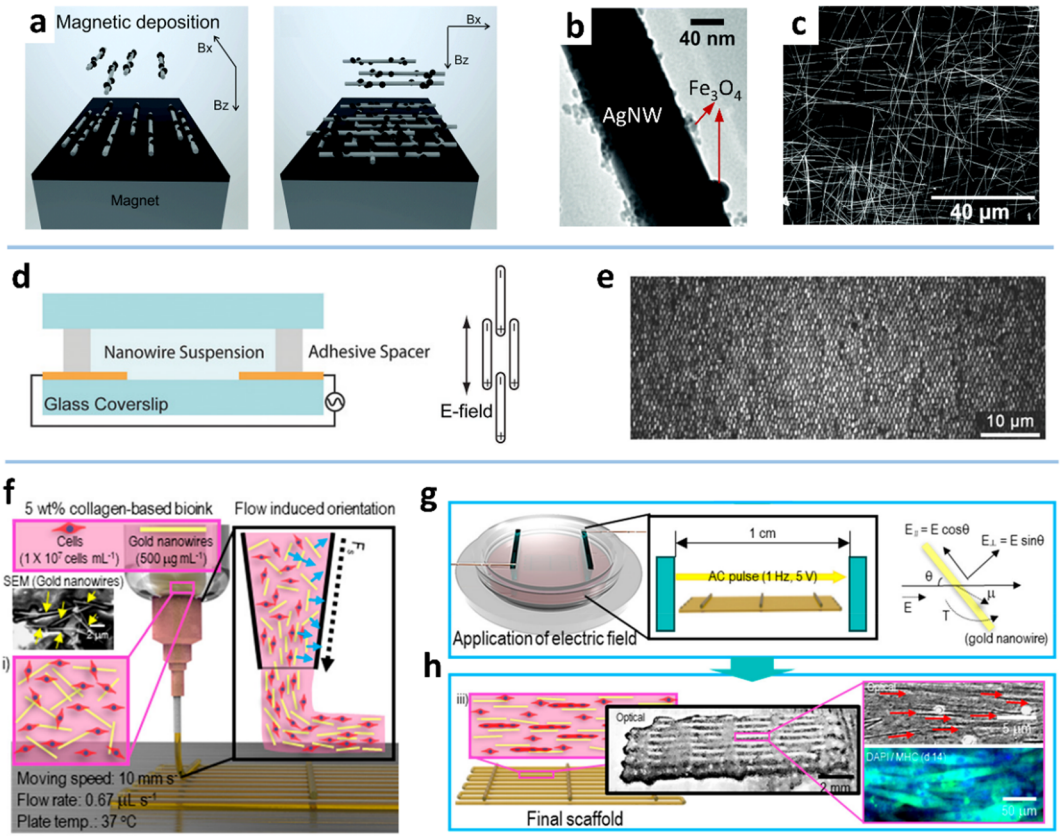

Fig. 9 (a) Illustration of the alignment of Fe_3O_4–AgNWs in the magnetic field. (b) TEM image of the Fe_3O_4–AgNW. (c) SEM image of the bi-aligned Fe_3O_4–AgNWs. Reproduced with permission.[63] Copyright 2015, RSC Pub. (d) Schematic of the electric field-induced assembly of AuNWs. (e) Reflected light OM image of AuNWs. Reproduced with permission.[194] Copyright 2016, WILEY-VCH. (f) Schematic of the cell-printing process. (g) Schematic of the applied electric field for aligning AuNWs. (h) Schematic and optical/fluorescence images of the cell-laden collagen/aligned AuNW structure. Reproduced with permission.[84] Copyright 2019, American Chemical Society.

shown to improve the alignment degree.[62] At a given magnetic field strength, the shorter NWs can align better with the direction of the magnetic field before deposition on the substrate because the shorter NW has a higher velocity than a longer NW.[62] The properties of the solvent, such as viscosity, also should have an impact on the NW alignment under a magnetic field, but there is still a lack of research on this topic. On the other hand, NW approaching the surface can be controlled by combining the magnetic field and heterogeneous substrates, as auxiliary templates, to improve the alignment degree. The geometrically structured substrate (*e.g.*, microtrench) can physically fix the NWs along the topography to reduce the MNW dislocation under a magnetic field.[62] Even without a magnetic field, MNWs can be roughly aligned along the micro-grooves due to the capillary action of the radial outward flow and the high specific gravity of MNWs.[104] The chemically patterned substrate can also increase the interaction between the MNWs and the substrate to form a better alignment.[61,195] For instance, the carbon-doped silicon dioxide (CDO) substrate is selectively functionalized with thiol functional groups by photolithography,[196,197] so that the Ni-modified CuNWs can be chemically anchored to the exposed thiol groups and selectively removed by a lift-off process. The prepared NW array exhibits high conductivity and good corrosion resistance because of the Ni shell.[198]

3.3.2. Alignment in an electric field. Dielectrophoresis between patterned electrodes is another alternative route for aligning dielectric NWs.[64–72] The dielectric NWs can be synthesized from metals and metal oxides using a templated cathodic electrodeposition.[199] Essentially, an alternating electric field is created between the electrodes to capture and orient the NWs until they cross the gap between the electrodes (Fig. 9d). This process is called positive dielectrophoresis. It requires the dielectric constant of the NW material to be higher than that of the surrounding medium. Otherwise, the NWs will deviate from the electrodes due to negative dielectrophoresis. The alignment degree depends on the distribution and strength of the electric field. Under a non-uniform electric field, the MNWs tend to be aligned along the field gradient line and attracted to the nearest electrode.[199] Due to their high aspect ratios, the induced dipole moment of the NWs promotes their self-assembly into an ordered array to a degree (Fig. 9d and e), which is proportional to their electrical conductivity. In order to reduce the degree of NW interlacing, the length of the MNWs should remain as consistent as possible, and the gap between the electrode pairs should be equivalent to this length, so that

the MNWs can bridge the gap after alignment and deposition.[200] For instance, Freer *et al.* reported the self-limiting assembly of single NWs with 98.5% yield on 16 000 electrode sites covering 400 mm^2.[64] Also, crossed MNW networks can be obtained by layer-by-layer deposition with orthogonal electric fields. The MNWs aligned by dielectrophoresis have been used to fabricate various functional components, such as light-emitting diodes, resonators, and mechanical oscillators.[65,94,201,202] Kim *et al.* gained the myoblast alignment with aligned AuNWs, which were achieved by a cell-printing process assisted with an electric field (Fig. 9f–h).[84]

The MNWs behave differently in a direct current (DC) and an alternating current (AC) electric field.[69,203] In a DC electric field, according to $qE = K\eta v$ (where K is the drag coefficient, E is the electric field intensity, and η is the viscosity), the MNWs eventually move at a speed v, but the direction is random. The movement of MNWs in the AC field is determined by a dielectrophoretic (DEP) force: $F_{DEP} = 1/2\varepsilon_m \mathrm{Re}(K)\nabla E^2$ (where ε_m is the dielectric constant of the medium, K is the Clausius–Mossotti coefficient). It is clear that the MNWs have no tendency to move in the AC electric field, but they will align in the same direction. Fan *et al.* used hybrid dielectrophoresis to align and transport MNWs based on this property.[69] When a mixed DC and AC electric field is applied to the MNWs, they can control the NW direction while maintaining a linear trajectory. The DC and AC electric field intensity and direction angles can be appropriately adjusted by engineering electrode configuration.

On the whole, significant advances have been made in the development of alignment techniques, which are classified into three kinds: (1) shear flow-induced alignment; (2) LB approach and its variants; and (3) electromagnetic force-guided deposition. Advanced strategies have already reduced the alignment degree (characterized by FWHM) to $\leq 15^\circ$, roughly in the descending order LB technique > electromagnetic field method > shear flow approach (see Table 1). The shear flow approaches such as rod coating have excellent manufacturability at a compromised FWHM, whereas the LB techniques can yield a highly aligned, compact MNW film and the electric field-based methods enable precise assembly of MNWs between electrode couples.

4. Patterning

MNW networks need to be patterned to improve performance, realize new functions, or construct integrated devices. The reported patterning approaches for MNWs can be classified into top-down and bottom-up strategies. Top-down strategies are those in which uniform networks of MNWs are first deposited on substrates and then carved into specific patterns. Lithography,[37,106,204–220] Plateau–Rayleigh instability (PRI) method,[98,221–224] and laser ablation[225–230] are the representative top-down techniques. In contrast, bottom-up strategies are those that directly organize MNWs into a particular structure on substrates, typically including printing,[139,140,143,231–240] wetting–dewetting self-assembly,[99,151,241–244] and template assisted patterning.

4.1. Top-down strategy

4.1.1. Photolithography

Photoresist-based photolithography. Photolithography is the most widely used patterning technology which was initially developed for fabricating semiconductor integrated circuits in the 1960s. In early reports, photolithography is combined with electrodeposition to achieve patterned NWs of noble metals (gold, palladium, platinum, or bismuth).[245,246] A temporary sacrificial template (nickel or silver) is fabricated by photolithography to act as a plating electrode which produces the patterned MNWs with 5–200 nm height and 0.011–2 μm width. More often, photolithography is used for patterning synthesized MNWs, which is elaborated in the following.

A key feature of photolithography is the pattern transfer from a photomask to a photoresist coating by light exposure. The method typically includes six steps: MNW deposition, liquid photoresist overcoating on the MNWs, pattern transfer, developing, selective removal of MNWs, and photoresist stripping (Fig. 10a and b).[204,217] After developing the photoresist layer,[211] structured access to the MNW network is produced to allow selective removal by wet/dry etching or exfoliation. Wet etching is the most commonly used, which employs liquid etchants to corrode MNWs. The etching effect can be improved either by adjusting the composition ratio and the pH value,[209,247,248] or with external assistance such as sonication and oxygen plasma treatment, to shorten the processing time and achieve high-precision patterning.[210,213] Dry etching mainly refers to processing MNWs using the physical and chemical processes generated by plasma discharge.[249,250] There is also a report of using a neutral iodine vapor, as an etchant, to etch the exposed AgNWs, which achieves a pattern resolution of 5 μm with sharp edges.[105]

To avoid using environmentally hazardous or expensive etching processes, etching-free photolithographic methods have been developed for patterning MNWs. One is to use the dry film photoresist (DFR) to replace the liquid photoresist. The DFR can be directly laminated with MNW networks with no need for homogenization, baking, and curing. The MNWs underneath the UV-exposed DFR can be selectively removed by stripping the DFR or washed away by ethanol.[212,251] The fabricated AgNW electrodes with a minimal linewidth of 50 μm show clear edges.[212] The other is the lift-off technique which begins with photoresist patterning and then coating of the MNW film on the pattern, followed by selective removal of the MNWs through photoresist stripping (Fig. 10c and d).[214–216] The graphene–AgNW composite is patterned into a minimum linewidth of 20 μm (Fig. 10e and f). Nevertheless, the above etching-free photolithography still requires the photoresist processes, including patterning, developing, and removing, which are complex, costly, and not environmentally friendly.

Photoresist and etching-free photolithography. This method modulates the adhesion of MNWs to the substrate to achieve patterning with external force such as physical exfoliation and ultrasonication.[37,106,218,252] According to the adhesion theory, adhesion arises from mechanical interlocking, physical adsorption, chemical bonding, diffusion, and electrostatic charges.[106]

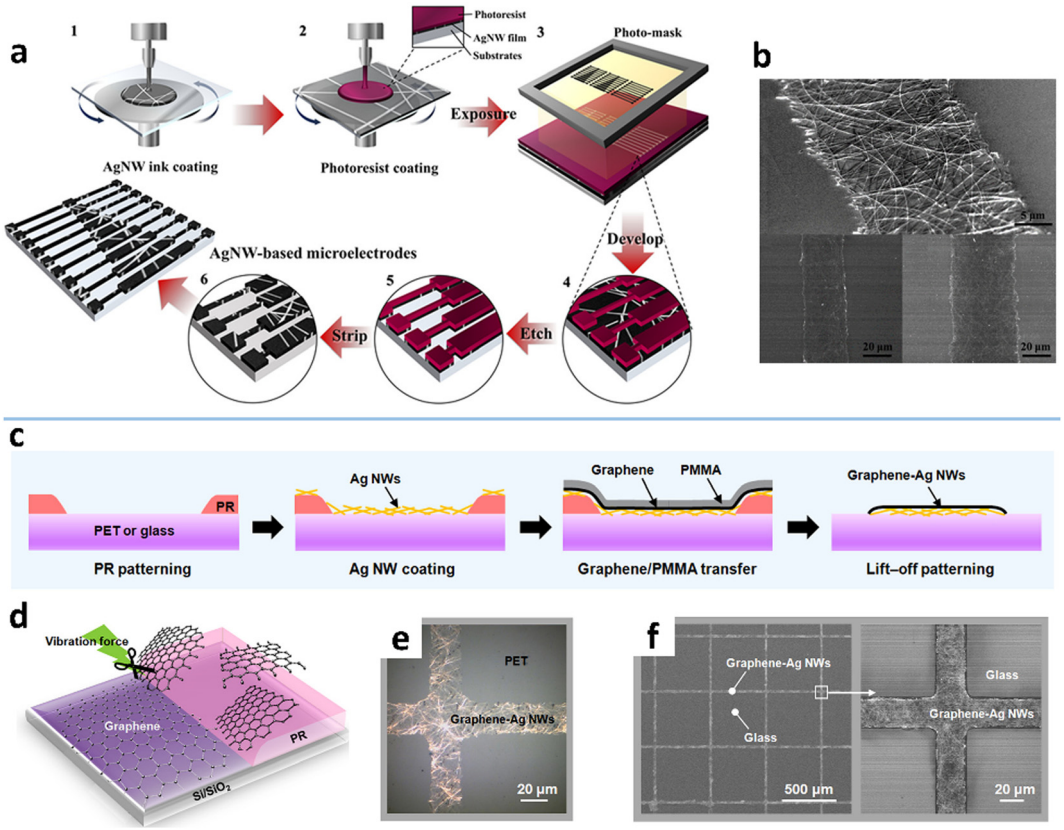

Fig. 10 (a) Fabrication procedure of AgNW microelectrodes by a photoresist-based photolithographic process and (b) the fabricated AgNW patterns. Reproduced with permission.[204] Copyright 2014, American Chemical Society. (c and d) Schematic of a lift-off photolithographic process for the graphene–AgNW composite. (e) OM and (f) SEM images of the graphene–AgNW patterns. Reproduced with permission.[216] Copyright 2017, American Chemical Society.

Physical adsorption, mechanical interlocking, and chemical bonding are the most frequently used to increase the adhesion between AgNWs and substrates.[253–256] Considering a sandwich structure comprised of a UV-curable polymer, a AgNW network, and a substrate, the transfer of the AgNW network onto the target substrate is dependent on the difference between the mechanical interlocking strength ($W_{\text{poly-AgNW}}$) and the physical adsorption strength ($W_{\text{AgNW-substrate}}$) (Fig. 11a). The physical adsorption strength between two films is characterized by the work of adhesion ($W_{1,2}$)[106]

$$W_{1,2} = 4\left(\frac{\gamma_1^{\text{d}}\gamma_2^{\text{d}}}{\gamma_1^{\text{d}}+\gamma_2^{\text{d}}} + \frac{\gamma_1^{\text{p}}\gamma_2^{\text{p}}}{\gamma_1^{\text{p}}+\gamma_2^{\text{p}}}\right) \quad (4)$$

where γ_1^{p} and γ_2^{p} are the polar surface energies, and γ_1^{d} and γ_2^{d} are the nonpolar surface energies of materials 1 and 2, respectively. Kim *et al.* used UV/O_3 treatment to control the surface energy of the substrate and thus the work of adhesion ($W_{\text{AgNW-substrate}}$) through a shadow mask, which yielded an AgNW-exposed pattern and an AgNW-embedded pattern after delaminating the sandwich structure. The physical adsorption mechanism dominates this patterning strategy. Similarly, the selective exfoliation of AgNWs can be achieved by adjusting the mechanical interlocking strength of a UV-curable pressure-sensitive adhesive (PSA) film. The AgNWs were deposited on a Teflon substrate with low surface energy and laminated with a UV-patterned PSA film (Fig. 11b), in which the exposed region showed low adhesion and high hardness, and the soft unexposed region allowed for embedding of AgNWs in the PSA under mechanical pressure. After further UV curing, the embedded AgNWs can be selectively exfoliated by the cured PSA film due to the mechanical locking.

Intense pulsed light (IPL) has also been utilized to realize the mechanical locking-based patterning of MNWs (Fig. 11c and d). The surface plasmon polariton (SPP) of MNWs can be excited by IPL to generate high local heat. The underlying polymer substrate is partially melted to make the MNWs embedded in the substrate, thereby enhancing the adhesion due to mechanical locking (Fig. 11c).[258–261] Meanwhile, the strong electromagnetic coupling at the junctions of MNWs is triggered under the IPL to induce plasmonic nano-welding of MNWs, which significantly improves the conductivity of the MNW network. Selective adhesion of the MNW network is obtained by IPL exposure through a photomask. The unexposed MNWs can be easily recycled or removed by swabbing, taping, or ultrasonic cleaning.[219,220,262] Combined with a roll-to-roll (R2R) system, this method can produce patterned flexible MNW TEs continuously.[220] The prerequisite for this method is that the substrate must be a thermoplastic material, such as colorless-polyimide (cPI), PET,

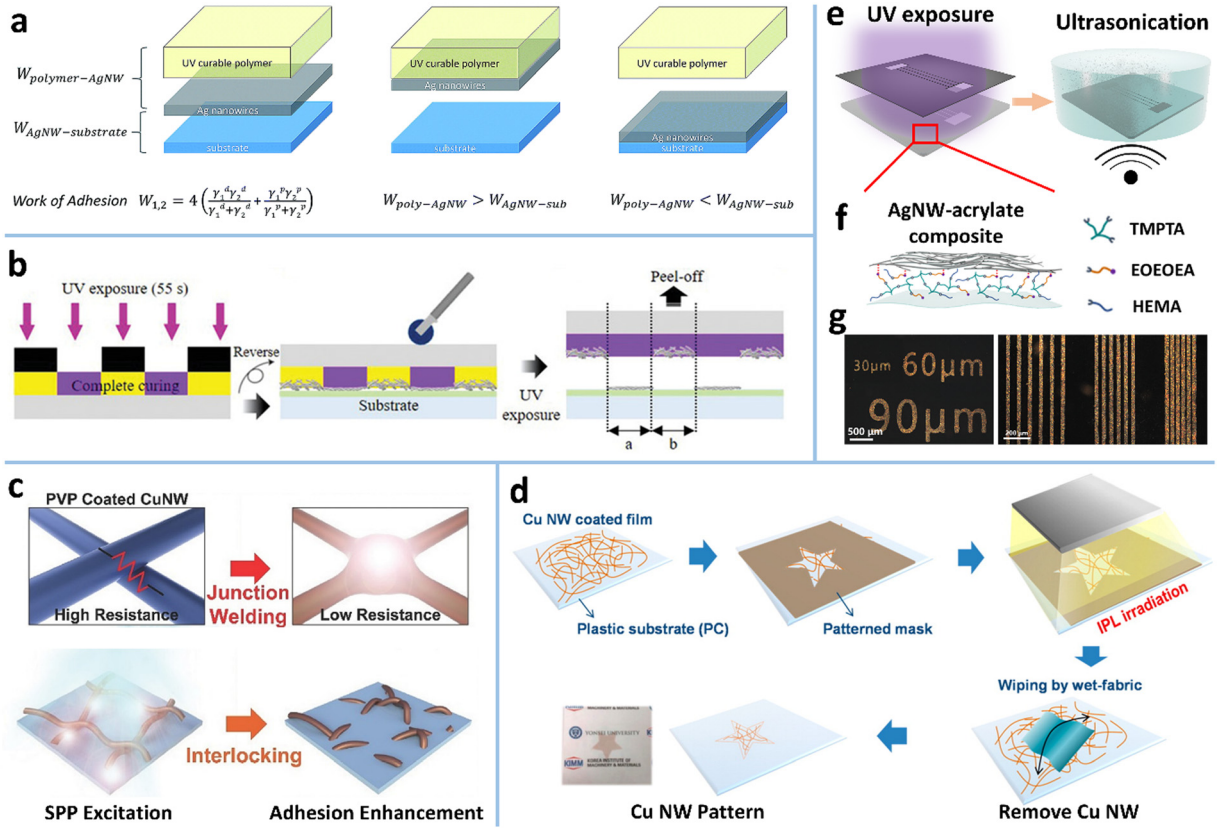

Fig. 11 (a) AgNW patterning based on the difference in work of adhesion between AgNWs and two different substrates. Reproduced with permission.[106] Copyright 2019, Royal Society of Chemistry. (b) Schematic of the UV-curable adhesive film-based photolithographic method for AgNWs. Reproduced with permission.[257] Copyright 2021, WILEY-VCH. (c) Schematic of the IPL-induced nano-welding and interlocking of CuNWs. Reproduced with permission.[258] Copyright 2017, WILEY-VCH. (d) IPL-based patterning process of CuNW electrodes. Reproduced with permission.[220] Copyright 2016, American Chemical Society. (e) One-step photolithographic patterning method of AgNWs based on (f) a photosensitive AgNW-acrylate composite ink. (g) OM images and photograph of the AgNW patterns on PDMS with different sizes and line spacing. Reproduced with permission.[37] Copyright 2020, American Chemical Society.

polyethylene naphthalate (PEN), and thermoplastic polyurethane (TPU), to ensure that it can be melted by SPP-induced heat.[219,252,263] It should be noted that excessive high irradiation energy would cause the breakdown of MNWs and thermal deformation of the polymer substrate.

Chemical bonding-modulated adhesion based on photosensitive inks has also been exploited to achieve MNW patterning. Our group developed a photosensitive AgNW ink that functions as both a photoresist and an adhesion promoter to achieve etching-free one-step photolithographic patterning of AgNWs (Fig. 11e).[37] The ink is comprised of AgNWs, ethanol, acrylate monomers, and a photoinitiator (Fig. 11f). The coated AgNW–acrylate composite film was selectively irradiated by UV light. The exposed film was polymerized and had strong adhesion to the hydroxylated PDMS surface due to the hydrogen bonding effect, while the unexposed film was water-soluble and could be removed by ultrasonication in water. This process yields well-defined AgNW micropatterns with a line width of 30 μm and a line spacing of 10 μm (Fig. 11g).[37] Similarly, photosensitive *N*-methyl-4(4′-formylstyryl) pyridinium methosulfate acetal (sbq-PVA) and PEI were also used to prepare a photosensitive AgNW ink.[264] The difference from the above method is that the AgNWs in the UV-irradiated region are buried and insulative in the cured polymer, while the AgNWs in the shadowed region are retained through the adsorption of PEI and exposed after rinsing sbq-PVA with water. The resultant pattern shows tiny optical visibility.

4.1.2. Lithography. Conventional lithography uses wettability-patterned substrates that can accept and repel ink into an image for transferring the imaged ink to target substrates. There are some revised lithographic methods for patterning MNWs, including micro-stamp contact and etching,[265] subtractive stamp transfer,[236] and mechanical locking-based removing.[218,237] The first approach is similar to the conventional photolithography. The only difference is that the protective layer is inked by the micro-stamp for the subsequent chemical etching. The latter two methods are based on the adhesion difference to remove MNWs selectively.

The most common strategy is to insert an adhesion promoter between MNW films and substrates. Poly(methyl methacrylate) (PMMA) templates as the mechanical locking layers have been printed on AgNW networks by IJP to achieve MNW patterning (Fig. 12a).[218] The uncovered AgNWs can be selectively removed from the substrate by wiping with wet tissue or peeling off with

tape, giving rise to patterns with a linewidth of 60 μm. If polyvinyl alcohol (PVA) film was coated on the PMMA-patterned AgNWs and peeled off, the positive and negative AgNW patterns with minimal size down to 10 μm are simultaneously achieved.[238] The disadvantage of this method is the additional requirement of removing the PMMA template. To avoid dissolution of the chemical, the toner containing a polymer binder was printed into an image on a copy paper, which was used to transfer the AgNWs on a hydrophobic film by a hot-press process (Fig. 12b and c).[237] The transferred AgNWs without the toner are weakly bonded with the paper and can be easily removed by taping, swabbing, or stamping with a polymer, while those embedded in the toner are retained, giving rise to a patterned electrode. Similarly, a fused deposition modeling (FDM) process using a 3D printer was used to define and transfer a kirigami pattern of AgNWs with no need for a hydrophobic donor substrate (Fig. 12d),[266] on which AgNWs are not easily deposited uniformly by the solution process. The AgNW pattern is determined by and embedded in the first layer of TPU. The 2nd–5th layers define the overall shape and a 3D notch that guides the folding of the kirigami pattern. The kirigami/origami-structured electrode could construct a perovskite solar module with a stretchability of up to 400%. In another report, poly(3,4-ethylenedioxythiophene):poly(styrenesulfonate) (PEDOT:PSS) was employed as the transfer template for AgNWs.[235] With a hot pressing process, the adhesion of AgNWs to PDMS is reduced, and the melting of D-sorbitol in PEDOT:PSS makes the AgNWs embedded in PEDOT:PSS, which allows for selective transfer of AgNWs. The conductive PEDOT:PSS can not only provide electrical contacts between AgNWs, but also increase adhesion and reduce roughness of AgNW electrodes.

4.1.3. Laser ablation. Laser ablation is a method of using a high-energy-density light beam to fragment MNWs or even evaporate them into a gas *via* light-induced heating. COMSOL simulations indicate that the MNWs at different positions of the network have significant temperature differences.[268] The NWs farther away from the substrate surface tend to reach higher peak temperature with more significant lateral thermal diffusion; that is, the ablation threshold decreases as the thickness of the film increases. Therefore, high uniformity of an MNW film is crucial for achieving uniform ablation patterns.

As an accurate, non-contact, mask-free tool, laser direct writing has been widely reported to achieve MNW patterns (Fig. 12f).[225,226,228,230,267,269] The disadvantage of this method is the damage to the substrate which exhibits distinct ablation traces. Fortunately, a nano/femtosecond laser can directly transform the MNWs into a plasma state without any thermal melting process, yielding well-defined patterns without damaging the substrate.[225,229,230] Fang *et al.* obtained an AgNW pattern with a linewidth as low as 20 μm by laser ablation and

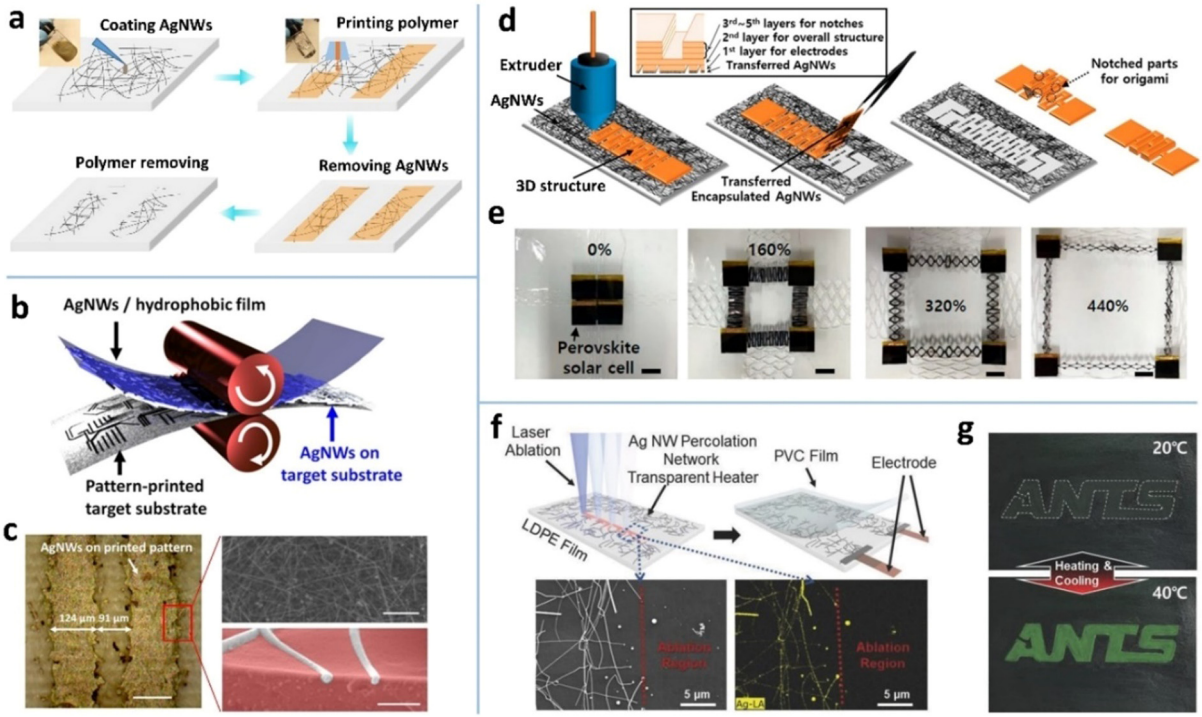

Fig. 12 (a) Patterning process of AgNWs with a printed PMMA template. Reproduced with permission.[218] Copyright 2019, Springer Nature. (b) Schematic of a toner-based transfer process for AgNWs. (c) A dry-transferred AgNW pattern and the corresponding SEM image. Reproduced with permission.[237] Copyright 2017, American Chemical Society. (d) Schematic of a 3D printer-based AgNW patterning method for constructing kirigami/origami electrodes. (e) The fabricated system fixed on a stretchable elastomer for a sufficient restoring force. Scale bars, 2 cm. Reproduced with permission.[266] Copyright 2019, American Chemical Society. (f) Schematic of laser patterning of AgNWs on a low density poly ethylene (LDPE) film for constructing a soft actuator. SEM and EDS images of the patterned AgNW network. (g) Color changes of the thermochromic ink layer. Reproduced with permission.[267] Copyright 2018, WILEY-VCH.

applied it as the bottom TE of a quantum dot light emitting diode (LED).[227] Tran *et al.* optimized the parameters of nanosecond pulsed laser ablation for patterning ultra-long CuNWs and reported the optimum conditions: 10 mJ cm^{-2} fluence, 40 kHz repetition rate, and 0.5 m s^{-1} scanning speed.[230] Liang *et al.* evaluated the ablation threshold of AgNWs and PET to realize high-precision patterning of AgNWs on a PET substrate by controlling the energy of femtosecond laser irradiation.[229] In short, laser ablation is a facile, mask-free patterning technique that is suitable for MNW networks of different shapes and sizes; however, it has the demerits of low productivity and high cost in equipment.

4.1.4. Plateau–Rayleigh instability method. Plateau and Rayleigh explained the phenomenon of a liquid jet breaking into small droplets when its length relative to the diameter was above a certain threshold in the 19th century. Later, Nichols and Mullins extended Rayleigh's theory to solids.[270] The origin of PRI is that a solid rod under elevated temperature tends to minimize its free surface area *via* surface energy. Since the PRI can cause the solid rod to undulate and break into an array of nanoparticles, it can yield various nanostructures from 1D metal nanomaterials, such as nanobeads, nanoparticle arrays, and micropatterns.

Selectively triggering PRI is the key to achieving patterned MNW networks, which can be realized *via* three strategies. The first strategy is the use of a pulsed laser with a small spot to trigger the PRI of MNW networks selectively.[221,222,224,271] Selectively coating the MNW network with thermally stable materials is the second strategy to control the PRI process.[272–275] Indium zinc oxide (IZO) was coated on AgNWs and then irradiated by deep ultraviolet (DUV) that induces the M–O–M condensation reaction of IZO.[223] The IZO capping greatly improves the thermal stability of AgNWs, while the non-irradiated IZO is removed to trigger the PRI of AgNWs at 250 °C, forming AgNW patterns with a resolution of about 100 μm. However, this method requires a relatively high heating temperature, which is unsuitable for flexible substrates.

To lower the triggering temperature of PRI, our group proposed two surface modification methods for AgNWs.[98,110,276] One is the modification with diphenyliodonium nitrate (DPIN), which can be self-assembled into nanoparticles on AgNWs after spin coating (Fig. 13a and b).[98] The DPIN NPs expedite the surface atom diffusion due to the gradient of chemical potential near the NPs

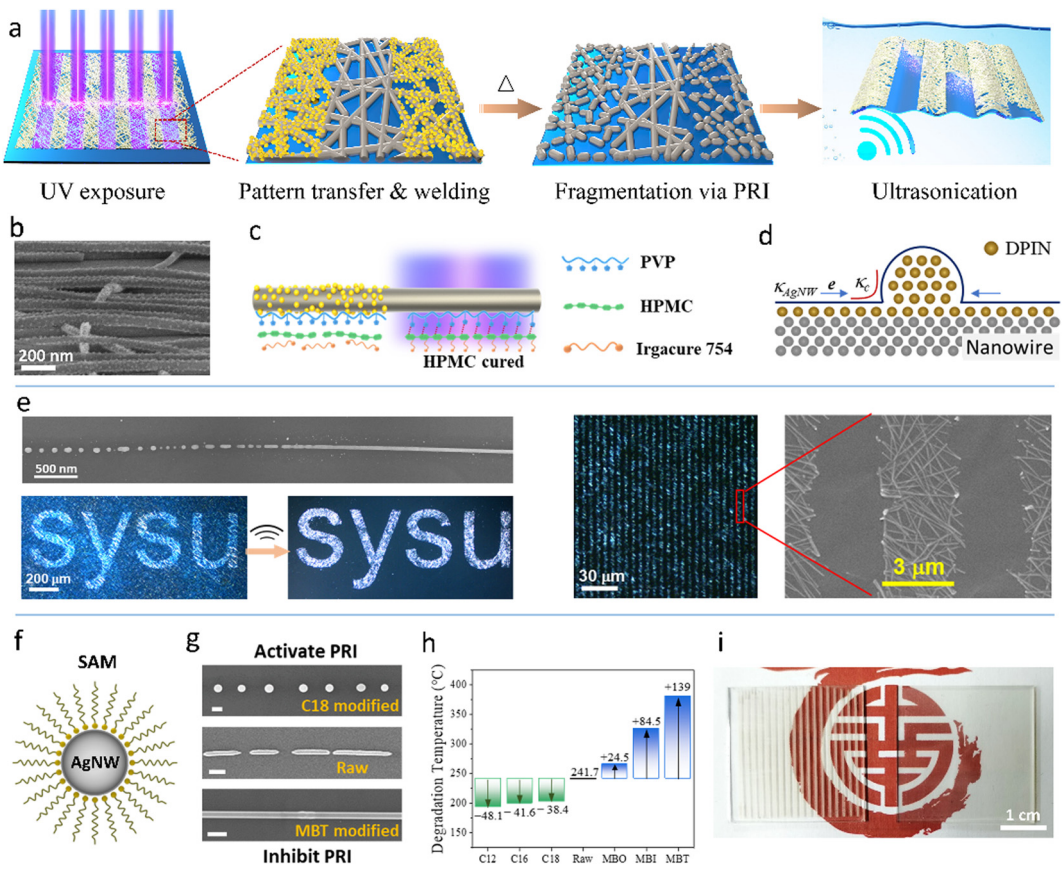

Fig. 13 (a) PRI patterning process of the DPIN-modified AgNWs. (b) SEM image of the DPIN-modified AgNWs. (c) Schematic of selective decomposition of DPIN and curing of HPMC along a single AgNW. (d) Mechanism of DPIN NP-induced fragmentation of AgNWs. (e) SEM and OM images of the PRI-patterned AgNWs. The upper-left image of (e) is reproduced with permission.[98] Copyright 2020, American Chemical Society. The other images of (a–e) are reproduced with permission.[110] Copyright 2022, Springer Nature. (f) Schematic of a SAM-modified AgNW. (g) SEM images of raw, C18-modified, MBT-modified AgNWs after 300 °C annealing for 5 min. (h) Degradation temperatures of raw AgNWs and SAM-modified AgNWs. (i) Photographs of the photolithography-patterned and PRI-patterned AgNW films. Reproduced with permission.[276] Copyright 2022, Springer Nature.

(Fig. 13d). Furthermore, DPIN modification can form a thin cladding of a molten salt-like compound on the AgNWs at an elevated temperature. The two effects decrease the degradation temperature (T_d) of the AgNW network by around 80 °C. Because of the hydroxy propyl methyl cellulose (HPMC)-enhanced plasmonic effect and the photo decomposable property of DPIN, nanowelding of AgNWs and pattern transfer can be simultaneously achieved by one-shot UV irradiation through a photomask (Fig. 13c). Then, low-temperature annealing (145 °C) can yield an AgNW pattern with a minimal size of 3 μm, which is the highest patterning resolution ever reported on AgNW microelectrodes. Moreover, the PRI-fragmented AgNWs in the unexposed region can be further removed by ultrasonication in water (Fig. 13e). The other is the modification with sulfhydryl compounds which form self-assembled monolayers (SAMs) on AgNWs *via* the Ag–S covalent bond (Fig. 13f).[276] It is found that the alkanethiol SAMs activate the PRI of AgNW while the mercaptobenzoheterocyclic (MBH) SAMs inhibit the process (Fig. 13g). The T_d of the AgNWs is successfully tuned in the range of 190–380 °C with different SAMs, with the raw AgNWs having a T_d of about 240 °C (Fig. 13h). With the selective modification of the SAMs using a PDMS stamp, the AgNW network could be patterned by selective PRI-induced fragmentation.

The PRI process leads to selective fragmentation of an MNW network to disconnect the percolation way for electrons. Different from the traditional top-down and bottom-up strategies, the PRI patterning retains the traces of MNWs in the insulated area.[98,110] If the PRI process does not reach the mature state and just fragments the AgNW network at junctions *via* the Gibbs–Thomson effect,[276] the remaining traces can effectively eliminate the optical difference between the conductive and insulative regions due to the well-matched refractive indices and scattering coefficients. The difference in the transmittance is less than 10%, which makes the patterning invisible to the naked eyes (Fig. 13i).[221,222,276] The invisible MNW electrode is of particular importance for display devices in terms of image quality.

4.2. Bottom-up strategy

The top-down patterning methods involve either wet or dry processes for selectively removing MNWs, which not only require expensive equipments and/or complex technical process, but also waste some MNWs. Therefore, various bottom-up patterning methods have been developed to deposit MNWs into patterns on substrates directly. These methods can be classified into three categories: printing methods, wetting–dewetting self-assembly, and template-assisted patterning.

4.2.1. Printing techniques

Inkjet printing. IJP is a maskless method that deposits ink droplets on a substrate to form a predefined pattern. There are two kinds of IJP: intermittent IJP and continuous inkjet (CIJ) printing.[277] Intermittent IJP, also known as "drop-on-demand" IJP, directly ejects droplets to the substrate as needed, where the droplets are thermally driven or piezoelectrically driven. In CIJ printing, a continuous flow is expelled from the nozzle and then broken up into intermittent droplets through high frequency vibration,[278] which are controlled by the deflection electrode to deposit into a specific position on the substrate. The patterning resolution is highly dependent on ink properties and the size of the printing nozzle. To achieve good stability, printability, and thus ultra-fine patterns, ink components (such as concentration, solvents, and other organic additives) must be carefully adjusted to optimize ink properties such as viscosity and surface tension.[231,232,279–281] Coleman *et al.* added diethylene glycol to isopropanol dispersion to increase the viscosity of the AgNW ink, which produced reasonably uniform AgNW patterns with linewidths of 1–10 mm and a conductivity of 10^5 S m^{-1}.[231] Chen *et al.* replaced isopropanol with deionized (DI) water to provide a stable AgNW suspension, printing an AgNW electrode pattern with a linewidth of about 50 μm and an edge roughness of 5 μm on PET. Printing resolution can be further improved by reducing nozzle size. However, the nozzle is easily clogged when the material size significantly exceeds the empirically determined printable size a/50 (a is the nozzle diameter).[231,232,282] Therefore, ultrasound is used to induce fragmentation of NWs to shorten their lengths, but shorter MNWs lead to lower conductivity and stretchability of the electrode. It is reported that the limitation of the ruleofthumb printable size (a/50) can be overcome using a direct printing method, in which a glass micropipette is in direct contact with the substrate through the ink meniscus (Fig. 14a). This method prints AgNWs of up to 40 μm in length into a pattern of about 270 μm in linewidth with well-defined and uniform features.[283] As the traditional IJP technology faces the issue of nozzle clogging and difficulty in producing high-resolution patterns, new IJP methods, such as aerosol jet printing (AJP) and EHD printing, have been developed.

Aerosol jet printing. AJP atomizes the functional ink to form aerosol droplets with diameters of 1–5 μm by pneumatic or ultrasonic processes and delivers the droplets to the substrate through a carrier gas (Fig. 14b).[143,284] During the transportation of the aerosol, the sheath gas forms an outer layer around the aerosol stream, which prevents the aerosol particles from contacting the inner wall of the nozzle, thereby avoiding the issue of nozzle clogging. This process also shows greater ink compatibility in viscosity (0.7–2500 cP) than IJP, which is usually limited to a narrow viscosity range of 10–40 cP.[285] In addition, the focusing effect of the sheath gas provides AJP with a high printing resolution of about 10 μm under appropriate conditions.[286] The printing quality of AJP is closely related to the process parameters, including atomization frequency, gas flow rate, nozzle size, working distance, *etc.*[143,287,288] It is reported that the linewidth can be narrowed by increasing the stage speed and the focusing ratio which is the ratio of sheath gas velocity to carrier gas velocity.[287] Tu *et al.* obtained AgNW electrodes with a linewidth of 50.9 μm and an R_S of 57.7 Ω sq^{-1} under an optimized condition (printing cycle is 1, printing speed is 0.4 mm s^{-1}, nozzle size is 200 μm).[143] AJP takes advantage of high-pressure air jets to reduce the limit on ink viscosity and aerodynamic focusing to obtain high-resolution patterns. However, some of the atomized droplets jetted by the high-pressure airflow will deposit nearby the printed patterns, resulting in rough edges of the patterns.[289]

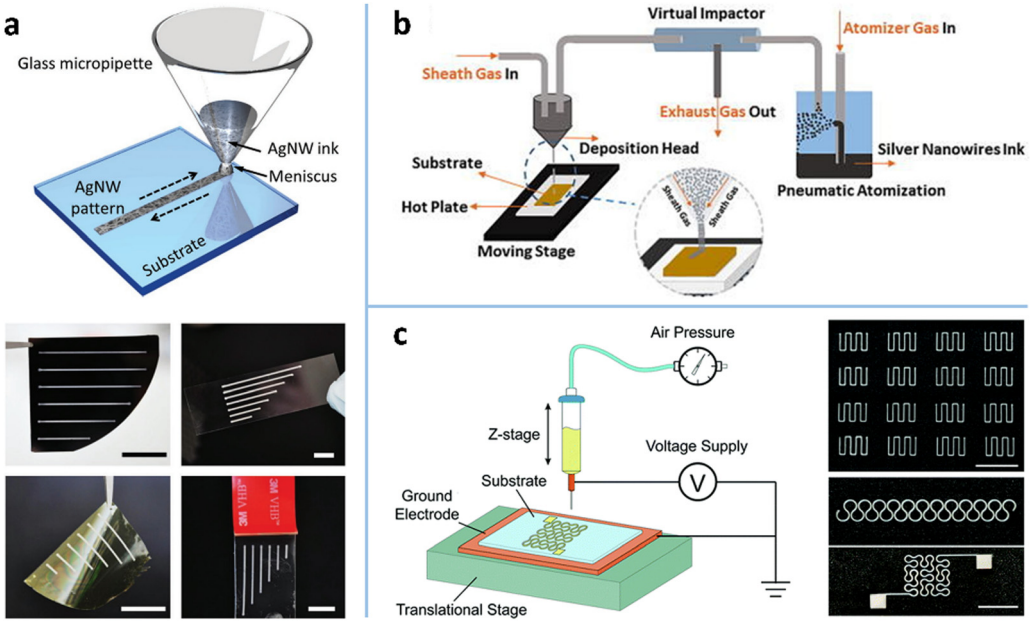

Fig. 14 (a) Schematic of IJP for AgNWs and the printed AgNW patterns on a silicon wafer, glass slide, PI thin film, and VHB tape. Scale bars: 2 cm. Reproduced with permission.[283] Copyright 2017, WILEY-VCH. (b) Schematic of an AJP system. Reproduced with permission.[143] Copyright 2018, AIP Publishing. (c) Schematic of an EHD printing system and the printed AgNW patterns. Scale bar: 1 cm. Reproduced with permission.[139] Copyright 2018, RSC Pub.

Electrohydrodynamic printing. The EHD printing system consists of a pneumatic element, a power source, and a translational stage (Fig. 14c).[139] The ink is delivered to the nozzle by a pneumatic press to form a meniscus which is deformed into a cone by the electrostatic repulsion of the charges induced by the electric field between the nozzle and the substrate. As the electric field stress overcomes the surface tension of the ink, a jet of droplets, with diameters 2 to 5 orders of magnitude smaller than the nozzle diameter, will be ejected from the cone.[290] There are different injection modes under different electric field strength and flow rates, including dripping, cone jet, pulsating jet, and complex jet.[291,292] In the "cone jet" mode, the flow rate and the electric field are properly matched, and a continuous ink stream will be ejected from the nozzle. With an excessive increase in electric field strength, "complex jet" modes (such as tilted jetting and multi-jetting) will be triggered and cannot be used for EHD printing. The patterning resolution can be controlled by carefully adjusting ink composition and printing parameters. Li *et al.* increased the printing speed from 1 to 30 mm s^{-1}, reducing the printing linewidth from 463 to 210 μm. The best lines with a uniform shape and sharp edges were achieved at a speed of 20 mm s^{-1}.[141] Cui *et al.* adjusted AgNW concentration, ink viscosity, printing speed, and stand-off distance, to obtain a minimum linewidth of about 45 μm.[139] An EHD-printed, aligned AgNW microgrid shows an ultrahigh T of 99.1% at an R_S of 91 Ω sq^{-1}.[165] EHD printing has shown the potential for large-scale manufacture of flexible electronic devices, such as dry electrocardiogram electrodes and electronic skins.[139,293,294] It can print different materials into large-scale repetitive and complex patterns with high resolution on various substrates, and has evolved from 2D to 3D micro/nanoscale additive manufacturing technology.[291,293]

Screen printing. Screen printing uses a squeegee to squeeze ink through a patterned screen mask to achieve large-area patterns. It is suitable for almost all types of substrates, such as textiles, PET, glass, paper, polyimide (PI), *etc.*[295–299] The printing process can be implemented on both flat surfaces and curved surfaces (Fig. 15a and b) so that R2R printing modes can be developed to improve output efficiency.[300–302] The patterning resolution of screen printing largely depends on the graph structures of screen masks and the formulation of printing inks.[303,304] High-viscosity ink can easily cause clogging, while low-viscosity ink induces leakage.[305] Screen printing requires the ink to have the thixotropic shear thinning property: the ink viscosity decreases with the shear rate to allow ink to pass through the mesh without congestion,[234,306] and the viscosity quickly returns to its initial high value to retain the ink on the mesh (Fig. 15c),[295,303,305] which improves printing precision. A shear-thinning ink is reported to consist of Cu@Ni rose-stem nanowires (RSNWs), carboxymethyl cellulose (CMC), PVP (M_W = 10 000), and DI water.[297] The ink viscosity is 102.2 Pa s and is reduced by about 1 Pa s as the shear rate increases to 10^3 s^{-1} (Fig. 15c). The viscosity value recovers the initial value within 100 s, providing enough time to deposit the ink onto the substrate with good printing quality. Another shear-thinning ink is the mixture of AgNWs, HPMC, and Zonyl FC-300, in which HPMC is used to adjust the rheological behavior of AgNW-ink (Fig. 15d).[233,295] The ink yields neat and smooth lines with a high conductivity of 46 700 S cm^{-1} and a minimum resolution of 50 μm.[295] Besides printing single functional material, screen printing can also print composite materials.[306,307] Li *et al.* developed a thixotropic ternary ink that combines AgNWs with GO nanosheets and hydrated ruthenium oxide nanoparticles

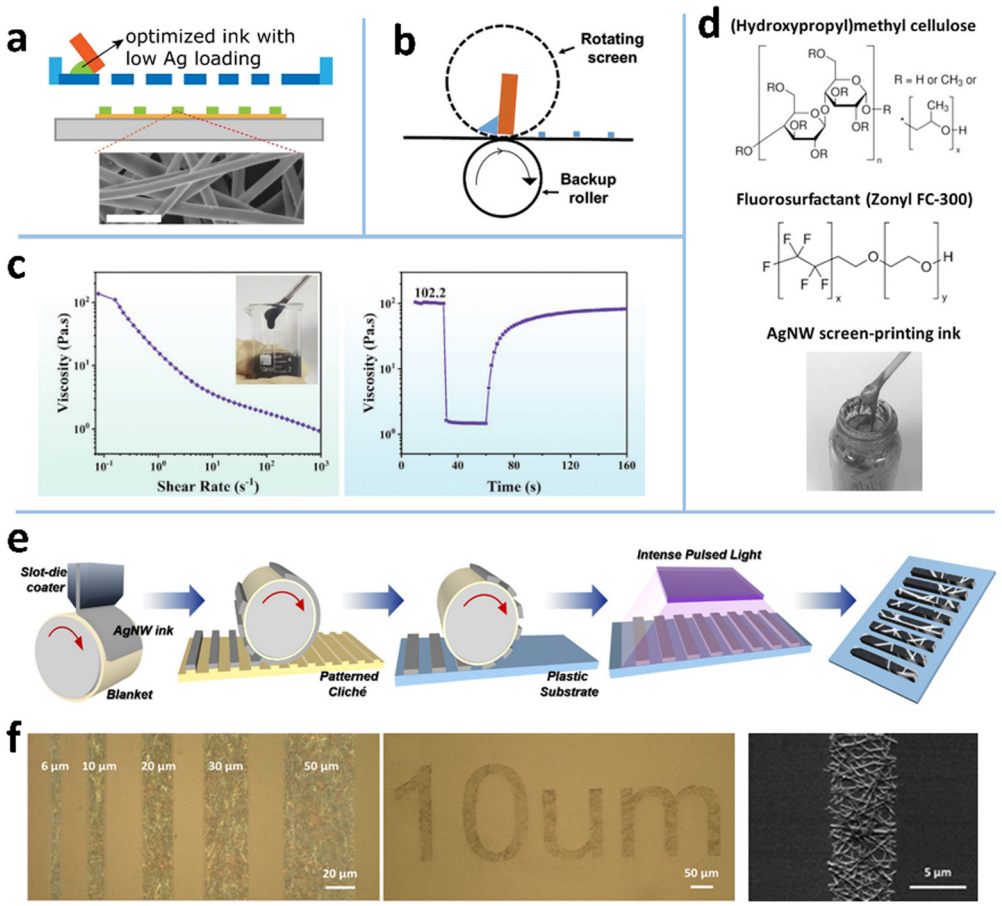

Fig. 15 (a) Schematic of flat screen printing. Reproduced with permission.[308] Copyright 2019, Springer Nature. (b) Schematic of rotary screen printing. Reproduced with permission.[309] Copyright 2019, WILEY-VCH. (c) Rheological property and thixotropic behavior of the Cu@Ni RSNW ink. Reproduced with permission.[297] Copyright 2020, WILEY-VCH. (d) Molecular structures of HPMC and Zonyl FC-300, and the prepared AgNW ink. Reproduced with permission.[295] Copyright 2016, WILEY-VCH. (e) Process of a reverse offset printing technique for patterning AgNWs. (f) Printed AgNW patterns on plastic substrates. Reproduced with permission.[239] Copyright 2019, American Chemical Society.

without inert additives. A uniform pattern with a minimum feature size of ~50 μm is directly achieved by screen printing without any hash post-processing.[307] In addition to adjusting the ink formulation, the properties of the pattern can also be improved by optimizing the printing parameters such as printing speed, extrusion force, the gap between the mesh and the substrate, and the number of printing cycles.[308]

Transfer printing. Transfer printing is controlled by the adhesion difference between two interfaces in a stamp/ink/substrate structure. Retrieval of ink occurs under stronger adhesion between the stamp and ink than that between the ink and substrate, while printing of ink occurs under weaker stamp/ink adhesion. Common methods of adhesion modulation for MNW patterning include surface chemical modification and polymer glue.[310] For elastomer stamps with significant viscoelastic properties, the adhesion at the stamp interface can also be modulated by the peeling speed. A higher peeling speed facilitates ink retrieval, while a lower speed enables ink printing onto a receiving substrate.[311]

One advantage of transfer printing is that it separates the manufacturing substrate from the target substrate, thus overcoming the incompatibility issues of conventional manufacturing techniques for flexible polymer substrates such as high temperature and chemical etching. Another advantage is that transfer printing is compatible with the R2R process in different patterning ways, including additive transfer, subtractive transfer (see Section 4.1.2), and pattern transfer.[311]

The additive transfer is a process wherein the ink is first deposited on the structural stamp and then brought into contact with and delivered onto the target substrate through the stamp.[312,313] In an early report, AgNWs were first deposited on the anodized aluminum oxide (AAO) membrane through vacuum filtration and then transferred onto the embossed PDMS stamp.[312] The PDMS stamp was also successfully inked with AgNWs *via* spray coating.[313] For fully transferring the AgNWs on the stamp, the receiving glass substrate was modified with 3-aminopropyltriethoxysilane which has strong σ-donating functional groups (NH_2) to produce adhesion to AgNWs. As a commonly used material for stamps, PDMS needs hydrophilic treatment and suffers from temporary or permanent deformation caused by absorption of organic solvents. As a substitute, agarose has been proposed to construct stamps.[236] Although the

mechanical strength of agarose needs to be improved, its hydrogel properties are beneficial for transfer. An AgNW pattern of 200 × 200 μm^2 has been directly transferred onto the TiO_2/Ag/PES substrate through an agarose stamp, which constructs a sandwich structure of TiO_2 resistive random-access memory.

Pattern transfer is the approach that combines patterning of MNWs on a donor substrate with further transferring of the pattern onto a receiving substrate.[241–244,314] The key to transfer is the adhesion difference between the two interfaces, so a donor substrate with low surface energy is usually required. However, it is difficult to deposit uniform MNW networks on such substrates by the solution process. To this end, MNWs were generally deposited on porous AAO or polytetrafluoroethylene (PTFE) with low surface energy by vacuum filtration. The MNWs were then transferred onto a secondary substrate (mainly PDMS) and finally to the target substrate.[315,316] Another attractive solution is that the substrate coated with MNWs was selectively modified to lower the surface energy by making use of the porosity of the AgNW networks.[99,240] The AgNW patterns on the modified PDMS have been successfully transferred onto various substrates with the assistance of UV-cured epoxy resin.

Two other promising techniques for pattern transfer are gravure printing and reverse offset printing, both of which use intaglio to generate nanomaterial patterns and are compatible with the roll-to-roll process for large-area and high-throughput manufacturing.[140,239,317–319] The gravure printing consists of two steps: filling ink onto the intaglio pattern and transferring the ink to the target substrate. The shape and fidelity of the printed pattern are determined by the rheological behavior of the ink defined by the capillary number (Ca = $\mu v/\sigma$).[319] The best printing quality can be achieved by adjusting the printing speed and ink parameters (viscosity and surface tension) to make Ca ≈ 1. A water-based AgNW ink, consisting of poly(ethylene oxide), ethanol, and water, has been developed for gravure printing to generate uniform, sharp-edged lines with a resolution of 50 μm on PET.[140] In reverse offset printing (Fig. 15e), the ink is first coated onto a PDMS-based blanket. The semi-dried ink on the blanket is selectively taken away by an embossed cliché. The adhesion of the ink to the blanket needs to exceed the shear strength of the edge to break the ink film and form a pattern on the blanket. The final step is the set process, in which the created patterns on the blanket are transferred onto a receiving substrate. AgNW patterns with a minimum linewidth of 6 μm have been achieved by carefully adjusting the ink composition and printing parameters (Fig. 15f).[239]

4.2.2. Wetting–dewetting self-assembly. The wetting–dewetting method uses a surface with high wettability contrast to confine the wetting and spreading of ink for patterning the ink-dispersed MNWs.[320,321] A liquid film on a hydrophobic surface can spontaneously dewet as its thickness is less than the critical thickness for dewetting.[322] The ruptured liquid is driven to the hydrophilic surface by the uncompensated Young's forces, resulting in a specific pattern of MNWs after solvent drying. To achieve a wettability-heterogeneous surface, hydrophobic fluorocarbon materials (Cytop, WP-100) and PDMS have been patterned by photolithography or irradiation of vacuum-ultraviolet or UV/O_3.[90,99,151] By using photolithography, our group constructed a patterned hydrophobic Cytop on a UV/O_3-treated hydrophilic Si wafer,[151] which self-assembles AgNWs into microchannels of width as low as 8 μm with rod coating (Fig. 16a and b). The narrower width of the microchannel results in a higher alignment degree of the NWs, which leads to less R_S (Fig. 16c). Compared to the MNW network patterned by top-down methods, the aligned and patterned MNW network is more conducive to maintaining percolative paths for electrons at narrow widths (Fig. 16d).

The pattern morphology of MNWs is closely related to the coating method, wettability contrast, and topographic structure. Rod coating with high speed (*e.g.*, >3.2 mm s^{-1}) can yield AgNW patterning with narrow linewidths; however, there are many residual AgNWs on the narrow spacings due to the meniscus pinning and on the huge open hydrophobic regions due to fracture of the liquid film.[90] In addition, the coffee-ring effect in the large-area hydrophilic region results in a lower R_S. Reducing the rod-coating speed (*e.g.*, <0.4 mm s^{-1}) makes the meniscus follow the rod without pinning, which improves the electrode conductivity and patterning resolution down to 20 μm in spacing.[324] Nevertheless, there are still residual MNWs on the hydrophobic region. Our group achieved a high-resolution, uniform AgNW pattern without residual AgNWs in the hydrophobic region by spin coating the AgNW ink in a wettability-patterned PDMS (Fig. 16e).[99] Large centrifugal force at high rotation per minute can overcome the ink hysteresis on hydrophobic regions and the pinning effect on patterned hydrophilic regions to remove excess ink and achieve uniform deposition. In addition, wettability contrast plays a vital role in the morphologies of self-assembled MNWs. In the patterned region, high surface energy (*e.g.*, >72 mJ m^{-2}) is required to obtain positive spreading coefficients for the ethanol-dispersed AgNW ink and thus achieve high-fidelity patterning.[99] The area fraction of AgNWs in the hydrophilic region is found to be linearly proportional to $\gamma_s - \gamma_l$ (γ_s and γ_l are the surface energies of the hydrophilic region and ink) (Fig. 16f). $\gamma_s - \gamma_l$ of 49 mJ m^{-2} is required to achieve 100% area fraction, that is, full-coverage and high-resolution patterning. It is also found that the UV/O_3-patterned PDMS has nanowell-like topography. This structure induces strong pinning of the ink to establish a well-defined, smooth, and continuous percolative path along the patterning boundary (Fig. 16e and g).

Instead of dewetting self-assembly, microflow velocity-field-induced patterning of MNWs has been recently reported on a patterned substrate with a less wettability contrast through bar coating (Fig. 16h).[323] A cross-border overlaying of the ink was formed on the substrate, where the ink flow decelerates at the surface with low surface energy and accelerates at the surface with high surface energy. Therefore, the AgNWs in the ink can be layer-by-layer assembled on the hydrophobic region (γ_s^-), with the 1st layer of AgNWs aligned along the coating direction, and the 2nd and 3rd layer of perpendicularly aligned AgNWs driven by Rayleigh–Bénard convection and Marangoni convection respectively, giving rise to a cross-linked AgNW network (Fig. 16i).

4.2.3. Template-assisted patterning. The template assisted method is based on the spatial limitation of a template to form

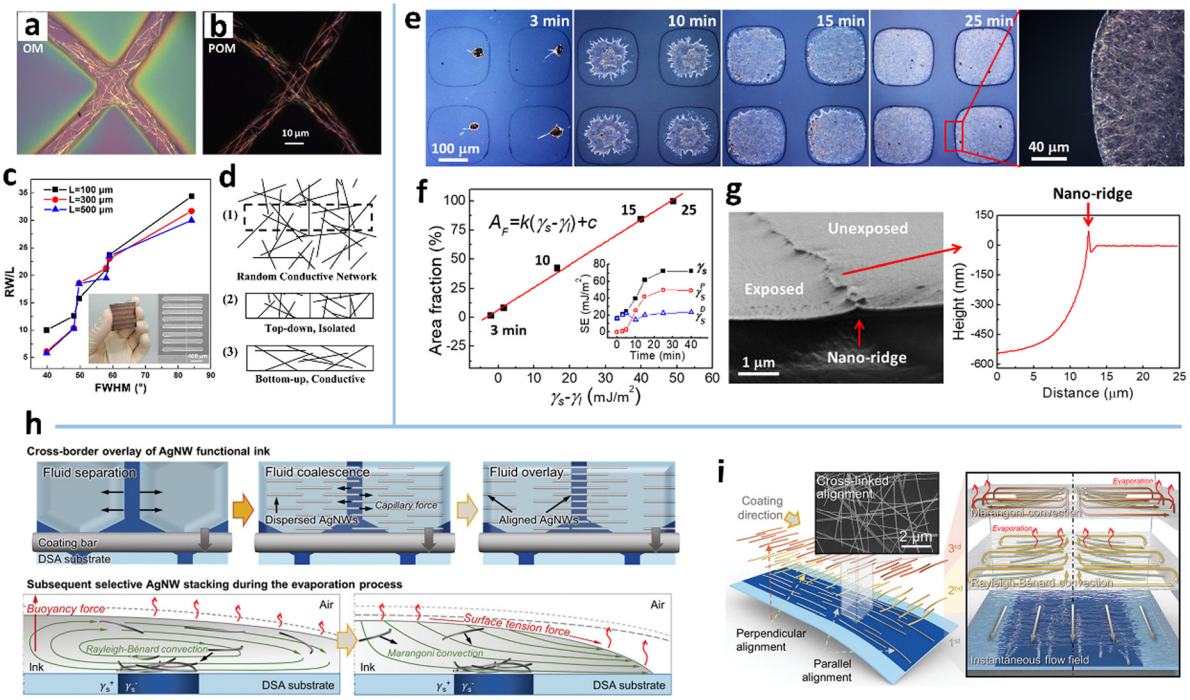

Fig. 16 (a) OM and (b) polarizing OM images of patterned AgNWs in super-hydrophilic microchannels. (c) Variation in *RW*/*L versus* FWHM of the aligned AgNWs in the microchannels. *W* is the channel width and *L* is the channel length between electrodes. The inset is an electrode sample. (d) Schematic of the NW networks patterned by top-down and bottom-up methods, respectively. Reproduced with permission.[151] Copyright 2015, American Chemical Society. (e) The effect of UV treatment time on the area fraction of AgNWs in the hydrophilic region. (f) Area fraction of AgNWs as a function of $\gamma_s - \gamma_l$; the inset is the surface energies (SE) for different UV treatment times. (g) SEM image of the UV-patterned PDMS and the surface scanning profile of the PDMS. Reproduced with permission.[99] Copyright 2016, RSC Pub. (h) Selection deposition of AgNWs on the hydrophobic (γ_s^-) region through Rayleigh-Bénard convection and Marangoni convection. (i) Schematic and SEM image of the multi-alignment during the coating and self-assembly process. Reproduced with permission.[323] Copyright 2022, WILEY-VCH.

specific deposition patterns of MNWs. A commonly used template is the PDMS-based embossing stamp which is usually replicated from a mold. The stamp can directly imprint the MNW ink on a substrate to achieve patterns (Fig. 17a), or it is in conformal contact with a bare substrate to form microchannels and then induce penetration of the MNW ink *via* capillary action to produce patterns.[108,325] The solvent can be drained from the microchannels by either a natural drying process or spin coating,[325] which leaves templated MNWs. The height and width of the microchannels have important effects on the patterning process. Greater height has a stronger capillary effect to induce a faster filling of the MNW ink; however, for AgNW ink, NW aggregation along the microchannel boundary occurs as the height increases to 25 μm and some aggregation occurs in the microchannels as the width decreases to 20 μm.[326] For AuNWs with a diameter of 1.6 nm and an aspect ratio >1000, an AuNW pattern with a thickness of 15 nm and a width of 250 nm has been successfully fabricated. One good feature of meshed structures is their ability to enhance the optoelectrical performance of MNW networks. The AuNW mesh shows an R_S of 29 Ω sq^{-1} and a *T* of 68%, and is superior to other AuNW-based TEs.[327]

A combination of hollow-out masks and vacuum filtration is another strategy for MNW patterning. Vacuum filtration uses negative pressure to accelerate the filtration of the MNW ink through a hollow-out mask to achieve an MNW pattern. The deposited patterns on filter membranes are generally transferred to target substrates for further use.[330] For this reason, the hydrophobic filter membranes made of polyvinylidene fluoride (PVDF) and PTFE are frequently used to allow pattern transfer.[331,332] The AAO film has also been used as the filter membrane, on which the AgNW pattern can be transferred onto the PDMS film with the assistance of DI water or after modifying AAO with octadecyltrichlorosilane.[243,316] Also, uncured or semi-cured PDMS films are used to transfer and carry AgNW patterns from the filter membranes. The AgNWs are embedded in PDMS to form SEs with stretchability up to 100% (Fig. 17c–f).[329]

In this method, the mask is paramount to patterning quality of MNWs. Removable hollow-out masks are the most used. However, there are some disadvantages of hollow-out masks. First, the patterning resolution is usually poor for the following reasons: (1) it is difficult to fabricate and handle a thin mask with a high-resolution pattern. (2) Lateral penetration between the mask and the substrate and NW crossover between the open area and the mask surface leads to the rough edges of the pattern. Um *et al.* patterned an ultrathin PI film by photolithography and RIE processes to obtain a high-resolution mask.[316] The ultrathin PI masks can conformally adhere to the AAO filtration membrane and be intactly removed, producing clear AgNW patterns with a minimal linewidth of about 3.5 μm

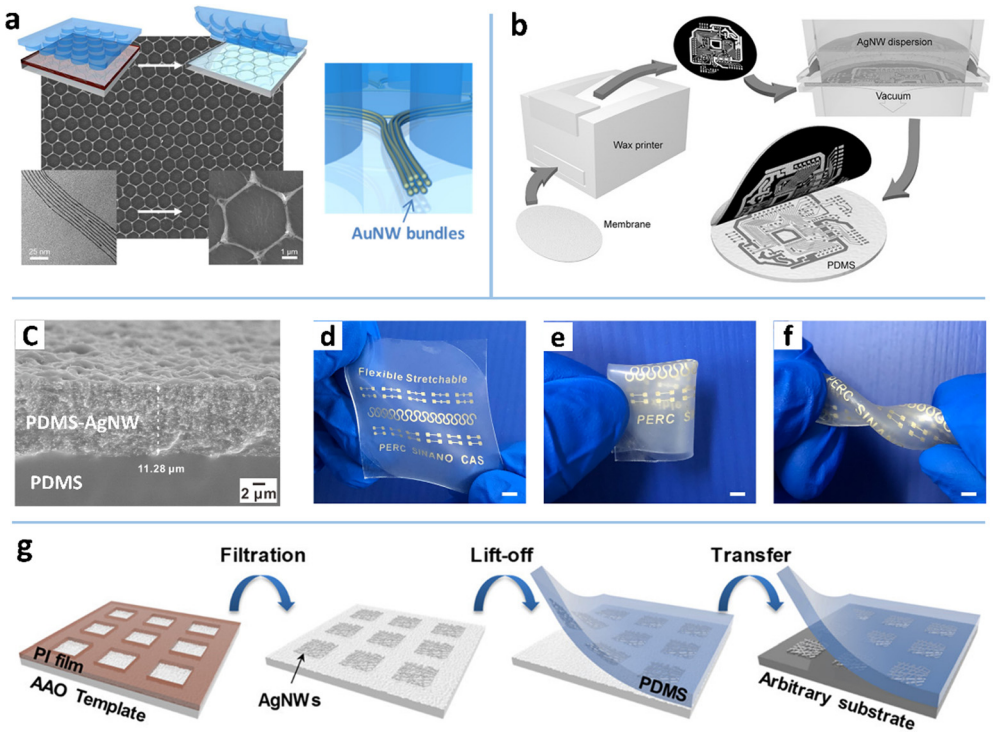

Fig. 17 (a) Schematic of the nanoimprinting and bundling process, and SEM and TEM images of the patterned AuNWs. Reproduced with permission.[108] Copyright 2016, American Chemical Society. (b) Process of a wax printer and vacuum filtration-based patterning method for AgNWs. Reproduced with permission.[328] Copyright 2015, WILEY-VCH. (c–f) SEM image and photographs of the stretchable, embedded AgNW patterns that are fabricated by a vacuum filtration and transfer process. Reproduced with permission.[329] Copyright 2022, Springer Nature. (g) Schematic of the AgNW patterning process through vacuum filtration and transfer printing. Reproduced with permission.[316] Copyright 2020, American Chemical Society.

(Fig. 17g). Second, the hollow-out masks are not suitable for preparing complex patterns with closed-loop areas, because the mask is difficult to be peeled off from the filtration film in one step. To address the above issues, two kinds of masks have been developed. One is the 3D PDMS mask that allows the AgNW ink to flow through the channels inside it, achieving a closed-loop pattern with sharp edges.[333] The limitation of this method is the difficulty in fabrication of high-resolution 3D masks. The other one is the blocking mask that is directly printed on porous filters. In early reports, a black ink was patterned on a paper through screen printing to block the paper selectively. After vacuum filtration, a paper-based AgNW circuit was achieved with a high conductivity of 60 781 S cm^{-1} and a minimal linewidth of 250 μm.[334] Another facile method resorts to a wax mask that is printed on the hydrophilic porous PVDF film by a desktop wax printer (Fig. 17b).[328] The AgNW ink is spontaneously filtered through the masked PVDF membrane to form AgNW patterns with a minimum patterning size of approximately 100 μm, which is limited by the resolution of the wax printer. Similarly, through screen printing, liquid PDMS is also patterned on filter membranes (Teflon and PTFE). A hydrophobic mask can reduce the AgNWs remaining outside the defined pattern due to the dewetting effect, which yields a pattern with sharp edges and a linewidth down to 50 μm.[315,328]

In short, the patterning technology for MNWs has made considerable progress since 2015. As shown in Table 2, the highest patterning resolutions of 250 nm for AuNWs, 3 μm for AgNWs, and 13.5 μm for CuNWs have been achieved. Among the top-down patterning strategies, photolithography can fabricate AuNW patterns with the highest resolution of 2.5 μm; some etching-free methods based on adhesion difference have been developed with patterning resolutions down to 10 μm; the novel PRI-based patterning method, different from the traditional top-down and bottom-up strategies, gives rise to the highest resolution of 3 μm in both linewidth and spacing for AgNW microelectrodes. As for the bottom-up strategies, the printing resolutions of IJP, AJP, and screen printing have been improved to 50 μm. The template-assisted patterning methods such as vacuum filtration have reduced the patterning linewidth to <10 μm. They have the merits of material saving and easy operation but are impractical for large-area manufacture. It is noted that the reverse offset printing shows high resolution and good manufacturability.

5. Applications

MNWs assembled into specific morphologies have shown great potential in diverse fields, including electronics, photonics, optoelectronics, catalysis, *etc.*[43,44,343] Since there are too many novel devices and application scenarios for this review to cover, we focus on a few distinguished applications which are based on TEs and SEs. The properties of TEs and SEs fabricated by the methods of self-assembly, alignment, and patterning are

Table 2 Summary of the current patterning methods for MNWs in terms of substrates, line width (L_W), and spacing (S)

Technical route	Methods	Materials	Substrates	L_W (μm)	S (μm)	Ref.
Top-down	Photolithography	AgNWs	Glass, PDMS	20	40	206
	Photolithography and transfer	AgNWs	PDMS and PUU[a]	100	100	335
	Shear alignment and photolithography	AuNWs	Si wafer	2.5	—	336
	Photolithography	AgNWs	Glass	180	110	337
	Photolithography	AgNWs and RuO_2	PET	10	—	338
	Atmospheric cold plasma-jet	AgNWs	PET	50	—	339
	Dry-film photolithography	AgNWs	PET	10	—	212,213
	Microcontact printing and etching	AgNWs	Si, PET	25	25	265
	Selective adhesion and transfer	AgNWs	PMMA, PET, acrylic substrates	100	—	106
	IJP and selective removal	AgNWs	PET	60	80	218
	IJP and adhesion manipulation	AgNWs and PMMA	Glass, PET, PDMS	10	10	238
	IJP and selective removal	AgNWs and PEDOT:PSS	Glass, PEN	30	—	235
	Selective adhesion and ultrasonication	AgNWs and TEH	PDMS	30	10	37
	IPL and selective removal	AgNWs/CuNWs	PET, cPI, PEN, PC	13.5	—	219,220
	Selective DUV exposure and thermal annealing	AgNWs and IZO	Glass, PI	100	100	223
	PRI patterning	AgNWs and DPIN	Glass, PDMS	3	3	110
	Laser scanning and transfer	CuNWs and PUA	Adhesive substrate	100	—	259
	Laser scribing and heat press lamination	AgNWs	Textile	135	—	340
	Laser ablation	AgNWs/CuNWs	Glass, silicon, PDMS, PET	20	—	227,230,341
	Laser ablation	AgNWs and PEDOT:PSS	PI	100	100	228
Bottom-up	AJP	AgNWs	Glass	50.9	—	143
	Gravure printing	AgNWs	PET	50	100	140
	IJP	AgNWs	Si, glass, PI, VHB tape, PDMS, PET, photo paper	240–270	—	232,283
	IJP	AgNWs	PET	50	—	83
	Screen printing	AgNWs	PET, PUA, glass, PDMS	50	50	233,295,342
	Reverse offset printing	AgNWs	PC,[b] PET	6	30	239
	Wetting–dewetting	AgNWs	Silicon	8	—	151
	Wetting–dewetting and transfer	AgNWs and PEDOT:PSS	Glass, PDMS	150	—	241
	Wetting–dewetting and transfer	AgNWs	PDMS, PVA, paper, PET	20	—	99,244
	Template assisted method	AuNWs	Glass, PET	0.25	5	327
	Template assisted method	AgNWs	Glass, PI	10	50	325
	2D ice-templating approach	AgNWs	PET	—	100	36
	Vacuum filtration and transfer	AgNWs	PDMS, PET	100	100	328,333
	Screen printing and vacuum filtration	AgNWs	PTFE	50	50	315
	Vacuum filtration and transfer	AgNWs	Si, glass, PET	3.5	—	316

[a] PUU: polyurethane urea. [b] PC: polycarbonate.

investigated, compared, and discussed, to provide guidance for fabricating high-performance devices.

5.1. Flexible transparent electrodes and applications

5.1.1. Optoelectrical characterization. The high conductivity, porous structure, and low extinction coefficient of MNW networks make them suitable for flexible TE applications. The optoelectrical performance of a TE can be mainly characterized by two trade-off parameters: transmittance and sheet resistance. The trade-off relationship is quantified by figure of merit (FoM) which can be estimated by many models, such as the Haacke model.[344] For nanostructure-based TEs, the transmittance can be given by[345]

$$T = \left(1 + \frac{Z_0}{2}\sigma_{op}t\right)^{-2} \quad (5)$$

where Z_0 is the impedance of free space (377 Ω), σ_{op} is the optical conductivity, and t is the film thickness. Combining eqn (5) with the definition of sheet resistance ($R_S = 1/(\sigma_{dc,B}t)$, $\sigma_{dc,B}$ is the DC conductivity for the bulk film, t is the thickness of the MNW network), a relationship of T and R_S can be obtained for quantifying FoM:[346]

$$T = \left(1 + \frac{Z_0}{2R_S}\frac{\sigma_{op}}{\sigma_{dc,B}}\right)^{-2} \quad (6)$$

where $\sigma_{dc,B}/\sigma_{op}$ is the FoM. High values of FoM denote high T and low R_S. This model can provide a good fitting to T and R_S of relatively thick (bulk-like) MNW films, but severely deviate the data from the thin (percolative) MNW networks. This is because the DC conductivity (σ_{dc}) of a thin MNW network is no longer a thickness-independent parameter ($\sigma_{dc,B}$) but is a power function of thickness: $\sigma_{dc} \propto (t - t_c)^n$, where n is the percolation exponent. Based on this, Coleman *et al.* developed a new function relation between T and R_S for percolative MNW networks:[347]

$$T = \left[1 + \frac{1}{\Pi}\left(\frac{Z_0}{R_S}\right)^{1/(n+1)}\right]^{-2} \quad (7)$$

$$\Pi = 2\left[\frac{\sigma_{DC,B}/\sigma_{Op}}{(Z_0 t_{min}\sigma_{Op})^n}\right]^{1/(n+1)} \quad (8)$$

where Π is the percolative FoM. High Π and low n denote a TE having high T coupled with low R_S. The percolative model provides an excellent fitting to the data (T, R_S) for thin MNW networks in the percolative regime.

Haze is another critical parameter for application in displays, touch panels, lighting, and solar cells. It refers to the degree of deviation of light when passing through MNW networks:[348]

$$H(\lambda) = \frac{T_{diffuse}(\lambda)}{T_{total}(\lambda)} \quad (9)$$

where $T_{diffuse}$ is the forward scattered light at angles larger than 2.5° and T_{total} is the total amount of the transmitted light. As a TE component, $H < 1\%$ is typically required for displays and touch panels while $H > 10\%$ coupled with $T > 85\%$ is preferred to achieve high light absorption for solar cells.[349] The haze of an MNW network is dependent on the scattering efficiency (Q_{ext}) and area coverage (A_C) of NWs:[350]

$$H = \frac{F_{12}F_{23}\frac{C^{90}_{2.5}}{C_{ext}}(1 - e^{-A_c Q_{ext}})}{F_{12}F_{23}F_{31}e^{-A_c Q_{ext}} + F_{12}F_{23}\frac{C^{90}_{0}}{C_{ext}}(1 - e^{-A_c Q_{ext}})} \quad (10)$$

where F_{ij} is the Fresnel transmission terms and C^n_m is the scattering efficiency between angles m and n. Since Q_{ext} increases rapidly with diameter in the range of 20–150 nm for AgNWs, H increases significantly with diameter.[110,349] Eqn (10) indicates that H is linearly related to A_c, which has been demonstrated experimentally.[350] However, theoretical models that relate H and R_S to provide an FoM are still missing and deserve more research.

5.1.2. Performance comparison of MNW TEs. The MNW TEs, fabricated by self-assembly, alignment, and patterning approaches, have been widely reported to have higher FoMs than those of the corresponding MNW networks with random orientation. A self-assembled AgNW mesh has better electrical connections and a higher open area ratio, which can improve optoelectrical performance.[45] Ordered arrays of MNWs can achieve high conductivity at high transparency with minimal stacking and overlap.[91] Patterned AuNWs have shown superior performance among AuNW-based TEs due to the voids in the pattern and plasma-annealed AuNW bundles.[108] Since TEs with a high FoM are desirable for constructing high-performance devices, the performances of the MNW TEs fabricated by different methods are summarized in Fig. 18a. The data (T, R_S) of self-assembled MNW TEs show widespread FoMs in the range of 15–300. Very limited TEs have an R_S of $\leq$20 Ohm sq^{-1} coupled with a T of >90%. The superior TEs are the AgNW-bundle meshes which exhibit R_S = 20 Ohm sq^{-1} at T = 93.5% and R_S = 25 Ohm sq^{-1} at T = 97%; however, the corresponding hazes are higher than 2.6% due to the large scattering efficiency of microscale bundle width.[34,45] By comparison, patterned MNW TEs have relatively better optoelectrical performances with FoMs mainly in the range of 80–500 (blue highlight in Fig. 18a). Some AgNW TEs show an R_S of 10–50 Ohm sq^{-1} at $T \geq$ 90%, which meets the requirements of displays and touch panels. The aligned MNW-based TEs have widely dispersed R_S, ranging from 2 to 400 Ohm sq^{-1}, with most $T \geq$ 85%. Alignment of MNWs can effectively increase FoMs to 300–800, as indicated by the red highlight in Fig. 18a. The better performance of aligned MNWs has the support of percolation theory, demonstrating that the conductivity follows a percolation-like dependence on the alignment degree; that is, a slightly aligned MNW network has the highest conductivity along the aligned direction.[351,352] For a given NW density, a cross-aligned AgNW network has >50% less R_S than a random AgNW network.[92] In brief, aligned and patterned MNW networks are superior to self-assembled MNW networks in terms of FoM. The first two TEs have shown an R_S of 5–50 Ohm sq^{-1} at $T \geq$ 90%, which can meet the requirements for most optoelectronics.

5.1.3. Optoelectrical applications. MNW-based TEs have been utilized to construct various flexible optoelectronic

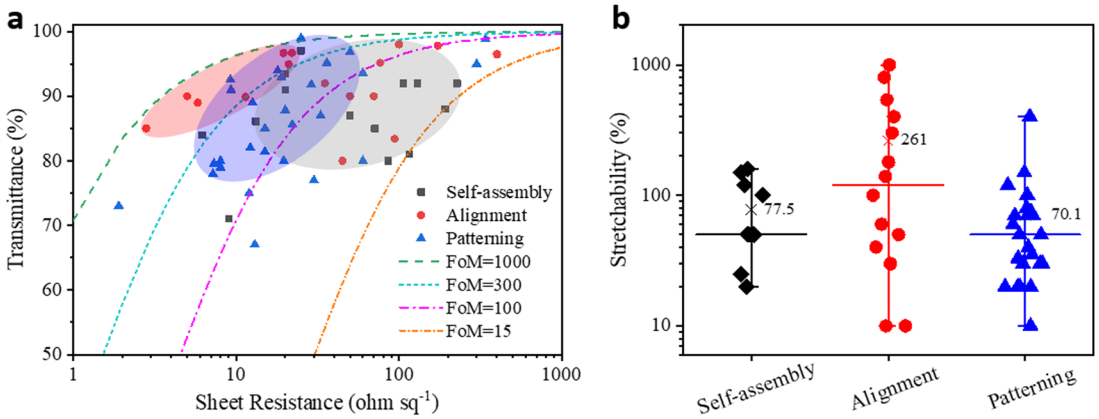

Fig. 18 (a) Transmittance *versus* sheet resistance of the MNW-based TEs fabricated by self-assembly,[34,36,45,47–49,108,131,134,327,353–357] alignment,[12,28,29,53,77,79,81,86,88,91,95,96,102,161,170,358,359] and patterning methods.[37,105,145,216,217,219,220,223,230,234,238,241,244,249,259,262,263,281,305,308,314,315,317,324,335,340,360–364] The dotted lines derived from eqn (6) denote the performances at different FoMs. (b) Stretchability of the MNW-based SEs fabricated by self-assembly,[34,36,124,131,365–371] alignment,[29,77,82,87,89,167,358,372–376] and patterning methods.[37,139,232,244,251,259,283,293,308,315,317,340,361]

devices, including LEDs,[377] solar cells,[86,281,359] touch panels,[34,36,91] heaters,[220] electromagnetic interference shielding,[14,22] memristors,[275] skin-attachable loudspeakers and microphones,[13] *etc.* The mesh structure, alignment, and patterns of MNWs play vital roles in the performance, function, and integration of devices. Herein, only LEDs, solar cells, and touch panels based on MNWs are briefly discussed, as demonstrations of the advantages of self-assembly, alignment, and patterning methods, because TEs are essential components in the three types of devices.

LEDs. The performances of different LEDs have been improved by assembling MNWs into specific structures. One structure is bi-aligned MNW networks which enhance the external quantum efficiency (EQE) of quantum dot LEDs (QLEDs) and organic LEDs (OLEDs) through alignment-enhanced FoMs.[86,227,378] The EQE of a reported OLED with an aligned AgNW TE is 20% higher than that of a reference device with an ITO electrode.[378] The EQE of the QLEDs is enhanced by a factor of 7 compared to the QLED with a random AgNW network.[227] Due to the improved uniformity of the bi-aligned AgNW network, a QLED with 30 μm linewidth is lighted by a laser-patterned AgNW electrode.[227] Another structure for LED improvement is MNWs with pattern designs. A nanopatterned AgNWs/ZnO TE was used to enhance the light outcoupling of green-emitting perovskite LEDs, achieving a high EQE of 24.5%.[379] With the inherent stretchability of AgNW networks, serpentine AgNW electrodes effectively reduce local strain, improving the bending stability of OLEDs.[380]

Solar cells. As in LEDs, MNW alignment finds application in organic solar cells (OSCs), in which enhanced FoMs account for the improvement of power conversion efficiency (PCE).[86,359,378] In an interesting report, aligned AgNWs were decorated with SiO_2 NPs to enhance electric field intensity at NP–NW interfaces through a strong gap-plasmon effect (Fig. 19a and b), which improves the J_{sc} value and EQE and achieves a PCE of 9.19% in the OSCs (Fig. 19c–f).[377] A cross-aligned AgNWs/polyester-based TE induced a large-grained perovskite film, which imparts a perovskite SC with a PCE of 17.51%.[381] Patterned MNWs improve the PCE of solar cells by enhancing transparency and the light trapping effect.[105] Multi-length scale AgNW grids provide OSCs with a PCE of 9.02%, higher than that of the AgNW uniform film-based solar cell.[105] A nanoimprint-AgNW mesh not only has high FoMs (335), but also induces light-trapping through the light scattering from NWs to increase optical absorption of OSCs.[382]

Touch panel. A touch panel (TP) is based on either a uniform or a patterned TE. For the former, researchers developed high-performance MNW TEs with emphasis on enhancing FoM and uniformity.[34,91,134,255,383] Highly cross-aligned AgNW networks were fabricated by Meyer-rod coating combined with electrostatic adsorption, which showed a high FoM (Π = 479, n = 0.12) and a small standard deviation (1.2) of R_S and were used for the construction of a four-wire resistive-type TP (RTP) (Fig. 19g–i).[91] By using a coffee-ring self-assembly method, Xiong *et al.* prepared porous AgNW networks with a low R_S (25 Ω sq^{-1}) at a high T (97%) for surface capacitive TPs (SCTPs).[34] The disadvantage of RTPs and SCTPs is that they cannot realize multi-touch. To sense multi-touch, patterned electrodes are required to construct projected capacitive TPs (PCTPs).

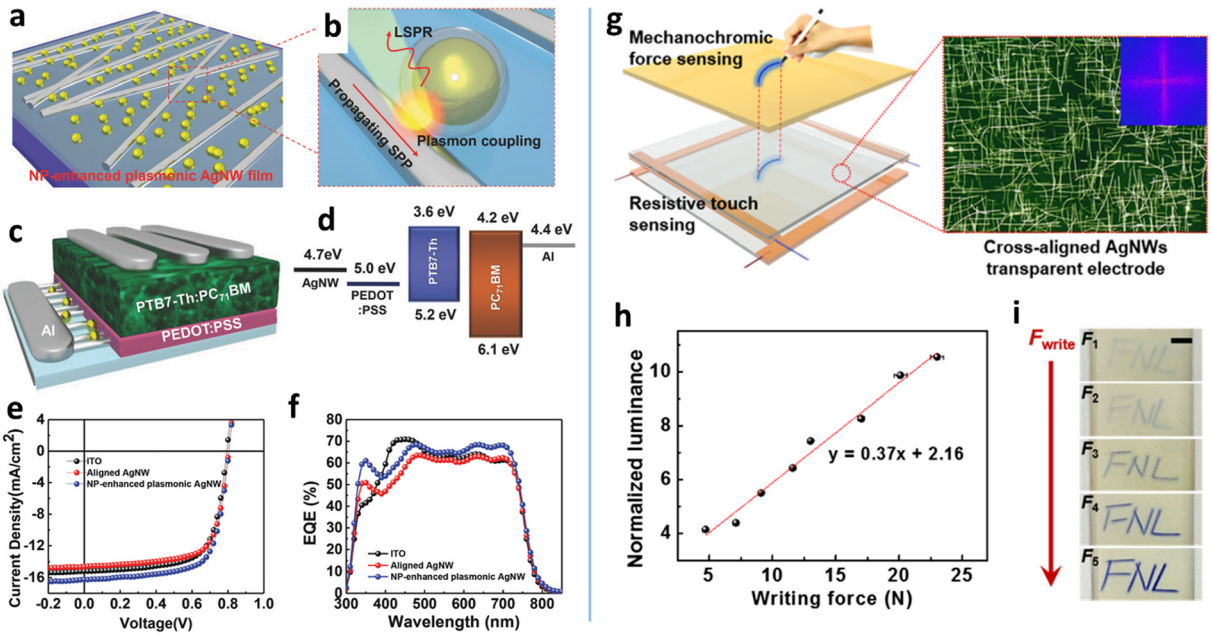

Fig. 19 (a) Schematic of the SiO_2 NP-decorated, aligned AgNWs and (b) the plasmon coupling between the NP and AgNW. (c) Schematic of an OSC device with the aligned NP–AgNW electrode and (d) the energy level diagram. (e) J–V curves and (f) IPCE spectra of the OSCs with different TEs. Reproduced with permission.[377] Copyright 2018, WILEY-VCH. (g) Schematic of the force-sensitive TP with bi-aligned AgNW TEs. (h) Normalized luminance at 448 nm *versus* the writing force. (i) Digital photographs of color change on the TP *versus* different writing forces. Reproduced with permission.[91] Copyright 2017, American Chemical Society.

Using an etching-free photolithography method, Shin *et al.* fabricated an AgNW-based PCTP which consisted of one glass and two flexible AgNW films (GFF).[264] Cann *et al.* utilized laser patterning to fabricate a single-sided, single-layer AgNW-based PCTP on a glass substrate (OGS).[226] Our group used laser ablation to fabricate a single-sided, embedded AgNW-based flexible PCTP on PET, demonstrating multi-touch.

5.2. Stretchable electrodes and applications

5.2.1. Stretchability. MNW networks are intrinsically stretchable due to strain dissipation of their porous structure.[384] Therefore, MNW-based conductors can be used as SEs for stretchable optoelectronics, including stretchable displays,[244] piezoresistive sensors,[385] wearable heaters,[386] epidermal electronics,[387] *etc.* An important parameter of SEs is stretchability which strongly depends on the morphologies of MNW networks. Therefore, the stretchability of MNW SEs assembled by different methods is summarized here.

Fig. 18b shows the stretchability distributions of the MNW SEs which are catalogued according to the three types of assembling methods. Nearly all of the data are from 2D film-shaped SEs. Most self-assembled SEs have stretchability in the range of 20–160%, with an average value of 77.5%. A 2D porous Au mesh on a prestrained PDMS is reported to have a stretchability of up to 160%.[368] The largest stretchability of 800% is obtained by a 3D AgNW-hydrogel aerogel with a cellular structure which is fabricated by the freeze-drying self-assembly method.[109] The patterned MNW-based SEs have more widespread stretchability, spanning from 10% to 400%. The stretchability of the in-plane MNW meshes is generally less than 150%. One outstanding MNW structure with a stretchability of $>400\%$ is the kirigami-engineered AgNW SE which is patterned by a UV laser.[387] The kirigami design can effectively reduce strains in MNW networks through 3D buckling under large tensile deformation at the device level, so that the AgNW SE under strains of 0–400% exhibits only a 3% change in resistance. As for aligned MNW networks, the stretchability spans from 10% to 1000%, with an average value of 261%. Two representative aligned MNW SEs are the horizontally aligned AgNW nanomembrane and the vertically aligned enokitake-like AuNW microfilm, which are fabricated by a modified LB assembly and a modified seed-mediated electroless plating method, respectively.[87,388] They possess stretchabilities of up to 1000% and 800% respectively, which are the highest-ranking stretchability values ever reported for MNW-based SEs.

In brief, the MNW SEs fabricated by self-assembly, alignment, and patterning methods have demonstrated high stretchability in the ascending order by discrete degree: aligned MNWs $>$ patterned MNWs $>$ self-assembled MNWs. The stretchability of self-assembled and patterned MNW networks with in-plane structures is mainly in the range of 10–150%, with the majority having a stretchability lower than 100%. The MNWs, which are with 3D structures or can induce out-of-plane deformation, have a higher stretchability of $>200\%$.[109,387] By contrast, the aligned MNW networks can effectively dissipate the applied strain to provide the highest stretchability with a broad distribution of 10–1000%. Since the advanced MNW SEs assembled by the three methods have a stretchability of $>100\%$ which is enough to accommodate skin deformation,[389] various skin-mountable optoelectrical devices have been developed.

5.2.2. Wearable optoelectronics. The great progress in MNW SEs is advancing the development of various wearable, stretchable devices, including stretchable heaters,[259] displays,[390,391] strain sensors,[37] nanogenerators,[17] epidermal bioelectric sensors,[392–394] organic transistors,[395] e-skin,[396] *etc.* Dependent on function requirement, the conductivity of MNW SEs needs to be either strain-insensitive or strain-sensitive. Since there are too many stretchable devices to cover in this article, this review only briefly discusses the two representative devices with strain-sensitive and strain-insensitive SEs: resistive strain sensors and epidermal electronic sensors.

Resistive strain sensors. MNW-based resistive strain sensors typically consist of MNW electrodes and elastomers. The MNW SEs are the sensing units, the performance of which is mainly characterized by stretchability, sensitivity, linearity, *etc.* The sensitivity is quantified by the gauge factor (GF):

$$\mathrm{GF} = \frac{\Delta R/R_0}{\Delta L/L_0} = \frac{\Delta R}{R_0 \varepsilon} \tag{11}$$

where ΔR, R_0, ΔL, L_0, and ε are the resistance change, initial resistance, length change, initial length, and strain, respectively.

The structures of MNW SEs have an essential influence on the performance of strain sensors. There are three patterned structures for performance enhancement: (1) patterning MNWs into micro-lined electrodes. A micropatterned AgNW–acrylate SE with a narrow linewidth can evade the Poisson compression effect through the formation of parallel cracks (Fig. 20a),[37] which enhances the GF (3.2×10^7) by 200 times as compared to that of the corresponding bulk film, with a transparency of 90.3% and a maximum stretchability of 20%. High sensitivity enables the sensor to clearly detect the percussion (P), tidal (T), and diastolic (D) waves and dicrotic notch of the wrist pulse at a high signal-to-noise ratio (Fig. 20b and c), so that the comprehensive medical parameters including augmentation index, transit time, and K value can be estimated from the pulse signals. (2) Patterning the substrate into meshed structures. A circle-meshed substrate can redistribute the stress uniformly and induce cracks in the AgNW network without total disconnection, giving rise to a high GF of 846 with a large strain range (150%) and a high transmittance (88.3%).[397] (3) Patterning MNWs and the substrate. An AgNW mesh is formed in a square plate array with concave channels, which induces stress concentration in the concave lines.[398] As a result, a large GF of 150 000 with a large stretchability of 60% and a good linearity of $R^2 = 0.989$ is achieved, which is able to detect the full-range human body motions.

Aligned architectures have been reported to effectively increase the stretchability of MNW SEs to $>300\%$.[87,373,375] However, uniform aligned films usually exhibit low GFs of less than 10.[388] A vertically aligned AuNW (v-AuNW) film patterned with pinholes can cause a 3.1-fold increase in the GF (28.6)

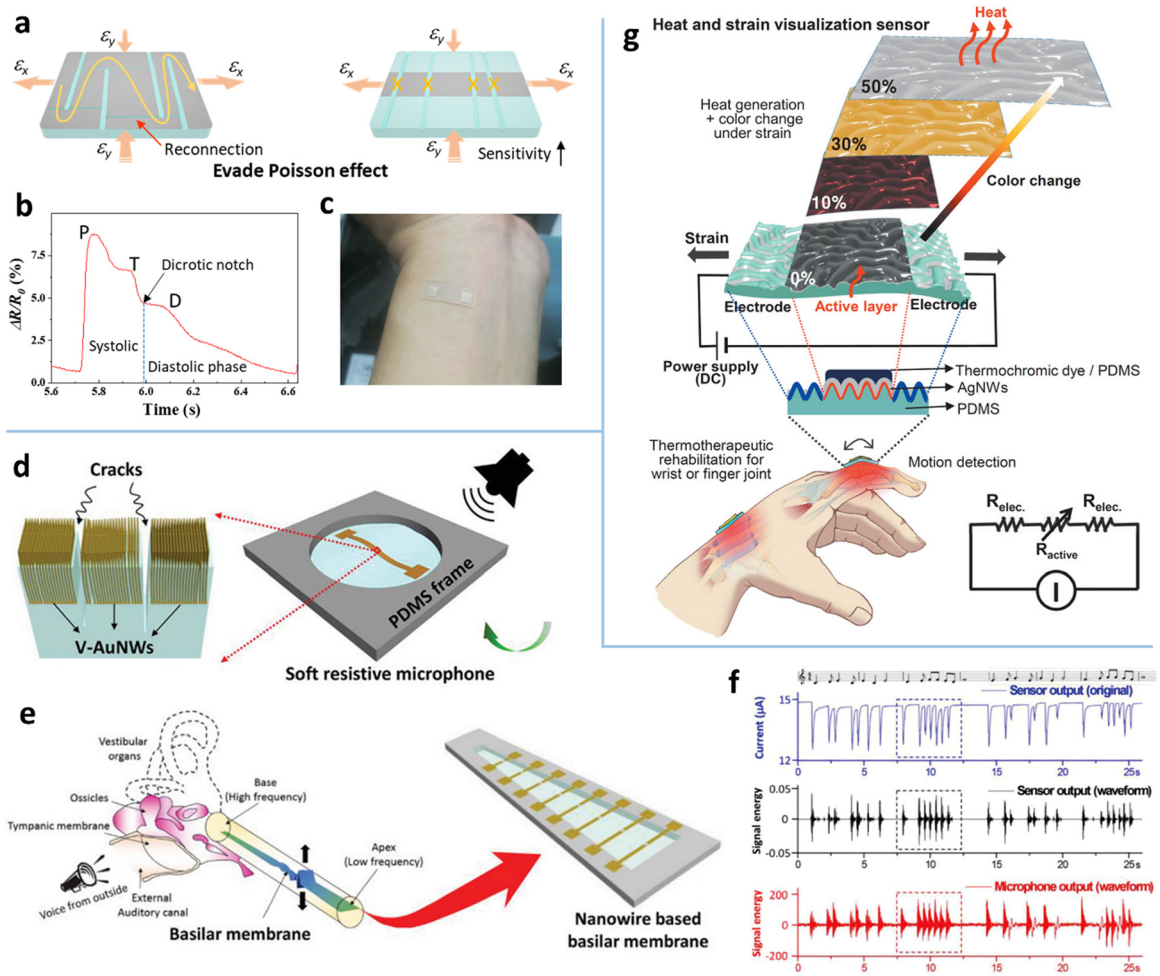

Fig. 20 (a) Schematic of GF enhancement by changing crisscross cracks in a bulk AgNW film to parallel cracks in the patterned AgNW–acrylate composite. (b) Resistance signal of wrist pulse. (c) The AgNW–acrylate based strain sensor on the wrist. Reproduced with permission.[37] Copyright 2020, American Chemical Society. (d) Schematic of the soft resistive microphone and v-AuNWs film. (e) Schematic illustration of the human ear with an uncoiled cochlea and the artificial basilar membrane made of eight cracked v-AuNW strain sensors. (f) Sensor output, detection, and commercial microphone waveform in response to a piece of music. Reproduced with permission.[399] Copyright 2020, WILEY-VCH. (g) Schematic of the thermotherapeutic patch integrated with a strain sensor and a thermochromic layer and its working mechanism. Reproduced with permission.[400] Copyright 2020, WILEY-VCH.

compared to the counterpart without patterned holes.[365] The detected pulse signal shows four times enhanced amplitude with clear systolic, diastolic, and notch peaks. The enokitake-mushroom-like v-AuNWs are also combined with the cracked Au film, which enhances the GF from 0.17 to 1023 in the strain range of 0–20%.[401] The v-AuNWs with local cracks, as a resistive acoustic sensor, have ultrahigh acoustic sensitivity and can detect the waveform of musical notes with distinguishable frequencies, which is comparable to that of a commercial microphone (Fig. 20d–f).[399] A soft artificial basilar membrane is constructed by integrating the eight acoustic sensors on a flexible trapezoid frame (Fig. 20e), which achieves high-frequency selectivity in the range of 319–1951 Hz with a high sensitivity of 0.48–4.26 Pa^{-1}.

Self-assembly of AgNWs onto a wrinkled PDMS, as a strain sensor, provides larger stretchability.[400] The AgNW strain sensor is further integrated with a thermochromic dye to construct a user-interactive thermotherapeutic device (Fig. 20g). The thermochromic film on the strain sensor with the same current bias can cause a color change under different tensile strains. The self-assembled, wrinkled AgNW SE endows the device with a high stretchability of 100% and linear sensitivity. This device can be used for the precise rehabilitation of injured tissues through strain-controllable and color-visible heating.

Epidermal electronic sensors. Epidermal electronics refer to ultra-thin electronic devices with a thickness less than tens of microns that can adhere to the skin comfortably and imperceptibly. MNWs are generally assembled into specific structures to construct strain-insensitive SEs which are ideal building blocks for such devices. The vertically aligned AuNW film with a thickness of 300 nm has a low GF of 0.17 within 20% strain.[401] A ''stick-and-play'' gold E-tattoo with multifunction is realized by combining the AuNWs with a tattoo transfer

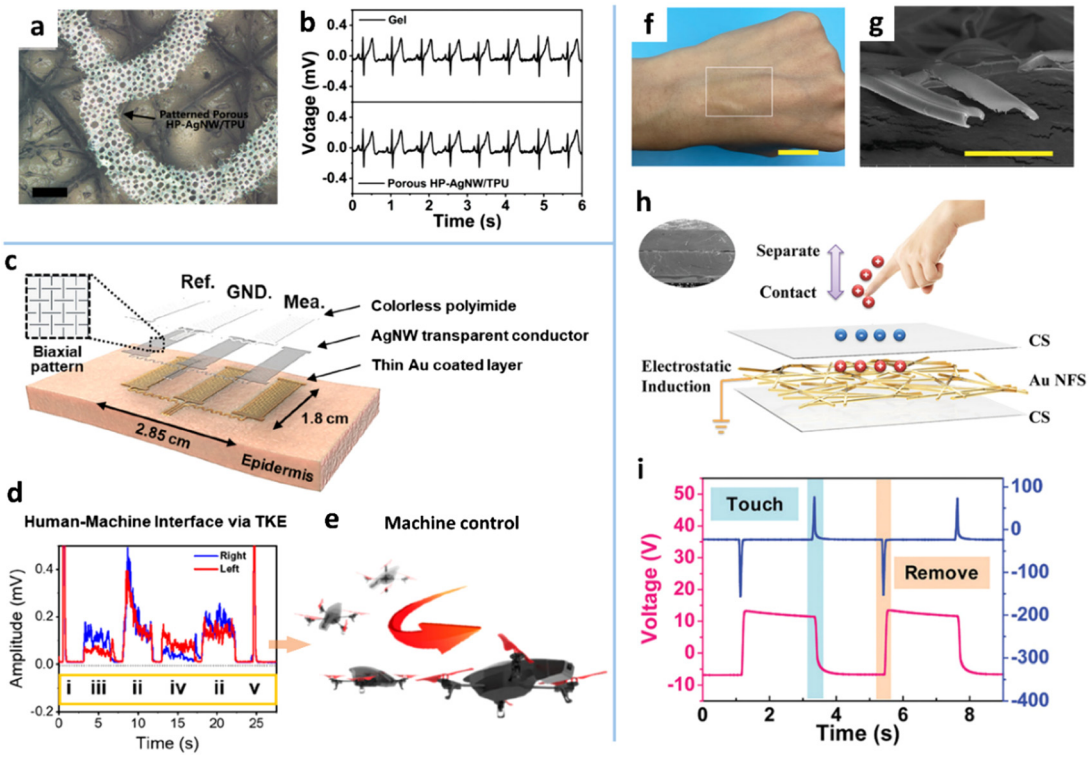

Fig. 21 (a) OM image of the patterned porous AgNW electrode on skin. (b) ECG spectra monitored by the porous AgNW electrode and gel electrode. Reproduced with permission.[133] Copyright 2020, American Chemical Society. (c) Configuration of the transparent kirigami electrode (TKE)-based sensor. (d) sEMG signals from the TKEs on the left/right arms. (e) Schematic of flight manipulation of a drone with the TKEs. Reproduced with permission.[387] Copyright 2019, American Chemical Society. (f) Photograph of the AuNW/chitosan-based electrode on skin. (g) SEM image of the AuNW cross-section. (h) Device structure of the e-skin. (i) Output voltage and current curves of the e-skin under cyclic touches. Reproduced with permission.[402] Copyright 2022, WILEY-VCH.

technique. It successfully detects the physiological signals of strain, strain direction, pressure, temperature, and glucose/lactate levels. Using the BF method and laser ablation, Zhu *et al.* reported a porous, epidermal SE with a thickness of 4.6 μm (Fig. 21a).[133] This SE is totally reversible within 15% strain after the first stretch. The high-conductivity, air permeable, ultrathin, embedded structure endows the SE with excellent stability and low impedance. The detected ECG signal has a comparable SNR (7.0 dB) to that (7.1 dB) of the commercial gel electrode (Fig. 21b). The AgNW thin film with a kirigami pattern exhibits a $<3\%$ change in resistance under 0–400% strain.[387] Long-term monitoring of bioelectrical signals is achieved after selectively passivating the AgNW kirigami. Surface electromyogram (sEMG) signals from the left and right arms are used for command classification based on their root-mean-square values, which successfully realizes the flight manipulation of a quadrotor drone (Fig. 21c–e). In addition to detecting biopotential signals, MNWs can also construct a self-powered electronic skin, where nanofiber templated AuNWs are the intermediate electrode between the substrate and the dielectric layer made of microscale cracked chitosan membranes (Fig. 21f–h).[402] The fabricated single-mode triboelectric nanogenerator exhibits a pressure sensitivity of 0.012 kPa^{-1} in the range of 0 to 70 kPa and can be used as an epidermal touch/pressure sensor (Fig. 21i).

6. Conclusions and perspectives

MNWs with the 1D inherent structure are ideal transport materials for electrons, photons, phonons, *etc.* Assembling MNWs into macroscale architectures manifests or further enhances these transport properties, which breeds and expedites many discoveries and novel applications, such as the newly flourishing stretchable electronics. So far, great strides have been made in the morphology manipulation of MNWs with diverse assembly strategies since the turn of the century. In this review, the main strategies for the assembly of MNWs have been summarized, including the self-assembly methods that spontaneously organize MNWs into a specific regular geometric appearance, the alignment methods which deposit MNWs into an anisotropic architecture with one or more aligning directions, and the patterning methods which process MNWs into well-designed structures. Each assembly method has its merits and limitations, which are summarized in Table 3. And the progress, main features, and key issues of these methods are also highlighted below.

The self-assembly of MNWs generally yields two types of structures: 2D porous networks and 3D foamy structures. The 2D porous films used as TEs and SEs are reported to have higher optoelectrical performance and stretchability than disordered MNW networks. However, their FoM values are generally less

Table 3 Merits and limitations of various MNW assembly techniques

Methods	Merits	Limitations
Self-assembly		
Coffee-ring effect	Dynamic control over MNW deposition; mass manufacture; compatible with various materials	Requires substrate modification; high haze as TE; impractical in fabrication of 3D structures
Ice templating	Versatility in porous structures; simplicity; distinct physico/mechanical attributes	Requires freeze drying and posttreatment to improve performance; special setup
Breath figure	Low-cost; time-saving; easy implementation	Limitations in the sizes of the pores; poor control of the surface morphology
Alignment		
Bubble blowing	Simplicity; low-cost; compatible with various substrates; high alignment degree	Difficult to achieve high-density NW deposition; low performance; poor manufacturability
Shear flow	Simplicity; large area; low-cost; good manufacturability	Moderate alignment degree
Printing	High positional control; high alignment degree	Special setup; impractical for large-area manufacture
Electrospinning	High alignment; large areas; high position control	Requires posttreatment to remove the polymer matrix; lower conductivity
LB technique	Ultrahigh alignment; compact deposition; high electromechanical performance	Rigid condition control; requires surface modification and transfer process; time-consuming
Electromagnetic field	Facile and precise control; long ranged; non-contact forces	Small forces in microscale and nanoscale; requires auxiliary electrodes, uniformity in NW length, or surface modification
Patterning		
Photolithography	Mature industrial technology; high resolution	Complex process; expensive equipment; environmentally unfriendly
Etching-free lithography	Environmentally friendly; low cost; large-area production	Requires elaborate tailoring of MNW inks and interfaces to achieve adhesion difference
Laser ablation	Designable patterns; non-contact; mask-free	Potential damage to the substrates; low productivity; expensive equipment
PRI method	High resolution; low visibility of patterns	Requires high-temperature annealing; surface modification
IJP/AJP/EHD printing	Noncontact; mask-free; material saving; designable patterns	Nozzle clogging; moderate resolution
Screen printing	High productivity; controllable deposition; easy implementation	Easy clogging of screen mesh; moderate resolution
Reverse offset printing	High resolution; large-area manufacture	Complex process; expensive equipment; high pressure
Wetting–dewetting	High resolution; complex patterns	Surface modification; lab scale fabrication; residual NWs in unpatterned regions
Mask-assisted methods	Material saving; simple; low cost	High requirements for mask; rough edges; difficult to fabricate complex patterns

than those of aligned and patterned MNW networks (Fig. 18a). In addition, the NW bundles induced by the self-assembly process increase the haze of the networks due to increased scattering cross-section, which is disadvantageous for application in touch panels and displays. The self-assembled MNW TEs with high hazes may be better suited for solar cells, which deserves further research. Besides, we believe that the self-assembled MNW micromeshes have great potential in permeable conductors for wearable on-skin electronics. As for 3D structures, the most amazing architecture of MNWs is the aerogel that combines the merits of MNWs and aerogels, exhibiting unparalleled potential in electrocatalysis, sensing, and plasmonics. For instance, an AgNW aerogel combined with a hydrogel shows a superhigh stretchability of 800%. So far, more attention has been paid to constructing new structures or pursuing high performance, while the in-depth study of formation mechanisms for MNW aerogels is lacking.[403]

Aligned MNW assemblies with a single direction and multi-direction have been realized by various methods. Based on the driving force, these methods can be categorized into shear flow-induced alignment, LB techniques, and electromagnetic field methods. The shear force-based methods have the advantages of being a simple process and being compatible with the R2R process, the LB techniques enable compact MNW assembly with an ultrahigh alignment degree, and the electromagnetic field methods show facile and precise manipulation of MNW deposition *via* distribution, strength, and frequency of the applied electromagnetic field. In terms of scalability, the rod/bar/blade (with or without a structured surface) coating methods are the most feasible methods; however, the alignment degree of the methods is unsatisfactory. In addition, the patterned, aligned array of MNWs that calls for the positional control of the NWs on the substrates is unable to be achieved by the simple rod/bar/blade coating methods. Modified rod/bar/blade coating methods or a combination of a few existing approaches still hold considerable appeal.

Well-defined, high-resolution MNW patterns have been fabricated on different substrates through various top-down and bottom-up strategies. Besides the etching-based photolithography and laser ablation, the etching-free top-down methods based on the adhesion difference and PRI have come out recently with patterning resolution down to 3 μm for AgNWs. To simplify the patterning process, novel bottom-up strategies such as IJP and wetting–dewetting self-assembly have been rapidly developed recently. The linewidth has been lowered to <50 μm for IJP and to 3.6 μm for vacuum filtration-based patterning. Still, several significant challenges remain. First, narrower linewidths of MNW networks lead to large variation in resistance among the

electrodes with the same size. A conductive composite would be a good solution, which needs further studies. Second, for AgNW and CuNW-based TEs, patterning traces are easily visible to the naked eyes due to their strong scattering in the visible wavelength range, which hinders the commercialization in displays and touch panels. Semi-etching and thermal fragmentation can reduce the patterning visibility but also complicate the patterning process. Further work is still needed to resolve this issue in a simple manner.

Manipulating MNW assembly have already proven to enhance performance and offer new features for various devices. However, most studies just provide demonstrations or proof of concept. A scalable assembly of MNWs with performance enhancement, precise control, relatively low costs, and high manufacturability are the key to practical applications. For instance, bi-alignment assembly of MNWs is not easily compatible with the R2R process. Besides, improvements in anticorrosion, thermal stability, conductivity, adhesion, and/or surface roughness should be taken into account in the assembly process. A one-step process to achieve high-performance structures is desirable and deserves more research. With continuous and enormous effort in structure design, fabrication optimization, and multi-level integration for MNWs, we anticipate that MNW-based systems will continue to have a revolutionary impact in numerous fields.

Except the SAM-based PRI self-assembly method, most strategies reviewed herein are not only limited to MNWs, but also applicable to other types of nanowires. The well-known techniques including the coffee-ring effect, breath figure, Langmuir–Blodgett technique, bubble blowing, electrospinning, dewetting self-assembly, and printing methods have been widely reported for assembling various types of 1D materials, such as CNTs and semiconductor nanowires.[100,115,121,123,171] Other methods based on surface/interface engineering and flow-field effects should also apply to those nanomaterials which can be dispersed in solvent and properly surface-modified. It is believed that the principles, ideas, and even processing of these assembly strategies are universal for various nanomaterials, which would be conducive to the development of micro/nano fabrication.

Conflicts of interest

There are no conflicts to declare.

Acknowledgements

The work is supported by the National Natural Science Foundation of China (61904067, 61805108, 62175094), Basic and Applied Basic Research Foundation of Guangdong province (2022A1515010272, 2020A1515011498), Basic and Applied Basic Research Foundation of Guangzhou City (202102020758), Scientific and Technological Projection of Guangdong province (2020B1212060030), Key-Area Research and Development Program of Guangdong province (2019B010934001), open funding from the State Key Laboratory of Optoelectronic Materials and Technologies (Sun Yat-Sen University, OEMT-2022- KF-08) and the Fundamental Research Funds for the Central Universities (21621405, 21620328).

References

1 S. Pan, H. Zou, A. C. Wang, Z. Wang, J. Yu, C. Lan, Q. Liu, Z. L. Wang, T. Lian, J. Peng and Z. Lin, *Angew. Chem., Int. Ed.*, 2020, **59**, 14942–14949.
2 B. Li, W. Han, M. Byun, L. Zhu, Q. Zou and Z. Lin, *ACS Nano*, 2013, **7**, 4326–4333.
3 D. Huo, M. J. Kim, Z. Lyu, Y. Shi, B. J. Wiley and Y. Xia, *Chem. Rev.*, 2019, **119**, 8972–9073.
4 J. L. Wang, M. Hassan, J. W. Liu and S. H. Yu, *Adv. Mater.*, 2018, **30**, e1803430.
5 K. Wang, L. W. Yap, S. Gong, R. Wang, S. J. Wang and W. Cheng, *Adv. Funct. Mater.*, 2021, **31**, 2008347.
6 B. Lee, J. Y. Oh, H. Cho, C. W. Joo, H. Yoon, S. Jeong, E. Oh, J. Byun, H. Kim, S. Lee, J. Seo, C. W. Park, S. Choi, N. M. Park, S. Y. Kang, C. S. Hwang, S. D. Ahn, J. I. Lee and Y. Hong, *Nat. Commun.*, 2020, **11**, 663.
7 C. Pan, L. Dong, G. Zhu, S. Niu, R. Yu, Q. Yang, Y. Liu and Z. L. Wang, *Nat. Photonics*, 2013, **7**, 752–758.
8 H. G. Manning, C. G. da Rocha, C. O. Callaghan, M. S. Ferreira and J. J. Boland, *Sci. Rep.*, 2019, **9**, 11550.
9 H. Hosseinzadeh Khaligh, K. Liew, Y. Han, N. M. Abukhdeir and I. A. Goldthorpe, *Sol. Energy Mater. Sol. Cells*, 2015, **132**, 337–341.
10 C. Lee, Y. Oh, I. S. Yoon, S. H. Kim, B. K. Ju and J. M. Hong, *Sci. Rep.*, 2018, **8**, 2763.
11 H. J. Seok, J. K. Kim and H. K. Kim, *Sci. Rep.*, 2018, **8**, 13521.
12 T. Ackermann, R. Neuhaus and S. Roth, *Sci. Rep.*, 2016, **6**, 34289.
13 S. Kang, S. Cho, R. Shanker, H. Lee, J. Park, D.-S. Um, Y. Lee and H. Ko, *Sci. Adv.*, 2018, **4**, eaas8772.
14 W. Chen, L.-X. Liu, H.-B. Zhang and Z.-Z. Yu, *ACS Nano*, 2020, **14**, 16643–16653.
15 G. Zeng, W. Chen, X. Chen, Y. Hu, Y. Chen, B. Zhang, H. Chen, W. Sun, Y. Shen, Y. Li, F. Yan and Y. Li, *J. Am. Chem. Soc.*, 2022, **144**, 8658–8668.
16 H. Kang, C. Zhao, J. Huang, D. H. Ho, Y. T. Megra, J. W. Suk, J. Sun, Z. L. Wang, Q. Sun and J. H. Cho, *Adv. Funct. Mater.*, 2019, **29**, 1903580.
17 X. Peng, K. Dong, C. Ye, Y. Jiang, S. Zhai, R. Cheng, D. Liu, X. Gao, J. Wang and L. Wang Zhong, *Sci. Adv.*, 2020, **6**, eaba9624.
18 J. Bang, Y. Jung, H. Kim, D. Kim, M. Cho and S. H. Ko, *Nano-Micro Lett.*, 2022, **14**, 49.
19 S. M. Lee, J. H. Lee, S. Bak, K. Lee, Y. Li and H. Lee, *Nano Res.*, 2015, **8**, 1882–1892.
20 P. Li, J. G. Ma, H. Y. Xu, D. Lin, X. D. Xue, X. Z. Yan, P. Xia and Y. C. Liu, *J. Alloys Compd.*, 2016, **664**, 764–769.
21 J. M. Lee, Y. H. Kim, H. K. Kim, H. J. Kim and C. H. Hong, *Sci. Rep.*, 2020, **10**, 4592.
22 Y. Yang, S. Chen, W. Li, P. Li, J. Ma, B. Li, X. Zhao, Z. Ju, H. Chang, L. Xiao, H. Xu and Y. Liu, *ACS Nano*, 2020, **14**, 8754–8765.

23 J. Wei, Z. Lin, Z. Lei, Y. Xu, Z. Zhao, T. Zhao, Y. Hu, H. Miao and R. Sun, *ACS Appl. Mater. Interfaces*, 2022, **14**, 5940–5950.
24 J. Liu, D. Jia, J. M. Gardner, E. M. J. Johansson and X. Zhang, *Mater. Today Energy*, 2019, **13**, 152–185.
25 B. Li, B. Jiang, H. Tang and Z. Lin, *Chem. Sci.*, 2015, **6**, 6349–6354.
26 L. Hu, H. Wu and Y. Cui, *MRS Bull.*, 2011, **36**, 760–765.
27 Q. Tang, H. Li, Y. Song, W. Xu, W. Hu, L. Jiang, Y. Liu, X. Wang and D. Zhu, *Adv. Mater.*, 2006, **18**, 3010–3014.
28 S. K. Duan, Q. L. Niu, J. F. Wei, J. B. He, Y. A. Yin and Y. Zhang, *Phys. Chem. Chem. Phys.*, 2015, **17**, 8106–8112.
29 H. Hu, S. Wang, S. Wang, G. Liu, T. Cao and Y. Long, *Adv. Funct. Mater.*, 2019, **29**, 1902922.
30 J. W. Liu, J. L. Wang, W. R. Huang, L. Yu, X. F. Ren, W. C. Wen and S. H. Yu, *Sci. Rep.*, 2012, **2**, 987.
31 Y. Lee, S.-Y. Min and T.-W. Lee, *Macromol. Mater. Eng.*, 2017, **302**, 1600507.
32 B. Reiser, D. Gerstner, L. Gonzalez-Garcia, J. H. M. Maurer, I. Kanelidis and T. Kraus, *ACS Nano*, 2017, **11**, 4934–4942.
33 J. Jung, H. Cho, R. Yuksel, D. Kim, H. Lee, J. Kwon, P. Lee, J. Yeo, S. Hong, H. E. Unalan, S. Han and S. H. Ko, *Nanoscale*, 2019, **11**, 20356–20378.
34 J. Xiong, S. Li, Y. Ye, J. Wang, K. Qian, P. Cui, D. Gao, M.-F. Lin, T. Chen and P. S. Lee, *Adv. Mater.*, 2018, **30**, 1802803.
35 R. Bian, L. Meng, C. Guo, Z. Tang and H. Liu, *Adv. Mater.*, 2019, **31**, 1900534.
36 J. Han, J. Yang, W. Gao and H. Bai, *Adv. Funct. Mater.*, 2021, **31**, 2010155.
37 G.-S. Liu, F. Yang, J. Xu, Y. Kong, H. Zheng, L. Chen, Y. Chen, M. X. Wu, B.-R. Yang, Y. Luo and Z. Chen, *ACS Appl. Mater. Interfaces*, 2020, **12**, 47729–47738.
38 F. Guo, P. Kubis, T. Przybilla, E. Spiecker, A. Hollmann, S. Langner, K. Forberich and C. J. Brabec, *Adv. Energy Mater.*, 2015, **5**, 1401779.
39 K. Zilberberg and T. Riedl, *J. Mater. Chem. A*, 2016, **4**, 14481–14508.
40 M.-R. Azani, A. Hassanpour and T. Torres, *Adv. Energy Mater.*, 2020, **10**, 2002536.
41 T. Araki, T. Uemura, S. Yoshimoto, A. Takemoto, Y. Noda, S. Izumi and T. Sekitani, *Adv. Mater.*, 2020, **32**, 1902684.
42 Y. Zhang, S.-W. Ng, X. Lu and Z. Zheng, *Chem. Rev.*, 2020, **120**, 2049–2122.
43 H. Hu, S. Wang, X. Feng, M. Pauly, G. Decher and Y. Long, *Chem. Soc. Rev.*, 2020, **49**, 509–553.
44 W. Li, H. Zhang, S. Shi, J. Xu, X. Qin, Q. He, K. Yang, W. Dai, G. Liu, Q. Zhou, H. Yu, S. R. P. Silva and M. Fahlman, *J. Mater. Chem. C*, 2020, **8**, 4636–4674.
45 J. Xiong, S. Li, J.-H. Ciou, J. Chen, D. Gao, J. Wang and P. S. Lee, *Adv. Funct. Mater.*, 2020, **31**, 2006120.
46 O. Jahanmahin, D. J. Kirby, B. D. Smith, C. A. Albright, Z. A. Gobert, C. D. Keating and K. A. Fichthorn, *J. Phys. Chem. C*, 2020, **124**, 9559–9571.
47 I. Khatri, A. Hoshino, F. Watanabe, Q. Liu, R. Ishikawa, K. Ueno and H. Shirai, *Thin Solid Films*, 2014, **558**, 306–310.
48 T. Tokuno, M. Nogi, J. Jiu, T. Sugahara and K. Suganuma, *Langmuir*, 2012, **28**, 9298–9302.
49 J. W. Shin, H. R. Lim, H. B. Cho, Y. T. Kwon and Y. H. Choa, *Nanoscale*, 2021, **13**, 8442–8451.
50 B. Seong, H. S. Park, I. Chae, H. Lee, X. Wang, H. S. Jang, J. Jung, C. Lee, L. Lin and D. Byun, *Langmuir*, 2017, **33**, 3367–3372.
51 Y. He, Y. Chen, Q. Xu, J. Xu and J. Weng, *ACS Appl. Mater. Interfaces*, 2017, **9**, 7826–7833.
52 R. Zhu, Y. Lai, V. Nguyen and R. Yang, *Nanoscale*, 2014, **6**, 11976–11980.
53 A. Sanchez-Iglesias, B. Rivas-Murias, M. Grzelczak, J. Perez-Juste, L. M. Liz-Marzan, F. Rivadulla and M. A. Correa-Duarte, *Nano Lett.*, 2012, **12**, 6066–6070.
54 C. Preston, Y. Xu, X. Han, J. N. Munday and L. Hu, *Nano Res.*, 2013, **6**, 461–468.
55 V. Malgras, Q. Ji, Y. Kamachi, T. Mori, F.-K. Shieh, K. C. W. Wu, K. Ariga and Y. Yamauchi, *Bull. Chem. Soc. Jpn.*, 2015, **88**, 1171–1200.
56 J. Lv, K. Hou, D. Ding, D. Wang, B. Han, X. Gao, M. Zhao, L. Shi, J. Guo, Y. Zheng, X. Zhang, C. Lu, L. Huang, W. Huang and Z. Tang, *Angew. Chem., Int. Ed.*, 2017, **56**, 5055–5060.
57 J. W. Liu, J. Xu, H. W. Liang, K. Wang and S. H. Yu, *Angew. Chem., Int. Ed.*, 2012, **51**, 7420–7425.
58 C. Baratto, V. Golovanova, G. Faglia, H. Hakola, T. Niemi, N. Tkachenko, B. Nazarchurk and V. Golovanov, *Appl. Surf. Sci.*, 2020, **528**, 146959.
59 J. H. Andrea, R. Tao and P. Yang, *Acc. Chem. Res.*, 2008, **41**, 1662–1673.
60 N. Li, G.-W. Huang, X.-J. Shen, H.-M. Xiao and S.-Y. Fu, *J. Mater. Chem. C*, 2013, **1**, 4879.
61 S. R. Darmakkolla, M. Ghobadi, L. Lampert, A. F. Pareira, A. Jenike, M. Tahir and S. B. Rananavare, *Nanoscale*, 2019, **11**, 2679–2686.
62 M. Beheshti, J. Choi, X. Geng, E. Podlaha-Murphy and S. Park, *Microelectron. Eng.*, 2018, **193**, 71–78.
63 O. Trotsenko, A. Tokarev, A. Gruzd, T. Enright and S. Minko, *Nanoscale*, 2015, **7**, 7155–7161.
64 E. M. Freer, O. Grachev, X. Duan, S. Martin and D. P. Stumbo, *Nat. Nanotechnol.*, 2010, **5**, 525–530.
65 A. W. Maijenburg, M. G. Maas, E. J. Rodijk, W. Ahmed, E. S. Kooij, E. T. Carlen, D. H. Blank and J. E. ten Elshof, *J. Colloid Interface Sci.*, 2011, **355**, 486–493.
66 N. Petchsang, M. P. McDonald, L. E. Sinks and M. Kuno, *Adv. Mater.*, 2013, **25**, 601–605.
67 M. J. Bauer, X. Wen, P. Tiwari, D. P. Arnold and J. S. Andrew, *Microsyst. Nanoeng.*, 2018, **4**, 37.
68 Z. Yin, X. Wang, F. Sun, X. Tong, C. Zhu, Q. Lv, D. Ye, S. Wang, W. Luo and Y. Huang, *Sci. Rep.*, 2017, **7**, 12206.
69 D. L. Fan, R. C. Cammarata and C. L. Chien, *Appl. Phys. Lett.*, 2008, **92**, 093115.
70 P. García-Sánchez, J. J. Arcenegui, H. Morgan and A. Ramos, *Appl. Phys. Lett.*, 2015, **106**, 023110.
71 P. P. Donahue, C. Zhang, N. Nye, J. Miller, C. Y. Wang, R. Tang, D. Christodoulides, C. D. Keating and Z. Liu, *ACS Nano*, 2018, **12**, 7343–7351.

72 D. Y. Shin, S. S. Yoo, H. E. Song, H. Tak and D. Byun, *Sci. Rep.*, 2015, **5**, 16704.
73 S. Wu, K. Huang, E. Shi, W. Xu, Y. Fang, Y. Yang and A. Cao, *ACS Nano*, 2014, **8**, 3522–3530.
74 M. C. P. Wang and B. D. Gates, *Mater. Today*, 2009, **12**, 34–43.
75 C. L. Zhang, K. P. Lv, N. Y. Hu, L. Yu, X. F. Ren, S. L. Liu and S. H. Yu, *Small*, 2012, **8**, 2936–2940.
76 T. L. Yang, C. T. Pan, Y. C. Chen, L. W. Lin, I. C. Wu, K. H. Hung, Y. R. Lin, H. L. Huang, C. F. Liu, S. W. Mao and S. W. Kuo, *Opt. Mater.*, 2015, **39**, 118–124.
77 H. Wu, L. Hu, M. W. Rowell, D. Kong, J. J. Cha, J. R. McDonough, J. Zhu, Y. Yang, M. D. McGehee and Y. Cui, *Nano Lett.*, 2010, **10**, 4242–4248.
78 N. G. Rim, C. S. Shin and H. Shin, *Biomed. Mater.*, 2013, **8**, 014102.
79 M. J. Nikzad, N. Mohamadbeigi, S. K. Sadrnezhaad and S. M. Mahdavi, *ACS Omega*, 2019, **4**, 21260–21266.
80 G. H. Kim, J. H. Shin, T. An and G. Lim, *Sci. Rep.*, 2018, **8**, 13581.
81 K. Azuma, K. Sakajiri, H. Matsumoto, S. Kang, J. Watanabe and M. Tokita, *Mater. Lett.*, 2014, **115**, 187–189.
82 K. N. Al-Milaji, Q. Huang, Z. Li, T. N. Ng and H. Zhao, *ACS Appl. Electron. Mater.*, 2020, **2**, 3289–3298.
83 S.-P. Chen, J. R. Durán Retamal, D.-H. Lien, J.-H. He and Y.-C. Liao, *RSC Adv.*, 2015, **5**, 70707–70712.
84 W. Kim, C. H. Jang and G. H. Kim, *Nano Lett.*, 2019, **19**, 8612–8620.
85 H. Lee, B. Seong, J. Kim, Y. Jang and D. Byun, *Small*, 2014, **10**, 3918–3922.
86 S. Kang, T. Kim, S. Cho, Y. Lee, A. Choe, B. Walker, S. J. Ko, J. Y. Kim and H. Ko, *Nano Lett.*, 2015, **15**, 7933–7942.
87 D. Jung, C. Lim, J. Shim Hyung, Y. Kim, C. Park, J. Jung, I. Han Sang, S.-H. Sunwoo, W. Cho Kyoung, D. Cha Gi, C. Kim Dong, H. Koo Ja, H. Kim Ji, T. Hyeon and D.-H. Kim, *Science*, 2021, **373**, 1022–1026.
88 M. G. Shin, C. J. Choi, Y. Jung, J. H. Choi and J. S. Ko, *AIP Adv.*, 2020, **10**, 035101.
89 F. Yin, H. Lu, H. Pan, H. Ji, S. Pei, H. Liu, J. Huang, J. Gu, M. Li and J. Wei, *Sci. Rep.*, 2019, **9**, 2403.
90 A. Takemoto, T. Araki, Y. Noda, T. Uemura, S. Yoshimoto, R. Abbel, C. Rentrop, J. van den Brand and T. Sekitani, *Nanotechnology*, 2019, **30**, 37LT03.
91 S. Cho, S. Kang, A. Pandya, R. Shanker, Z. Khan, Y. Lee, J. Park, S. L. Craig and H. Ko, *ACS Nano*, 2017, **11**, 4346–4357.
92 B. R. Yang, G. S. Liu, S. J. Han, W. Cao, H. J. Chen, J. G. Lu and H. P. D. Shieh, *J. Disp. Technol.*, 2015, **11**, 625–629.
93 J. Dong, N. M. Abukhdeir and I. A. Goldthorpe, *Nanotechnology*, 2015, **26**, 485302.
94 B. Park, I. G. Bae and Y. H. Huh, *Sci. Rep.*, 2016, **6**, 19485.
95 D. J. Kim, H. I. Shin, E. H. Ko, K. H. Kim, T. W. Kim and H. K. Kim, *Sci. Rep.*, 2016, **6**, 34322.
96 Y. R. Chen, C. C. Hong, T. M. Liou, K. C. Hwang and T. F. Guo, *Sci. Rep.*, 2017, **7**, 16662.
97 J. Yao, H. Yan and C. M. Lieber, *Nat. Nanotechnol.*, 2013, **8**, 329–335.
98 G.-S. Liu, M. He, T. Wang, L. Wang, Z. He, R. Zhan, L. Chen, Y. Chen, B.-R. Yang, Y. Luo and Z. Chen, *ACS Appl. Mater. Interfaces*, 2020, **12**, 53984–53993.
99 G.-S. Liu, C. Liu, H.-J. Chen, W. Cao, J.-S. Qiu, H.-P. D. Shieh and B.-R. Yang, *Nanoscale*, 2016, **8**, 5507–5515.
100 X. Liu, Y.-Z. Long, L. Liao, X. Duan and Z. Fan, *ACS Nano*, 2012, **6**, 1888–1900.
101 Y. Z. Long, M. Yu, B. Sun, C. Z. Gu and Z. Fan, *Chem. Soc. Rev.*, 2012, **41**, 4560–4580.
102 P. C. Hsu, S. Wang, H. Wu, V. K. Narasimhan, D. S. Kong, H. R. Lee and Y. Cui, *Nat. Commun.*, 2013, **4**, 2522.
103 V. Flauraud, M. Mastrangeli, G. D. Bernasconi, J. Butet, D. T. L. Alexander, E. Shahrabi, O. J. F. Martin and J. Brugger, *Nat. Nanotechnol.*, 2017, **12**, 73–80.
104 H. S. Wu, M. Menon, E. Gates, A. Balasubramanian and C. J. Bettinger, *Adv. Mater.*, 2014, **26**, 706–711.
105 J. Wu, X. Que, Q. Hu, D. Luo, T. Liu, F. Liu, T. P. Russell, R. Zhu and Q. Gong, *Adv. Funct. Mater.*, 2016, **26**, 4822–4828.
106 D. Ko, B. Gu, S. J. Kang, S. Jo, D. C. Hyun, C. S. Kim and J. Kim, *J. Mater. Chem. A*, 2019, **7**, 14536–14544.
107 B. Han, K. Pei, Y. L. Huang, X. J. Zhang, Q. K. Rong, Q. G. Lin, Y. F. Guo, T. Y. Sun, C. F. Guo, D. Carnahan, M. Giersig, Y. Wang, J. W. Gao, Z. F. Ren and K. Kempa, *Adv. Mater.*, 2014, **26**, 873–877.
108 J. H. Maurer, L. Gonzalez-Garcia, B. Reiser, I. Kanelidis and T. Kraus, *Nano Lett.*, 2016, **16**, 2921–2925.
109 P. Song, H. Qin, H. L. Gao, H. P. Cong and S. H. Yu, *Nat. Commun.*, 2018, **9**, 2786.
110 G.-S. Liu, T. Wang, Y. Wang, H. Zheng, Y. Chen, Z. Zeng, L. Chen, Y. Chen, B.-R. Yang, Y. Luo and Z. Chen, *Nano Res.*, 2022, **15**, 2582–2591.
111 B. Li, B. Jiang, W. Han, M. He, X. Li, W. Wang, S. W. Hong, M. Byun, S. Lin and Z. Lin, *Angew. Chem., Int. Ed.*, 2017, **56**, 4554–4559.
112 J. Xu, Z. Qiu, M. Yang, J. Chen, Q. Luo, Z. Wu, G.-S. Liu, J. Wu, Z. Qin and B.-R. Yang, *ACS Appl. Mater. Interfaces*, 2021, **13**, 52880–52891.
113 J. Kim, S. M. Lee, J. S. You, N. Y. Kim, S. Wooh and S. T. Chang, *J. Ind. Eng. Chem.*, 2022, **107**, 410–417.
114 H. Dai, R. Ding, M. Li, J. Huang, Y. Li and M. Trevor, *Sci. Rep.*, 2014, **4**, 6742.
115 D. Mampallil and H. B. Eral, *Adv. Colloid Interface Sci.*, 2018, **252**, 38–54.
116 R. D. Deegan, O. Bakajin, T. F. Dupont, G. Huber, S. R. Nagel and T. A. Witten, *Nature*, 1997, **389**, 827–829.
117 H. Ma and J. Hao, *Chem. Soc. Rev.*, 2011, **40**, 5457–5471.
118 Z. Wang, R. Bao, X. Zhang, X. Ou, C. S. Lee, J. C. Chang and X. Zhang, *Angew. Chem., Int. Ed.*, 2011, **50**, 2811–2815.
119 C. Zhang, X. Zhang, X. Zhang, X. Fan, J. Jie, J. C. Chang, C.-S. Lee, W. Zhang and S.-T. Lee, *Adv. Mater.*, 2008, **20**, 1716–1720.
120 M. Grzelczak, J. Vermant, E. M. Furst and L. M. Liz-Marzán, *ACS Nano*, 2010, **4**, 3591–3605.
121 G. Shao, D. A. H. Hanaor, X. Shen and A. Gurlo, *Adv. Mater.*, 2020, **32**, 1907176.
122 L. Li, Q. Fan, H. Xue, S. Zhang, S. Wu, Z. He and J. Wang, *RSC Adv.*, 2020, **10**, 9894–9901.

123 A. Zhang, H. Bai and L. Li, *Chem. Rev.*, 2015, **115**, 9801–9868.
124 H. L. Gao, L. Xu, F. Long, Z. Pan, Y. X. Du, Y. Lu, J. Ge and S. H. Yu, *Angew. Chem., Int. Ed.*, 2014, **53**, 4561–4566.
125 P. Yan, E. Brown, Q. Su, J. Li, J. Wang, C. Xu, C. Zhou and D. Lin, *Small*, 2017, **13**, 1701756.
126 F. Qian, P. C. Lan, M. C. Freyman, W. Chen, T. Kou, T. Y. Olson, C. Zhu, M. A. Worsley, E. B. Duoss, C. M. Spadaccini, T. Baumann and T. Y.-J. Han, *Nano Lett.*, 2017, **17**, 7171–7176.
127 X. Li, H. Wang, Q. Xu, S. Guo, J. Du, X. Liu, J. Weng and J. Xu, *Adv. Mater. Interfaces*, 2018, **5**, 1800256.
128 M. Su, Z. Huang, Y. Li, X. Qian, Z. Li, X. Hu, Q. Pan, F. Li, L. Li and Y. Song, *Adv. Mater.*, 2018, **30**, 1703963.
129 L. Zhang, X. Liu, A. Deb and G. Feng, *ACS Sustainable Chem. Eng.*, 2019, **7**, 19910–19917.
130 H. Li, Y. Ma, Z. Liang, Z. Wang, Y. Cao, Y. Xu, H. Zhou, B. Lu, Y. Chen, Z. Han, S. Cai and X. Feng, *Natl. Sci. Rev.*, 2020, **7**, 849–862.
131 S. Wu, L. Li, H. Xue, K. Liu, Q. Fan, G. Bai and J. Wang, *ACS Nano*, 2017, **11**, 9898–9905.
132 H. Zhang, Q. Liao, X. Wang, Z. Xu and H. Fu, *Nanoscale*, 2015, **7**, 10186–10192.
133 W. Zhou, S. Yao, H. Wang, Q. Du, Y. Ma and Y. Zhu, *ACS Nano*, 2020, **14**, 5798–5805.
134 S. Gong, Y. Zhao, L. W. Yap, Q. Shi, Y. Wang, J. A. P. B. Bay, D. T. H. Lai, H. Uddin and W. Cheng, *Adv. Electron. Mater.*, 2016, **2**, 1600121.
135 P. Wang, T. Zhao, R. Bian, G. Wang and H. Liu, *ACS Nano*, 2017, **11**, 12385–12391.
136 H. Liu, J. Zhai and L. Jiang, *Soft Matter*, 2006, **2**, 811–821.
137 H. Liu, S. Li, J. Zhai, H. Li, Q. Zheng, L. Jiang and D. Zhu, *Angew. Chem., Int. Ed.*, 2004, **43**, 1146–1149.
138 H. Zhou, P. Heyer, H.-J. Kim, J.-H. Song, L. Piao and S.-H. Kim, *Chem. Mater.*, 2011, **23**, 3622–3627.
139 Z. Cui, Y. Han, Q. Huang, J. Dong and Y. Zhu, *Nanoscale*, 2018, **10**, 6806–6811.
140 Q. Huang and Y. Zhu, *Sci. Rep.*, 2018, **8**, 15167.
141 X. Li, G. S. Lee, S. H. Park, H. Kong, T. K. An and S. H. Kim, *Org. Electron.*, 2018, **62**, 357–365.
142 S. Liu, X. Shi, X. Li, Y. Sun, J. Zhu, Q. Pei, J. Liang and Y. Chen, *Nanoscale*, 2018, **10**, 20096–20107.
143 L. Tu, S. Yuan, H. Zhang, P. Wang, X. Cui, J. Wang, Y.-Q. Zhan and L.-R. Zheng, *J. Appl. Phys.*, 2018, **123**, 174905.
144 X. Li, K. Kim, H. Oh, H. C. Moon, S. Nam and S. H. Kim, *Org. Electron.*, 2019, **69**, 190–199.
145 P. Sopeña, P. Serra and J. M. Fernández-Pradas, *Appl. Surf. Sci.*, 2019, **476**, 828–833.
146 W. Xu, S. Zhang and W. Xu, *Sci. China Mater.*, 2019, **62**, 1709–1726.
147 S. J. Lee, Y. H. Kim, J. K. Kim, H. Baik, J. H. Park, J. Lee, J. Nam, J. H. Park, T. W. Lee, G. R. Yi and J. H. Cho, *Nanoscale*, 2014, **6**, 11828–11834.
148 Junaidi, K. Triyana, Harsojo and E. Suharyadi, *Mater. Sci. Eng.*, 2017, **202**, 012055.
149 B. Li, C. Zhang, B. Jiang, W. Han and Z. Lin, *Angew. Chem., Int. Ed.*, 2015, **54**, 4250–4254.
150 S. Pan, J. Peng and Z. Lin, *Angew. Chem., Int. Ed.*, 2021, **60**, 11751–11757.
151 B. R. Yang, W. Cao, G. S. Liu, H. J. Chen, Y. Y. Noh, T. Minari, H. C. Hsiao, C. Y. Lee, H. P. Shieh and C. Liu, *ACS Appl. Mater. Interfaces*, 2015, **7**, 21433–21441.
152 Y. Huang, X. Duan, Q. Wei and C. M. Lieber, *Science*, 2001, **291**, 630–633.
153 G. Yu, X. Li, C. M. Lieber and A. Cao, *J. Mater. Chem.*, 2008, **18**, 728–734.
154 G. Yu, A. Cao and C. M. Lieber, *Nat. Nanotechnol.*, 2007, **2**, 372–377.
155 M. C. LeMieux, M. Roberts, S. Barman, Y. W. Jin, J. M. Kim and Z. N. Bao, *Science*, 2008, **321**, 101–104.
156 V. Calabrese, S. J. Haward and A. Q. Shen, *Macromolecules*, 2021, **54**, 4176–4185.
157 X. Gu, L. Shaw, K. Gu, M. F. Toney and Z. Bao, *Nat. Commun.*, 2018, **9**, 534.
158 K. B. Moses, S. G. Advani and A. Reinhardt, *Rheol. Acta*, 2001, **40**, 296–306.
159 S. Wu, L. Yang, M. Zou, Y. Yang, M. Du, W. Xu, L. Yang, Y. Fang and A. Cao, *Nano Lett.*, 2016, **16**, 4917–4924.
160 R. Bian, L. Meng, M. Zhang, L. Chen and H. Liu, *ACS Omega*, 2019, **4**, 1816–1823.
161 L. Meng, R. Bian, C. Guo, B. Xu, H. Liu and L. Jiang, *Adv. Mater.*, 2018, **30**, 1706938.
162 Y. Gong, X. Zhang, T. Yang, W. Huang, H. Liu, H. Liu, B. Zheng, D. Li, X. Zhu, W. Hu and A. Pan, *Nanotechnology*, 2019, **30**, 345603.
163 H. Jeong, S. Park, J. Lee, P. Won, S.-H. Ko and D. Lee, *Adv. Electron. Mater.*, 2018, **4**, 1800243.
164 L. Meng, M. Zhang, H. Deng, B. Xu and H. Liu, *CCS Chem.*, 2020, **3**, 2194–2202.
165 X. Feng, L. Wang, Y. Y. S. Huang, Y. Luo, J. Ba, H. H. Shi, Y. Pei, S. Zhang, Z. Zhang, X. Jia and B. Lu, *ACS Appl. Mater. Interfaces*, 2022, **14**, 39199–39210.
166 J.-U. Park, M. Hardy, S. J. Kang, K. Barton, K. Adair, D. K. Mukhopadhyay, C. Y. Lee, M. S. Strano, A. G. Alleyne, J. G. Georgiadis, P. M. Ferreira and J. A. Rogers, *Nat. Mater.*, 2007, **6**, 782–789.
167 J. H. Choi, M. G. Shin, Y. Jung, D. H. Kim and J. S. Ko, *Micromachines*, 2020, **11**, 2101687.
168 C. Li, N. Wang, Q. Lei, J. Evans and S. He, *Opt. Mater. Express*, 2021, **11**, 3321–3331.
169 H. Hu, M. Pauly, O. Felix and G. Decher, *Nanoscale*, 2017, **9**, 1307–1314.
170 H. Chen, S. Chen, Y. Guan, H. Yan, R. Jin, H. Zhang, D. Li, J. Zhong and L. Li, *RSC Adv.*, 2017, **7**, 46621–46628.
171 J. Xue, T. Wu, Y. Dai and Y. Xia, *Chem. Rev.*, 2019, **119**, 5298–5415.
172 C.-L. Zhang, K.-P. Lv, H.-P. Cong and S.-H. Yu, *Small*, 2012, **8**, 648–653.
173 H. Wu, D. S. Kong, Z. C. Ruan, P. C. Hsu, S. Wang, Z. F. Yu, T. J. Carney, L. B. Hu, S. H. Fan and Y. Cui, *Nat. Nanotechnol.*, 2013, **8**, 421–425.
174 A. Miyamoto, S. Lee, N. F. Cooray, S. Lee, M. Mori, N. Matsuhisa, H. Jin, L. Yoda, T. Yokota, A. Itoh,

M. Sekino, H. Kawasaki, T. Ebihara, M. Amagai and T. Someya, *Nat. Nanotechnol.*, 2017, **12**, 907–913.
175 S. An, Y. I. Kim, H. S. Jo, M.-W. Kim, M. W. Lee, A. L. Yarin and S. S. Yoon, *Chem. Eng. J.*, 2017, **327**, 336–342.
176 S. V. Ebadi, H. Fashandi, D. Semnani, B. Rezaei and A. Fakhrali, *Smart Mater. Struct.*, 2020, **29**, 085036.
177 N. Hussain, M. Yousif, A. Ali, M. Mehdi, S. Ullah, A. Ullah, F. K. Mahar and I. S. Kim, *Mater. Chem. Phys.*, 2020, **255**, 123614.
178 N. Hussain, M. Mehdi, M. Yousif, A. Ali, S. Ullah, S. Hussain Siyal, T. Hussain and I. S. Kim, *Nanomaterials*, 2021, **11**, 531.
179 S. An, H. S. Jo, D.-Y. Kim, H. J. Lee, B.-K. Ju, S. S. Al-Deyab, J.-H. Ahn, Y. Qin, M. T. Swihart, A. L. Yarin and S. S. Yoon, *Adv. Mater.*, 2016, **28**, 7149–7154.
180 A. Tao, F. Kim, C. Hess, J. Goldberger, R. He, Y. Sun, Y. Xia and P. Yang, *Nano Lett.*, 2003, **3**, 1229–1233.
181 M. Benkovicova, A. Holos, P. NadaZdy, Y. Halahovets, M. Kotlar, J. Kollar, P. Siffalovic, M. Jergel, E. Majkova, J. Mosnacek and J. Ivanco, *Phys. Chem. Chem. Phys.*, 2019, **21**, 9553–9563.
182 S. A. Camacho, P. H. B. Aoki, F. F. de Assis, A. M. Pires, K. T. de Oliveira, R. F. Aroca and C. J. L. Constantino, *Appl. Spectrosc.*, 2015, **69**, 451–456.
183 D. I. Njoku, G. N. Onuoha, E. E. Oguzie, K. L. Oguzie, A. A. Egbedina and A. N. Alshawabkeh, *Arabian J. Chem.*, 2019, **12**, 4466–4478.
184 E. Pechkova and C. Nicolini, *Nat. Protoc.*, 2017, **12**, 2570–2589.
185 A. Kuzyk, R. Schreiber, Z. Fan, G. Pardatscher, E. M. Roller, A. Hogele, F. C. Simmel, A. O. Govorov and T. Liedl, *Nature*, 2012, **483**, 311–314.
186 J.-L. Wang, Y. Lu, H.-H. Li, J.-W. Liu and S.-H. Yu, *J. Am. Chem. Soc.*, 2017, **139**, 9921–9926.
187 L. Mai, Y. Gu, C. Han, B. Hu, W. Chen, P. Zhang, L. Xu, W. Guo and Y. Dai, *Nano Lett.*, 2009, **9**, 826–830.
188 D. Wang, Y.-L. Chang, Z. Liu and H. Dai, *J. Am. Chem. Soc.*, 2005, **127**, 11871–11875.
189 A. Dong, J. Chen, P. M. Vora, J. M. Kikkawa and C. B. Murray, *Nature*, 2010, **466**, 474–477.
190 A. Sanchez-Iglesias, M. Grzelczak, J. Perez-Juste and L. M. Liz-Marzan, *Angew. Chem., Int. Ed.*, 2010, **49**, 9985–9989.
191 J. Wang, S. Liu, C. Ban, Z. Jia, X. He, J. Ma, X. Pu, W. Li and L. Zhi, *Nanotechnology*, 2019, **30**, 355301.
192 S. Wang, G. Chen, S. Niu, K. Chen, T. Gan, Z. Wang, H. Wang, P. Du, C. W. Leung and S. Qu, *ACS Appl. Mater. Interfaces*, 2019, **11**, 48331–48340.
193 B. Jang, A. Ilong, C. Alcantara, G. Chatzipirpiridis, X. Marti, E. Pellicer, J. Sort, Y. Harduf,, Y. Or, B. J. Nelson and S. Pane, *ACS Appl. Mater. Interfaces*, 2019, **11**, 3214–3223.
194 S. J. Boehm, L. Kang, D. H. Werner and C. D. Keating, *Adv. Funct. Mater.*, 2017, **27**, 1604703.
195 R. Mehta, S. Chugh and Z. Chen, *Nano Lett.*, 2015, **15**, 2024–2030.
196 T. H. Kim, X. G. Zhang, D. M. Nicholson, B. M. Evans, N. S. Kulkarni, B. Radhakrishnan, E. A. Kenik and A. P. Li, *Nano Lett.*, 2010, **10**, 3096–3100.
197 S. R. Darmakkolla, H. Tran, A. Gupta and S. B. Rananavare, *RSC Adv.*, 2016, **6**, 93219–93230.
198 Y. Yang, J. L. Wang, L. Liu, Z. H. Wang, J. W. Liu and S. H. Yu, *Nanoscale*, 2017, **9**, 52–55.
199 S. J. Boehm, L. Lin, K. Guzmán Betancourt, R. Emery, J. S. Mayer, T. S. Mayer and C. D. Keating, *Langmuir*, 2015, **31**, 5779–5786.
200 M. Li, R. B. Bhiladvala, T. J. Morrow, J. A. Sioss, K. K. Lew, J. M. Redwing, C. D. Keating and T. S. Mayer, *Nat. Nanotechnol.*, 2008, **3**, 88–92.
201 J. Molina, D. Ramos, E. Gil-Santos, J. E. Escobar, J. J. Ruz, J. Tamayo, A. San Paulo and M. Calleja, *Nano Lett.*, 2020, **20**, 2359–2369.
202 H. E. Ruda and A. Shik, *J. Appl. Phys.*, 2011, **109**, 064305.
203 T. H. Kim, S. Y. Lee, N. K. Cho, H. K. Seong, H. J. Choi, S. W. Jung and S. K. Lee, *Nanotechnology*, 2006, **17**, 3394–3399.
204 Y. Ahn, H. Lee, D. Lee and Y. Lee, *ACS Appl. Mater. Interfaces*, 2014, **6**, 18401–18407.
205 S. Kim, S. Y. Kim, J. Kim and J. H. Kim, *J. Mater. Chem. C*, 2014, **2**, 5636–5643.
206 V. Martinez, F. Stauffer, M. O. Adagunodo, C. Forro, J. Voros and A. Larmagnac, *ACS Appl. Mater. Interfaces*, 2015, **7**, 13467–13475.
207 J. Wang, J. Jiu, T. Sugahara, S. Nagao, M. Nogi, H. Koga, P. He, K. Suganuma and H. Uchida, *ACS Appl. Mater. Interfaces*, 2015, **7**, 23297–23304.
208 Y. Ko, J. Kim, D. Kim, Y. Yamauchi, J. H. Kim and J. You, *Sci. Rep.*, 2017, **7**, 2282.
209 H. S. Ko, Y. Lee, S. Y. Min, S. J. Kwon and T. W. Lee, *Nanoscale*, 2017, **9**, 15766–15772.
210 M. D. S. L. Wimalananda, J.-K. Kim and J.-M. Lee, *Mater. Sci. Eng., B*, 2018, **228**, 67–73.
211 C.-H. An, S. Kim, H.-J. Lee and B. Hwang, *J. Mater. Chem. C*, 2017, **5**, 4804–4809.
212 S. Kim, B. Kim, S. M. Cho, H.-J. Lee and B. Hwang, *Mater. Lett.*, 2017, **209**, 433–436.
213 H. Kim, G. Lee, S. Becker, J.-S. Kim, H. Kim and B. Hwang, *J. Mater. Chem. C*, 2018, **6**, 9394–9398.
214 M.-S. Kim, D.-H. Lee, K.-B. Kim, S.-H. Jung, J.-K. Lee, B.-H. O. S.-G. Lee and S.-G. Park, *Thin Solid Films*, 2015, **587**, 100–105.
215 N. Chou, Y. Kim and S. Kim, *ACS Appl. Mater. Interfaces*, 2016, **8**, 6269–6276.
216 T. N. Trung, D.-O. Kim, J.-H. Lee, V.-D. Dao, H.-S. Choi and E.-T. Kim, *ACS Appl. Mater. Interfaces*, 2017, **9**, 21406–21412.
217 J. H. Lee, B.-C. Huynh-Nguyen, E. Ko, J. H. Kim and G. H. Seong, *Sens. Actuators, B*, 2016, **224**, 789–797.
218 W. Li, A. Meredov and A. Shamim, *npj Flexible Electron.*, 2019, **3**, 19.
219 C. H. Song, C. J. Han, B. K. Ju and J. W. Kim, *ACS Appl. Mater. Interfaces*, 2016, **8**, 480–489.
220 Z. Zhong, H. Lee, D. Kang, S. Kwon, Y. M. Choi, I. Kim, K. Y. Kim, Y. Lee, K. Woo and J. Moon, *ACS Nano*, 2016, **10**, 7847–7854.
221 H. Oh, J. Lee, J.-H. Kim, J.-W. Park and M. Lee, *J. Phys. Chem. C*, 2016, **120**, 20471–20477.

222 H. Oh and M. Lee, *Mater. Lett.*, 2016, **176**, 110–113.
223 H.-C. Liu, H.-W. Zan, O. Soppera, Y. Zhang and B.-R. Yang, *RSC Adv.*, 2017, **7**, 33091–33097.
224 H. Oh, J. Lee and M. Lee, *Appl. Surf. Sci.*, 2018, **427**, 65–73.
225 J.-W. Yoon, W. S. Chang and S. H. Cho, *Opt. Lasers Eng.*, 2015, **73**, 40–45.
226 M. Cann, M. J. Large, S. J. Henley, D. Milne, T. Sato, H. Chan, I. Jurewicz and A. B. Dalton, *Mater. Today Commun.*, 2016, **7**, 42–50.
227 Y. Fang, K. Ding, Z. Wu, H. Chen, W. Li, S. Zhao, Y. Zhang, L. Wang, J. Zhou and B. Hu, *ACS Nano*, 2016, **10**, 10023–10030.
228 C.-C. Yang, Y.-C. Lin, M.-W. Hung, H.-Y. Tsai, K.-C. Huang and W.-T. Hsiao, *Appl. Surf. Sci.*, 2019, **484**, 1019–1026.
229 C. Liang, X. Sun, J. Zheng, W. Su, Y. Hu and J. A. Duan, *Microelectron. Eng.*, 2020, **232**, 111396.
230 N.-H. Tran, H.-M. Hoang, T.-H. Duong and H.-C. Kim, *Appl. Surf. Sci.*, 2020, **520**, 146216.
231 D. J. Finn, M. Lotya and J. N. Coleman, *ACS Appl. Mater. Interfaces*, 2015, **7**, 9254–9261.
232 Q. Huang, K. N. Al-Milaji and H. Zhao, *ACS Appl. Nano Mater.*, 2018, **1**, 4528–4536.
233 D. Li, X. Liu, X. Chen, W. Y. Lai and W. Huang, *Adv. Mater. Technol.*, 2019, **4**, 1900196.
234 W. Li, E. Yarali, A. Bakytbekov, T. D. Anthopoulos and A. Shamim, *Nanotechnology*, 2020, **31**, 395201.
235 J. Park, G. Kim, B. Lee, S. Lee, P. Won, H. Yoon, H. Cho, S. H. Ko and Y. Hong, *Adv. Mater. Technol.*, 2020, **5**, 2000042.
236 Y. C. Kao and F. C. Hong, *Nanotechnology*, 2011, **22**, 185303.
237 J. Ahn, J. W. Seo, T. I. Lee, D. Kwon, I. Park, T. S. Kim and J. Y. Lee, *ACS Appl. Mater. Interfaces*, 2016, **8**, 19031–19037.
238 T. Wan, P. Guan, X. Guan, L. Hu, T. Wu, C. Cazorla and D. Chu, *ACS Appl. Mater. Interfaces*, 2020, **12**, 34086–34094.
239 K. Park, K. Woo, J. Kim, D. Lee, Y. Ahn, D. Song, H. Kim, D. Oh, S. Kwon and Y. Lee, *ACS Appl. Mater. Interfaces*, 2019, **11**, 14882–14891.
240 Z. He, L. Wang, G.-S. Liu, Y. Xu, Z. Qiu, M. Zhong, X. Li, X. Gui, Y.-S. Lin, Z. Qin, J. Wu, X. Xie, C. Liu and B.-R. Yang, *ACS Appl. Electron. Mater.*, 2020, **2**, 1335–1342.
241 S. Liu, S. Ho and F. So, *ACS Appl. Mater. Interfaces*, 2016, **8**, 9268–9274.
242 L. Wang, P. Chen, Y. C. Wang, G. S. Liu, C. Liu, X. Xie, J. Z. Li and B. R. Yang, *ACS Appl. Mater. Interfaces*, 2018, **10**, 16596–16604.
243 L. Wang, G.-S. Liu, P. Chen, J. Wu, Z.-X. Wang, X. Xie and B.-R. Yang, *Appl. Phys. Express*, 2018, **11**, 116502.
244 Y. Chen, R. S. Carmichael and T. B. Carmichael, *ACS Appl. Mater. Interfaces*, 2019, **11**, 31210–31219.
245 E. J. Menke, M. A. Thompson, C. Xiang, L. C. Yang and R. M. Penner, *Nat. Mater.*, 2006, **5**, 914–919.
246 C. Xiang, S. C. Kung, D. K. Taggart, F. Yang, M. A. Thompson, A. G. Guell, Y. Yang and R. M. Penner, *ACS Nano*, 2008, **2**, 1939–1949.
247 M. S. Goh, Y. H. Lee, S. Pedireddy, I. Y. Phang, W. W. Tjiu, J. M. Tan and X. Y. Ling, *Langmuir*, 2012, **28**, 14441–14449.
248 E. H. Cho, J. Hwang, J. Kim, J. Lee, C. Kwak and C. S. Lee, *Opt. Express*, 2015, **23**, 26095–26103.
249 J. Li, Y. Tao, S. Chen, H. Li, P. Chen, M. Z. Wei, H. Wang, K. Li, M. Mazzeo and Y. Duan, *Sci. Rep.*, 2017, **7**, 16468.
250 D. J. Lee, I. S. Yoon, C. H. Park, J. Choi, Y. W. Park and B. K. Ju, *Sci. Rep.*, 2019, **9**, 12312.
251 S. R. Kim, J. H. Kim and J. W. Park, *ACS Appl. Mater. Interfaces*, 2017, **9**, 26407–26416.
252 B. Yoo, Y. Kim, C. J. Han, M. S. Oh and J.-W. Kim, *Appl. Surf. Sci.*, 2018, **429**, 151–157.
253 G. Wang, L. Bi, W. Wei, X. Zhang, Y. Gu, L. Huang, H. Yin, Y. Li, G. Chen, Z. Wu and C. Ye, *ACS Appl. Nano Mater.*, 2019, **2**, 6707–6714.
254 Q. Sun, S. J. Lee, H. Kang, Y. Gim, H. S. Park and J. H. Cho, *Nanoscale*, 2015, **7**, 6798–6804.
255 H. S. Kang, J. Choi, W. Cho, H. Lee, D. Lee, D. G. Lee and H.-T. Kim, *J. Mater. Chem. C*, 2016, **4**, 9834–9840.
256 G. W. Huang, Q. P. Feng, H. M. Xiao, N. Li and S. Y. Fu, *ACS Nano*, 2016, **10**, 8895–8903.
257 D. Yoo, D.-J. Won, W. Cho, S. Kim and J. Kim, *Small Methods*, 2021, **5**, 2101049.
258 J. H. Park, S. Han, D. Kim, B. K. You, D. J. Joe, S. Hong, J. Seo, J. Kwon, C. K. Jeong, H.-J. Park, T.-S. Kim, S. H. Ko and K. J. Lee, *Adv. Funct. Mater.*, 2017, **27**, 1701138.
259 D. Kim, J. Bang, W. Lee, I. Ha, J. Lee, H. Eom, M. Kim, J. Park, J. Choi, J. Kwon, S. Han, H. Park, D. Lee and S. H. Ko, *J. Mater. Chem. A*, 2020, **8**, 8281–8291.
260 C.-H. Song, K.-H. Ok, C.-J. Lee, Y. Kim, M.-G. Kwak, C. J. Han, N. Kim, B.-K. Ju and J.-W. Kim, *Org. Electron.*, 2015, **17**, 208–215.
261 C. J. Han, B.-G. Park, M. Suk Oh, S.-B. Jung and J.-W. Kim, *J. Mater. Chem. C*, 2017, **5**, 9986–9994.
262 Z. Zhong, K. Woo, I. Kim, H. Hwang, S. Kwon, Y. M. Choi, Y. Lee, T. M. Lee, K. Kim and J. Moon, *Nanoscale*, 2016, **8**, 8995–9003.
263 S. Jun, B.-K. Ju and J.-W. Kim, *Adv. Mater. Technol.*, 2016, **1**, 1600062.
264 K. Shin, J. S. Park, J. H. Han, Y. Choi, D. S. Chung and S. H. Kim, *Sci. Rep.*, 2017, **7**, 40087.
265 S. S. Yoon and D. Y. Khang, *ACS Appl. Mater. Interfaces*, 2016, **8**, 23236–23243.
266 M. Jo, S. Bae, I. Oh, J. H. Jeong, B. Kang, S. J. Hwang, S. S. Lee, H. J. Son, B. M. Moon, M. J. Ko and P. Lee, *ACS Nano*, 2019, **13**, 12500–12510.
267 H. Kim, H. Lee, I. Ha, J. Jung, P. Won, H. Cho, J. Yeo, S. Hong, S. Han, J. Kwon, K.-J. Cho and S. H. Ko, *Adv. Funct. Mater.*, 2018, **28**, 1801847.
268 S. J. Henley, M. Cann, I. Jurewicz, A. Dalton and D. Milne, *Nanoscale*, 2014, **6**, 946–952.
269 Q. Che, Q. Zhao, M. Hu, R. Qin, G. Shan and J. Yang, *ACS Appl. Nano Mater.*, 2021, **4**, 12726–12736.
270 F. Nichols and W. Mullins, *Trans. Metall. Soc. AIME*, 1965, **233**, 1840–1848.
271 S. Yadavali, V. P. Sandireddy and R. Kalyanaraman, *Nanotechnology*, 2016, **27**, 195602.
272 Y. Ahn, Y. Jeong and Y. Lee, *ACS Appl. Mater. Interfaces*, 2012, **4**, 6410–6414.
273 T. B. Song, Y. S. Rim, F. Liu, B. Bob, S. Ye, Y. T. Hsieh and Y. Yang, *ACS Appl. Mater. Interfaces*, 2015, **7**, 24601–24607.

274 G. S. Liu, Y. Xu, Y. Kong, L. Wang, J. Wang, X. Xie, Y. Luo and B. R. Yang, *ACS Appl. Mater. Interfaces*, 2018, **10**, 37699–37708.
275 T. Wan, Y. Pan, H. Du, B. Qu, J. Yi and D. Chu, *ACS Appl. Mater. Interfaces*, 2018, **10**, 2716–2724.
276 G.-S. Liu, H. Zheng, Z. Zeng, Y. Wang, W. Guo, T. Wang, H. Chen, Y. Chen, S. Hu, L. Chen, Y. Chen, W. Xie, B.-R. Yang and Y. Luo, *Nano Res.*, 2022, **15**, 4552–4562.
277 B. Derby, *Annu. Rev. Mater. Res.*, 2010, **40**, 395–414.
278 J. S. R. Wheeler, S. W. Reynolds, S. Lancaster, V. S. Romanguera and S. G. Yeates, *Polym. Degrad. Stab.*, 2014, **105**, 116–121.
279 J.-T. Wu, S. Lien-Chung Hsu, M.-H. Tsai, Y.-F. Liu and W.-S. Hwang, *J. Mater. Chem.*, 2012, **22**, 15599.
280 H. Lu, J. Lin, N. Wu, S. Nie, Q. Luo, C.-Q. Ma and Z. Cui, *Appl. Phys. Lett.*, 2015, **106**, 093302.
281 P. Maisch, K. C. Tam, L. Lucera, H.-J. Egelhaaf, H. Scheiber, E. Maier and C. J. Brabec, *Org. Electron.*, 2016, **38**, 139–143.
282 K.-H. Choi, J. Yoo, C. K. Lee and S.-Y. Lee, *Energy Environ. Sci.*, 2016, **9**, 2812–2821.
283 L. Cai, S. Zhang, Y. Zhang, J. Li, J. Miao, Q. Wang, Z. Yu and C. Wang, *Adv. Mater. Technol.*, 2018, **3**, 1700232.
284 C. Wang, G. Y. Hong, K. M. Li and H. T. Young, *Sensors*, 2017, **17**, 2602.
285 Q. Jing, Y. S. Choi, M. Smith, N. Ćatić, C. Ou and S. Kar-Narayan, *Adv. Mater. Technol.*, 2019, **4**, 1800328.
286 M. Smith, Y. S. Choi, C. Boughey and S. Kar-Narayan, *Flexible Printed Electron.*, 2017, **2**, 015004.
287 A. Mahajan, C. D. Frisbie and L. F. Francis, *ACS Appl. Mater. Interfaces*, 2013, **5**, 4856–4864.
288 E. B. Secor, *Flexible Printed Electron.*, 2018, **3**, 035002.
289 T. Seifert, E. Sowade, F. Roscher, M. Wiemer, T. Gessner and R. R. Baumann, *Ind. Eng. Chem. Res.*, 2015, **54**, 769–779.
290 M. S. Onses, E. Sutanto, P. M. Ferreira, A. G. Alleyne and J. A. Rogers, *Small*, 2015, **11**, 4237–4266.
291 B. Zhang, J. He, X. Li, F. Xu and D. Li, *Nanoscale*, 2016, **8**, 15376–15388.
292 S. M. Yang, Y. S. Lee, Y. Jang, D. Byun and S.-H. Choa, *Microelectron. Reliab.*, 2016, **65**, 151–159.
293 P. Ren, Y. Liu, R. Song, B. O'Connor, J. Dong and Y. Zhu, *ACS Appl. Electron. Mater.*, 2020, **3**, 192–202.
294 H. Dong, L. Zhang, T. Wu, H. Song, J. Luo, F. Huang and C. Zuo, *Org. Electron.*, 2021, **89**, 106044.
295 J. Liang, K. Tong and Q. Pei, *Adv. Mater.*, 2016, **28**, 5986–5996.
296 D. Du, X. Yang, Y. Yang, Y. Zhao and Y. Wang, *Micromachines*, 2019, **10**, 42.
297 Q. Liu, B. Tian, C. Luo, J. Liang and W. Wu, *Adv. Mater. Technol.*, 2020, **5**, 2000278.
298 C. Luo, B. Tian, Q. Liu, Y. Feng and W. Wu, *Adv. Mater. Technol.*, 2020, **5**, 1900925.
299 X. Xu, Z. Liu, P. He and J. Yang, *J. Phys. D: Appl. Phys.*, 2019, **52**, 455401.
300 D. Angmo, T. R. Andersen, J. J. Bentzen, M. Helgesen, R. R. Søndergaard, M. Jørgensen, J. E. Carlé, E. Bundgaard and F. C. Krebs, *Adv. Funct. Mater.*, 2015, **25**, 4539–4547.
301 M. Hösel, R. R. Søndergaard, M. Jørgensen and F. C. Krebs, *Energy Technol.*, 2013, **1**, 102–107.
302 G. A. dos Reis Benatto, B. Roth, M. Corazza, R. R. Sondergaard, S. A. Gevorgyan, M. Jorgensen and F. C. Krebs, *Nanoscale*, 2016, **8**, 318–326.
303 S. Thibert, J. Jourdan, B. Bechevet, D. Chaussy, N. Reverdy-Bruas and D. Beneventi, *Mater. Sci. Semicond. Process.*, 2014, **27**, 790–799.
304 X. He, G. Shen, R. Xu, W. Yang, C. Zhang, Z. Liu, B. Chen, J. Liu and M. Song, *Polymers*, 2019, **11**, 468.
305 F. Hoeng, A. Denneulin, N. Reverdy-Bruas, G. Krosnicki and J. Bras, *Appl. Surf. Sci.*, 2017, **394**, 160–168.
306 H. Li, X. Li, J. Liang and Y. Chen, *Adv. Energy Mater.*, 2019, **9**, 1803987.
307 H. Li, S. Liu, X. Li, Z.-S. Wu and J. Liang, *Mater. Chem. Front.*, 2019, **3**, 626–635.
308 W. Li, S. Yang and A. Shamim, *npj Flexible Electron.*, 2019, **3**, 13.
309 Q. Huang and Y. Zhu, *Adv. Mater. Technol.*, 2019, **4**, 1800546.
310 C. Linghu, S. Zhang, C. Wang and J. Song, *npj Flexible Electron.*, 2018, **2**, 26.
311 A. Carlson, A. M. Bowen, Y. Huang, R. G. Nuzzo and J. A. Rogers, *Adv. Mater.*, 2012, **24**, 5284–5318.
312 A. R. Madaria, A. Kumar, F. N. Ishikawa and C. Zhou, *Nano Res.*, 2010, **3**, 564–573.
313 A. R. Madaria, A. Kumar and C. Zhou, *Nanotechnology*, 2011, **22**, 245201.
314 K.-S. Kim, S. O. Kim, C. J. Han, D. U. Kim, J. S. Kim, Y.-T. Yu, C.-R. Lee and J.-W. Kim, *Compos. Sci. Technol.*, 2018, **165**, 58–65.
315 Y. Lin, W. Yuan, C. Ding, S. Chen, W. Su, H. Hu, Z. Cui and F. Li, *ACS Appl. Mater. Interfaces*, 2020, **12**, 24074–24085.
316 D. S. Um, Y. Lee, T. Kim, S. Lim, H. Lee, M. Ha, Z. Khan, S. Kang, M. P. Kim, J. Y. Kim and H. Ko, *ACS Appl. Mater. Interfaces*, 2020, **12**, 32154–32162.
317 B. S. Kim, S. Won, J. Seo, S. K. Jeong, C. Kim, K. S. Kim, S. H. Kim, S. M. Cho and J. H. Kim, *ACS Appl. Mater. Interfaces*, 2021, **13**, 26601–26609.
318 Y. Peng, B. Du, X. Xu, J. Yang, J. Lin and C. Ma, *Appl. Phys. Express*, 2019, **12**, 066503.
319 J. D. Park, S. Lim and H. Kim, *Thin Solid Films*, 2015, **586**, 70–75.
320 L. Xue and Y. Han, *Prog. Polym. Sci.*, 2011, **36**, 269–293.
321 D. Tian, Y. Song and L. Jiang, *Chem. Soc. Rev.*, 2013, **42**, 5184–5209.
322 D. Gentili, G. Foschi, F. Valle, M. Cavallini and F. Biscarini, *Chem. Soc. Rev.*, 2012, **41**, 4430–4443.
323 L. Li, W. Li, X. Liu, M. Tenjimbayashi, H. Segawa, C. Niikura, T. Nakayama and T. Minari, *Adv. Mater. Technol.*, 2022, **7**, 2101687.
324 A. Takemoto, T. Araki, T. Uemura, Y. Noda, S. Yoshimoto, S. Izumi, S. Tsuruta and T. Sekitani, *Adv. Intell. Syst.*, 2020, **2**, 2000093.
325 J.-H. Kim and J.-W. Park, *ACS Appl. Mater. Interfaces*, 2018, **10**, 9704–9717.
326 B. Ha and S. Jo, *Sci. Rep.*, 2017, **7**, 11614.

327 J. H. M. Maurer, L. González-García, B. Reiser, I. Kanelidis and T. Kraus, *Nano Lett.*, 2016, **16**, 2921–2925.
328 K. Tybrandt and J. Voros, *Small*, 2016, **12**, 180–184.
329 Y. Lin, Q. Li, C. Ding, J. Wang, W. Yuan, Z. Liu, W. Su and Z. Cui, *Nano Res.*, 2022, **15**, 4590–4598.
330 J.-G. Sun, T.-N. Yang, C.-Y. Wang and L.-J. Chen, *Nano Energy*, 2018, **48**, 383–390.
331 C. Luo and Q. Liu, *ACS Appl. Mater. Interfaces*, 2017, **9**, 8297–8307.
332 S. Feng, Z. Zhong, Y. Wang, W. Xing and E. Drioli, *J. Membr. Sci.*, 2018, **549**, 332–349.
333 M. Yang, S. W. Kim, S. Zhang, D. Y. Park, C.-W. Lee, Y.-H. Ko, H. Yang, Y. Xiao, G. Chen and M. Li, *J. Mater. Chem. C*, 2018, **6**, 7207–7218.
334 G. W. Huang, H. M. Xiao and S. Y. Fu, *Nanoscale*, 2014, **6**, 8495–8502.
335 B. You, C. J. Han, Y. Kim, B.-K. Ju and J.-W. Kim, *J. Mater. Chem. A*, 2016, **4**, 10435–10443.
336 Y. C. Kim and S. Y. Kim, *RSC Adv.*, 2018, **8**, 19532–19538.
337 S. Jun, S. O. Kim, H.-J. Lee, C. J. Han, C.-J. Lee, Y.-T. Yu, C.-R. Lee, B.-K. Ju, Y. Kim and J.-W. Kim, *J. Mater. Chem. A*, 2019, **7**, 3101–3111.
338 E. H. Cho, J. Hwang, J. Lee, H. C. Park, Y. Kim, C. Kwak, C. S. Lee and Y. S. Woo, *Nanotechnology*, 2019, **30**, 015301.
339 L. Liu, H. Y. Li, D. Ye, Y. Yu, L. Liu and Y. Wu, *Nanotechnology*, 2017, **28**, 225301.
340 S. Yao, J. Yang, F. R. Poblete, X. Hu and Y. Zhu, *ACS Appl. Mater. Interfaces*, 2019, **11**, 31028–31037.
341 Y. Nakajima, K. Obata, M. Machida, A. Hohnholz, J. Koch, O. Suttmann and M. Terakawa, *Opt. Mater. Express*, 2017, **7**, 4203.
342 W. Yuan, X. Wu, W. Gu, J. Lin and Z. Cui, *J. Semicond.*, 2018, **39**, 015002.
343 Q. Huang and Y. Zhu, *ACS Appl. Mater. Interfaces*, 2021, **13**, 60736–60762.
344 G. Haacke, *J. Appl. Phys.*, 1976, **47**, 4086–4089.
345 M. Dressel and G. Gruener, *Am. J. Phys.*, 2002, **70**, 1269–1270.
346 L. Hu, D. S. Hecht and G. Gruner, *Nano Lett.*, 2004, **4**, 2513–2517.
347 S. De, P. J. King, P. E. Lyons, U. Khan and J. N. Coleman, *ACS Nano*, 2010, **4**, 7064–7072.
348 S. Mehra, M. G. Christoforo, P. Peumans and A. Salleo, *Nanoscale*, 2013, **5**, 4400–4403.
349 Y. Fang, Z. Wu, J. Li, F. Jiang, K. Zhang, Y. Zhang, Y. Zhou, J. Zhou and B. Hu, *Adv. Funct. Mater.*, 2018, **28**, 1705409.
350 G. Khanarian, J. Joo, X. Q. Liu, P. Eastman, D. Werner, K. O'Connell and P. Trefonas, *J. Appl. Phys.*, 2013, **114**, 024302.
351 S. I. White, B. A. DiDonna, M. Mu, T. C. Lubensky and K. I. Winey, *Phys. Rev. B: Condens. Matter Mater. Phys.*, 2009, **79**, 024301.
352 F. Du, J. E. Fischer and K. I. Winey, *Phys. Rev. B: Condens. Matter Mater. Phys.*, 2005, **72**, 121404.
353 B. T. Camic, H. I. Jeong, M. H. Aslan, A. Kosemen, S. Kim, H. Choi, F. Basarir and B. R. Lee, *Nanomaterials*, 2020, **10**, 10010046.
354 S.-T. Hsiao, H.-W. Tien, W.-H. Liao, Y.-S. Wang, S.-M. Li, C.-C. Mma, Y.-H. Yu and W.-P. Chuang, *J. Mater. Chem. C*, 2014, **2**, 7284–7291.
355 H.-W. Tien, S.-T. Hsiao, W.-H. Liao, Y.-H. Yu, F.-C. Lin, Y.-S. Wang, S.-M. Li and C.-C. M. Ma, *Carbon*, 2013, **58**, 198–207.
356 Q. Su, T. Xue, Y. Zhang, K. Lan and Q. Zou, *Mater. Lett.*, 2019, **236**, 218–221.
357 B. Zheng, Q. Zhu and Y. Zhao, *J. Mater. Sci.*, 2019, **54**, 5802–5812.
358 C. Ma, X.-M. Gao, Y.-F. Liu, Y.-G. Bi, X.-M. Wen, X.-L. Zhang, D. Yin, J. Feng and H.-B. Sun, *IEEE Trans. Nanotechnol.*, 2021, **20**, 99–103.
359 D. Pu, W. Zhou, Y. Li, J. Chen, J. Chen, H. Zhang, B. Mi, L. Wang and Y. Ma, *RSC Adv.*, 2015, **5**, 100725–100729.
360 J. Wang, H. Chen, Y. Zhao, Z. Zhong, Y. Tang, G. Liu, X. Feng, F. Xu, X. Chen, D. Cai and J. Kang, *ACS Appl. Mater. Interfaces*, 2020, **12**, 35211–35221.
361 K.-W. Lee, H.-J. Lee and J.-Y. Kim, *Synth. Met.*, 2020, **262**, 116333.
362 S. Hu, J. Gu, W. Zhao, H. Ji, X. Ma, J. Wei and M. Li, *Adv. Mater. Technol.*, 2019, **4**, 1900194.
363 M. E. Layani-Tzadka, E. Tirosh and G. Markovich, *ACS Omega*, 2017, **2**, 7584–7592.
364 W. J. Scheideler, J. Smith, I. Deckman, S. Chung, A. C. Arias and V. Subramanian, *J. Mater. Chem. C*, 2016, **4**, 3248–3255.
365 Y. Ling, K. Guo, B. Zhu, B. Prieto-Simon, N. H. Voelcker and W. Cheng, *Nanoscale Horiz.*, 2019, **4**, 1380–1387.
366 Y. Li, J. Chen, X. Han, Y. Li, Z. Zhang and Y. Ma, *NANO*, 2018, **13**, 1850146.
367 C. Weng, Z. Dai, G. Wang, L. Liu and Z. Zhang, *ACS Appl. Mater. Interfaces*, 2019, **11**, 6541–6549.
368 C. F. Guo, Y. Chen, L. Tang, F. Wang and Z. F. Ren, *Nano Lett.*, 2016, **16**, 594–600.
369 E. Y. An, S. Lee, S. G. Lee, E. Lee, J. J. Baek, G. Shin, K. H. Choi, J. H. Cho and G. Y. Bae, *Nanomaterials*, 2021, **11**, 2865.
370 C. Zhao, K. Hu, F.-M. Li, M.-X. Li, S. Li, Y.-F. Zhai, W.-W. Deng, H.-Y. Yu and M. Wang, *Mater. Today Phys.*, 2021, **20**, 100442.
371 Y. Wang, S. Gong, D. Dong, Y. Zhao, L. W. Yap, Q. Shi, T. An, Y. Ling, G. P. Simon and W. Cheng, *Nanoscale*, 2018, **10**, 15948–15955.
372 T. An, S. Gong, Y. Ling, D. Dong, Y. Zhao and W. Cheng, *EcoMat*, 2020, **2**, e12022.
373 J. Li, J. Niu, X. Li, J. Zhou, Z. Hu and W. Guo, *Sci. China: Technol. Sci.*, 2020, **63**, 2131–2136.
374 Y. J. Moon and K.-T. Kang, *Flexible Printed Electron.*, 2022, **7**, 024003.
375 Y. Wang, S. Gong, D. Gómez, Y. Ling, L. W. Yap, G. P. Simon and W. Cheng, *ACS Nano*, 2018, **12**, 8717–8722.
376 B. Zhu, S. Gong, F. Lin, Y. Wang, Y. Ling, T. An and W. Cheng, *Adv. Electron. Mater.*, 2019, **5**, 1800509.
377 T. Kim, S. Kang, J. Heo, S. Cho, J. W. Kim, A. Choe, B. Walker, R. Shanker, H. Ko and J. Y. Kim, *Adv. Mater.*, 2018, **30**, 1800659.

378 K.-M. Chiang, Z.-Y. Huang, W.-L. Tsai and H.-W. Lin, *Org. Electron.*, 2017, **43**, 15–20.
379 Y. Shen, M.-N. Li, Y. Li, F.-M. Xie, H.-Y. Wu, G.-H. Zhang, L. Chen, S.-T. Lee and J.-X. Tang, *ACS Nano*, 2020, **14**, 6107–6116.
380 R. E. Triambulo, J.-H. Kim and J.-W. Park, *Org. Electron.*, 2019, **71**, 220–226.
381 J. Qi, S. Chen, C. Lan, A. C. Wang, X. Cui, Z. You, Q. Zhang, Y. Li, Z. L. Wang, H. Wang and Z. Lin, *Adv. Energy Mater.*, 2020, **10**, 2001185.
382 J. van de Groep, D. Gupta, M. A. Verschuuren, M. M. Wienk, R. A. J. Janssen and A. Polman, *Sci. Rep.*, 2015, **5**, 11414.
383 S. Chen, Y. Guan, Y. Li, X. Yan, H. Ni and L. Li, *J. Mater. Chem. C*, 2017, **5**, 2404–2414.
384 P. Lee, J. Lee, H. Lee, J. Yeo, S. Hong, K. H. Nam, D. Lee, S. S. Lee and S. H. Ko, *Adv. Mater.*, 2012, **24**, 3326–3332.
385 Y. Zhu, M. C. Hartel, N. Yu, P. R. Garrido, S. Kim, J. Lee, P. Bandaru, S. Guan, H. Lin, S. Emaminejad, N. R. de Barros, S. Ahadian, H.-J. Kim, W. Sun, V. Jucaud, M. R. Dokmeci, P. S. Weiss, R. Yan and A. Khademhosseini, *Small Methods*, 2022, **6**, 2100900.
386 Z. Ma, X. Xiang, L. Shao, Y. Zhang and J. Gu, *Angew. Chem., Int. Ed.*, 2022, **61**, e202200705.
387 P. Won, J. J. Park, T. Lee, I. Ha, S. Han, M. Choi, J. Lee, S. Hong, K.-J. Cho and S. H. Ko, *Nano Lett.*, 2019, **19**, 6087–6096.
388 Y. Wang, S. Gong, S. J. Wang, X. Yang, Y. Ling, L. W. Yap, D. Dong, G. P. Simon and W. Cheng, *ACS Nano*, 2018, **12**, 9742–9749.
389 S. Han, C. Liu, H. Xu, D. Yao, K. Yan, H. Zheng, H.-J. Chen, X. Gui, S. Chu and C. Liu, *npj Flexible Electron.*, 2018, **2**, 16.
390 J. Liang, L. Li, X. Niu, Z. Yu and Q. Pei, *Nat. Photonics*, 2013, **7**, 817–824.
391 Y.-F. Li, S.-Y. Chou, P. Huang, C. Xiao, X. Liu, Y. Xie, F. Zhao, Y. Huang, J. Feng, H. Zhong, H.-B. Sun and Q. Pei, *Adv. Mater.*, 2019, **31**, 1807516.
392 Y. Fang, Y. Li, X. Wang, Z. Zhou, K. Zhang, J. Zhou and B. Hu, *Small*, 2020, **16**, 2000450.
393 L. Liu, H. Y. Li, Y. J. Fan, Y. H. Chen, S. Y. Kuang, Z. B. Li, Z. L. Wang and G. Zhu, *Small*, 2019, **15**, 1900755.
394 H. Zhao, Y. Zhou, S. Cao, Y. Wang, J. Zhang, S. Feng, J. Wang, D. Li and D. Kong, *ACS Mater. Lett.*, 2021, **3**, 912–920.
395 J. Liang, L. Li, D. Chen, T. Hajagos, Z. Ren, S.-Y. Chou, W. Hu and Q. Pei, *Nat. Commun.*, 2015, **6**, 7647.
396 Q. Tang, M. Zou, L. Chang and W. Guo, *Chem. Eng. J.*, 2022, **430**, 132152.
397 Z. Wang, L. Zhang, J. Liu and C. Li, *ACS Appl. Mater. Interfaces*, 2019, **11**, 5316–5324.
398 X. Liao, Z. Zhang, Z. Kang, F. Gao, Q. Liao and Y. Zhang, *Mater. Horiz.*, 2017, **4**, 502–510.
399 S. Gong, L. W. Yap, Y. Zhu, B. Zhu, Y. Wang, Y. Ling, Y. Zhao, T. An, Y. Lu and W. Cheng, *Adv. Funct. Mater.*, 2020, **30**, 1910717.
400 G. Lee, G. Y. Bae, J. H. Son, S. Lee, S. W. Kim, D. Kim, S. G. Lee and K. Cho, *Adv. Sci.*, 2020, **7**, 2001184.
401 S. Gong, L. W. Yap, B. Zhu, Q. Zhai, Y. Liu, Q. Lyu, K. Wang, M. Yang, Y. Ling, D. T. H. Lai, F. Marzbanrad and W. Cheng, *Adv. Mater.*, 2019, **31**, 1903789.
402 X. Peng, K. Dong, Y. Zhang, L. Wang, C. Wei, T. Lv, Z. L. Wang and Z. Wu, *Adv. Funct. Mater.*, 2022, **32**, 2112241.
403 X. Jiang, R. Du, R. Hübner, Y. Hu and A. Eychmüller, *Matter*, 2021, **4**, 54–94.